UNIVERSITÀ DEGLI STUDI DI PAVIA
DOTTORATO DI RICERCA IN FISICA – XXIV CICLO

Supersymmetry searches in two-lepton plus E_T^{miss} channel based on a flavour subtraction technique with the ATLAS detector at the LHC

Massimiliano Uslenghi

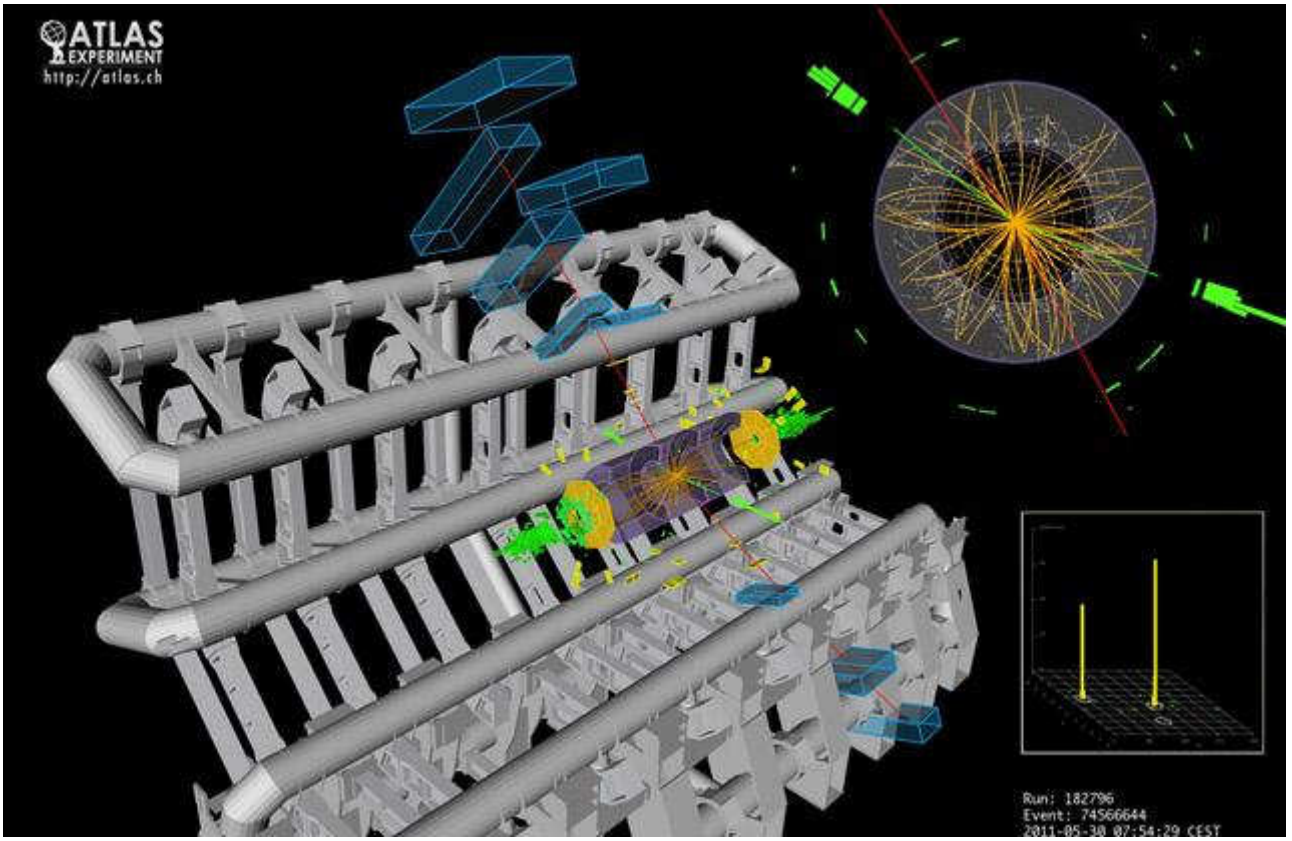

Tesi per il conseguimento del titolo

Università
degli Studi
di Pavia

Dipartimento
di Fisica
"A. Volta"

DOTTORATO DI RICERCA IN FISICA – XXIV CICLO

Supersymmetry searches in two-lepton plus E_T^{miss} channel based on a flavour subtraction technique with the ATLAS detector at the LHC

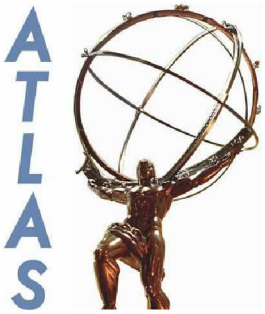

dissertation submitted by

Massimiliano Uslenghi

to obtain the degree of

DOTTORE DI RICERCA IN FISICA

Supervisor: Dott. Giacomo Polesello (INFN Pavia)

Referee: Dott. Davide Costanzo (University of Sheffield)

Cover: An event with two identified muons and two identified electrons from a proton-proton collision in ATLAS. This event is consistent with coming from two Z particles decaying: one Z decays to two muons, the other to two electrons. The two muons are picked out as red tracks penetrating right through the detector. The two electrons are picked out as green tracks in the central, inner detector, matching narrow green clusters of energy in the barrel part of the calorimeters. The inset at the bottom right shows a map of the energy seen in the detector: the two big yellow spikes correspond to the two electrons. Photo: CERN

Supersymmetry searches in two-lepton plus E_T^{miss} channel based on a flavour subtraction technique with the ATLAS detector at the LHC

Massimiliano Uslenghi

PhD thesis – University of Pavia
Printed in Pavia, Italy, April 2012
ISBN: 978-88-95767-53-6

ISBN 978-88-95767-53-6

Supersymmetry searches in two-lepton plus E_T^{miss} channel based on a flavour subtraction technique with the ATLAS detector at the LHC

Massimiliano Uslenghi

2012

To my beloved dad,

living forever in my heart...

Contents

Chapter 1

Introduction

One of the greatest milestones of twentieth century physics was the development of the Standard Model of particle physics, a unified and organic description of the fundamental particles which make up our universe, of their properties and interactions via three of the four fundamental forces. Despite its great successes and the ever increasing accuracy to which it has been verified experimentally, this theory presents some rifts: some natural mechanisms and observations are not completely and clearly described and it makes predictions only after the insertion of key parameters measured by particle and astrophysical experiments with a reduced predicting power. The most easy and accepted solution to these problems and flaws is that the Standard Model is an effective theory of a more general theory, correct only at low energy scale. It must break down at higher energies as yet unexplored.

The quest for a theory describing physics beyond the Standard Model (the so called "new physics") has engaged physicists for the last quarter of a century - with theorists postulating an assortment of models and conjectures, in order to attempt to address the big unanswered questions. One of the most promising, accepted and exciting theories of new physics is the Supersymmetry. (SUSY) The most important novelty is the introduction of a new symmetry: for each known particle, it postulates an almost identical partner differing only in spin and mass (we haven't ever observed these super-partners and so they must have higher masses). Their introduction solves several problems of the Standard Model, offering an explanation for the origin of mass and dark matter. Only as experiments probe the high energy frontier can we test these theories.

The Large Hadron Collider (LHC), built at CERN in Geneva, Switzerland, is exploring new energies to give sure answers, improve our nature knowledge and take us from current conjecture to concrete discovery (or, at least, we hope!). Taking over 20 years to complete, now it is for the first time successfully colliding together bunches containing billions of protons, millions of times each second. After a brief commissioning run during winter 2009, now it has reached energies never examined before (7 TeV), offering physicists peer-

less opportunities for fundamental physics. ATLAS is the largest detector ever built and records these collisions; more than 3000 physicists and engineers take part in the ATLAS Collaboration. Interactions between proton constituents probe and test the Standard Model for deviations or new phenomena with a precision never obtained. The most challenging task of particle physicists is to attempt to piece together what happens during collisions, in order to refine our knowledge of these interactions, looking to discover evidence of new ones and bringing light on a new energy range.

According to the supersymmetry theory, the hypothetical supersymmetric cascade decays would be characterized by final states with high missing transverse energy (E_T^{miss}) (due to the production of undetected neutral supersymmetry particles, the neutralinos, new sources of E_T^{miss} respect on the Standard Model) and energetic jets. Moreover, we could have the presence of leptons as decay products of SUSY particles. So, these are the main actors of a typical SUSY signature. In my work, I draw my attention on the two-lepton signature (characterized by the request of exactly two leptons in the final state): it is a very promising venue for the discovery of Supersymmetry and the best channel for the measurement of SUSY particle properties.

In my work I perform a two-lepton analysis on the data collected until the summer 2011 at $\sqrt{s} = 7$ TeV (1 fb^{-1}). In particular, I look for an eventual excess of lepton-pairs with identical flavour (e or μ) leptons over pairs with different flavour leptons beyond the Standard Model prediction. This technique, called "flavour subtraction", aims to find decay chains in supersymmetric events which can only produce lepton-pairs with identical flavour leptons. This analysis has two important and appreciated qualities: it allows to reduce, to cancel the most difficult and challenging Standard Model process, the $t\bar{t}$ production, and it has a small systematic uncertainty. The Monte Carlo predictions and the data-driven estimates of the Standard Model processes (backgrounds for a SUSY search) permit me to interpret the results and to set limits at 95% confidence on the number of excess identical flavour lepton-pairs, over those of different flavour, multiplied by detector acceptances and efficiencies, from supersymmetry.

My work is part of an ATLAS collaboration wide endeavour. The research of new physics at LHC is an exciting challenge and many groups are involved in it, in particular in the two-lepton analysis. For give more completeness and clearness at my work, I exploit also some results obtained by other members of the ATLAS "two-lepton" SUSY group. However, that use is limited to the data-driven estimation of Standard Model backgrounds less important for my results and analysis: the muon cosmic events (as we can see in section 4.7.2 this background is negligible and it will not considered in my analysis), the fake events (section 4.7.3) and $t\bar{t}$ events (section 4.7.5) that in the flavour subtraction analysis is canceled and so has a small contribution to the excess

of identical flavour lepton pair events.

In chapter 2 I give a brief presentation of Standard Model theory and of its limits and I introduce the supersymmetry and some aspects that make it so popular and interesting. In chapter 3 you can find an overview of the ATLAS detector and of the algorithms of identification and reconstruction of jets and leptons. The following chapter 4 contains the SUSY analysis: I present the event selection and some other features of the two lepton analysis and the (partially data-driven) Standard Model estimation necessary for the understanding and interpretation of the results. Then I explain the flavour subtraction analysis and the results obtained.

I conclude this introduction with a clarification. I perform my analysis only on the statistic of data collected until the summer 2011 (integrated luminosity equal to 1 fb^{-1}) and not on the entire statistic (4.7 fb^{-1}) collected during the 2011 as the analysis in which I was involved was concluded with the publication of a paper in October 2011 based on the reduced statistics. This analysis unfortunately did not yield a signal, and inside the ATLAS Collaboration it was deemed more effective, rather than to upgrade it to full statistics, to redirect the efforts to less inclusive analyses, such as, for the case of two leptons, to the search for the direct production of sleptons and of charginos and neutralinos.

Chapter 2

Standard Model and Supersymmetry

The Standard Model (SM) of particle physics [1] is a very successful theory able to well explain a great variety of phenomena that exist in nature. Many experiments and observations both in particle physics (with colliders reaching energy of the centre of mass higher and higher) and in astrophysics and cosmology give precise and accurate measurements in extraordinary agreement with the Standard Model predictions. However, in spite of the Standard Model has passed many tests of validity, confirming its intrinsic robustness and consistency, it shows some flaws: some natural mechanisms and observations are not completely and clearly described, some questions remain without an answer, unsolved. This doesn't mean that it is wrong, but that it is an effective theory working in a perfect way only in a range of low energy. Beyond this energy (of the order of TeV) we must introduce a new model, more general and more fundamental that can include the Standard Model as low energy limit. One of the most interesting and common accepted theory able to solve the Standard Model rifts and problems is the Supersymmetry (SUSY). In this chapter, I give a brief overview of the Standard Model (section 2.1), underlining some problematic aspects, especially in the explanation of particle masses (with the Higgs mechanism (section 2.1.1) and the hierarchy problem (section 2.1.2)) and I introduce the supersymmetry theory (section 2.2).

2.1 The Standard Model

The Standard Model is the current theoretical framework of particle physics. It is a gauge field theory, able to give a unified and organic description of the fundamental particles which make up our universe, of their properties and interactions.

It describes the fundamental particles dividing them in two different types, according to their internal angular momentum (spin):

fermions with spin 1/2: the fermions are the elementary constituents of the matter (they do not have an internal structure); they are grouped in two

categories: leptons and quarks. Both leptons and quarks are split in three generations (or families). Depending on the projection of the spin onto the direction of momentum (called helicity), we can divide them in two types with different symmetry and behaviour: left-handed (with momenta pointing in opposite direction) and right-handed (momenta in the same direction). It's interesting to note that the left-handed components are grouped in doublets, whilst the right-handed ones are singlets (as we can see in table 2.1). In the lepton family, electron, muon and τ lepton have charge -1, while the relative neutrinos are neutral. Neutrinos are predicted to have null mass. Leptons interact only via the weak and electromagnetic forces (unified into the electroweak force) whilst quarks are also able to interact via the strong force. The quarks have fractional charge: the up (u), charm (c) and top (t) quarks have charge $\frac{2}{3}e$, whilst the down (d), strange (s) and bottom (b) quarks have charge $-\frac{1}{3}e$. In addition to the flavour quantic number (that allows the subdivision in the six types reported in table 2.1), they carry a colour charge (related to the strong interaction) and appear in three different versions or colours degenerate in mass (red, blue and green). According to the strong interaction only the colourless state can exist in nature; therefore, the quarks can not be found isolated, but confined in bound states so that the resulting state is colourless: we can find a quark bound with an anti-quark to forming a meson or three (anti-)quarks forming a (anti-)baryon. These two particle types are grouped under the name of hadrons. Finally, the eigenstates of the electroweak symmetry $SU(2)_L$ of charge $-\frac{1}{3}e$ are not mass eigenstates, but a mixing of them parameterized by the Cabibbo-Kobayashi-Maskawa (CKM) matrix.

Bosons with spin 1: the fermions interact by exchanging vector bosons (reported in table 2.2):

- the photons γ are the neutral mediators of the electromagnetic force that affects all the charged particles. The coupling constant is the fine structure constant defined as

$$\alpha_{em}(m_e) = \frac{e^2}{4\pi\epsilon_0\hbar c} = 7.2973525376(50) \times 10^{-3} \tag{2.1}$$

  where e is the absolute value of the electron charge, ϵ_0 is the dielectric constant of the vacuum, $\hbar = \frac{h}{2\pi}$ where h is the Planck constant and c is the speed of light in vacuum.

- the vector bosons W^+, W^- (charged) and Z (neutral) are the mediators of the electroweak force that affect all the fermions. The coupling constant is:

$$\frac{G_F}{(\hbar c)^3} = 1.16637(1) \times 10^{-5} GeV^{-2} \tag{2.2}$$

Leptons		Quarks	
$\begin{pmatrix} \nu_{eL} \\ e_L^- \end{pmatrix}$	e_R^-	$\begin{pmatrix} u_L \\ d'_L \end{pmatrix}$	$u_R \quad d'_R$
$\begin{pmatrix} \nu_{\mu L} \\ \mu_L^- \end{pmatrix}$	μ_R^-	$\begin{pmatrix} c_L \\ s'_L \end{pmatrix}$	$c_R \quad s'_R$
$\begin{pmatrix} \nu_{\tau L} \\ \tau_L^- \end{pmatrix}$	τ_R^-	$\begin{pmatrix} t_L \\ b'_L \end{pmatrix}$	$t_R \quad b'_R$

Table 2.1: Fermion classification according to the Standard Model. They are divided in three families. Only the left-handed components are grouped in doublets and follow the $SU(2)_L$ symmetry. The quarks having charge $-\frac{1}{3}e$ are not the physical states (are not mass eigenstates), but a mixing of them according the matrix CKM.

Force	Boson	Mass [GeV]
Electromagnetic	Photons γ	0
Weak	$W^{\pm}$	80.399 ± 0.023
	Z	91.1876 ± 0.0021
Strong	Gluons g	0

Table 2.2: The gauge bosons, mediators of the electromagnetic, weak and strong forces described and included in the Standard Model. Also their masses are reported [3].

- the eight neutral and massless gluons are the mediators of the strong interaction that affects the quarks. They carry a colour charge (as the quarks). At first order in perturbation theory the QCD coupling constant of the strong interactions is

$$\alpha_S(\mu^2) = \frac{12\pi}{(33 - 2n_f) \cdot \ln(\frac{\mu^2}{\Delta^2})} \tag{2.3}$$

  where n_f is the number of fermions, μ is the scale of the interaction (usually the squared transferred four-momentum is taken), and Δ is an energy scale parameter, experimentally determined ($\Delta \approx 250$ MeV).

Separately, we collocate the Higgs boson. As we will see in the next section

2.1.1, it is the only boson with spin 0, introduced ad hoc to explain the observed particle masses causing the spontaneous breaking of the electroweak (EW) gauge symmetry. Until now, it has not yet been observed in any experiment.

The Standard Model is based on a local gauge invariance

$$G_{MS} = SU(3)_C \otimes SU(2)_L \otimes U(1)_Y \tag{2.4}$$

where $SU(3)_C$ is the colour symmetry, mediated by the eight gluons, $SU(2)_L \otimes U(1)_Y$ is the electroweak symmetry mediated by the vector bosons γ, $W^{\pm}$ and Z. $SU(2)_L$ characterizes the doublets of particles with left-handed helicity, while $U(1)_Y$ is connected to the hypercharge Y.

2.1.1 The Higgs boson

I conclude the overview of the Standard Model with the problem of the origin of the particle masses. The gauge theories predict massless gauge bosons and fermions, instead experimental observations have shown that the electroweak boson $W^{\pm}$ and Z have mass (80 GeV and 91 GeV respectively, as reported in table 2.2). Many measurements exist also for the masses of the fermions. The inclusion of massive fields into a gauge theory is nontrivial, because the introduction by hand of the usual mass terms of the form

$$m(\psi_L^+ \psi_R + \psi_R^+ \psi_L)$$

breaks the local gauge invariance $SU(2)_L$. So, for explaining the masses observed an alternative solution is provided in the model: the Higgs mechanism [4]. It spontaneously breaks the electroweak symmetry $SU(2)_L \otimes U(1)_Y$. This mechanism is based on the introduction of a new doublet of complex scalar fields, the Higgs doublet:

$$\phi = \begin{pmatrix} \phi^+ \\ \phi^0 \end{pmatrix} = \begin{pmatrix} \frac{\phi_1 + i\phi_2}{\sqrt{2}} \\ \frac{\phi_3 - i\phi_4}{\sqrt{2}} \end{pmatrix} \tag{2.5}$$

with ϕ_i real fields. With the introduction of these fields ϕ, the Lagrangian can be written as

$$L = -\frac{1}{4} F^{\mu\nu} F_{\mu\nu} + (D_\mu \phi)^\dagger (D^\mu \phi) - V(\phi) \tag{2.6}$$

where $V(\phi)$ is the scalar Higgs potential defined as

$$V(\phi) = \mu^2 \phi^\dagger \phi + \frac{\lambda (\phi^\dagger \phi)^2}{2} \tag{2.7}$$

If the mass parameter μ^2 is positive, then the potential has a single minimum value $V = 0$ at $\phi = \phi_0 = 0$. But this case is not interesting because we would have again massless particles. Instead, the Higgs doublet is designed to

have this mass parameter negative: $\mu^2 < 0$. In this case the minimum of the potential is not zero but lies in the complex plane on a circle of radius

$$|\phi| = v = \sqrt{-\frac{\mu^2}{\lambda}} \tag{2.8}$$

where we have also defined the vev v (vacuum expectation value) of the Higgs field ϕ. In figure 2.1 the mexican-hat profile of the Higgs potential for $\mu^2 < 0$ is shown. The fact of these minima are not zero is the cause of the symmetry breaking: if a change of state occurs, with a transition from high energy density to low energy density (such as in the early universe when there was the particle formation and their mass acquisition), the field will spontaneously fall into a minimum of the potential and assumes a not zero vev.

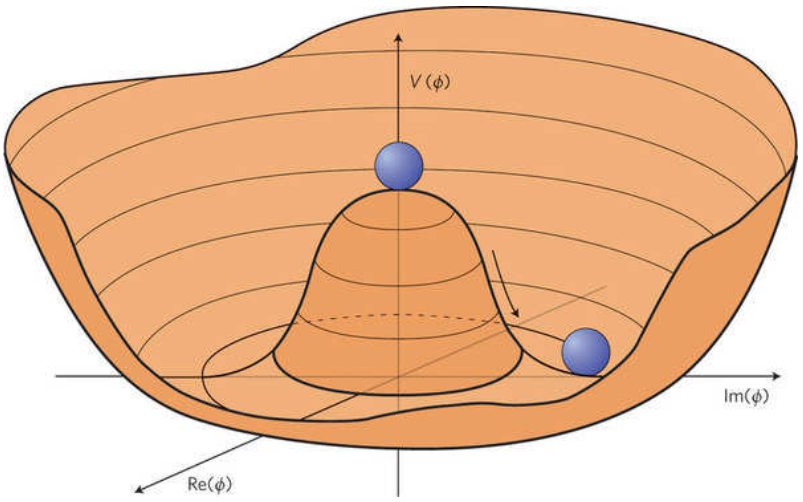

Figure 2.1: Higgs potential $V(\phi)$ for $\mu^2 < 0$. For a fixed value of λ the potential is presented against the real and imaginary parts of ϕ. It show a Mexican-hat or champagne-bottle profile with a minimum that not occurs at zero, but in a ring with radius $|\phi| = \sqrt{-\frac{\mu^2}{\lambda}}$ [5].

At its minimum, the field can be written as:

$$\phi = v + \frac{1}{\sqrt{(2)}}(\phi_1 + i\phi_2) \tag{2.9}$$

Substituting in the Lagrangian (eq. 2.6), for an initial massless field A^μ we find mass terms of the type $g^2v^2A^\mu A_\mu$ and a single physical scalar field ϕ_1 with mass $\sqrt{\lambda v^2}$. With a null minimum value for v, we could not have vector bosons with mass. If the gauge mass term defines completely v, unfortunately the parameter λ is the free parameter of the theory and so we can not make predictions on the mass of the Higgs boson. It's interesting to note that of the four real fields of the Higgs doublet (2.5), three of them are used to give mass to the three vector bosons W^+, W^- and Z, while the fourth corresponds

at the physical Higgs boson. It's possible to write the boson masses in the following way:

$$m_W = \frac{gv}{2}$$

$$m_Z = \frac{\sqrt{g^2 + g'^2}v}{2} \tag{2.10}$$

$$m_\gamma = 0$$

$$m_H = \sqrt{-2\mu^2} = \sqrt{2\lambda}v$$

where g is the weak coupling constant of $SU(2)_L$, and g' is the coupling constant of $U(1)_Y$. So we can write the vev v of the Higgs field as

$$v = \frac{2m_W}{g} = (\frac{1}{\sqrt{(2)}G_F})^{\frac{1}{2}} \approx 246GeV \tag{2.11}$$

where G_F is the Fermi coupling constant.

Investigating the coupling of the scalar Higgs field, we can note that self-coupling terms of the scalar exist ($\lambda\phi^4$), but, depending on λ, they are unpredictable. On the other hand, the coupling terms with the gauge bosons are depending only on g and v ($vg^2\phi_i A^\mu A_\mu$ and $g^2\phi_i^2 A^\mu A_\mu$) and so their strengths are completely predicted. The prediction of the coupling strength of the scalar to a pair of gauge bosons is fundamental, as it has important experimental consequences: if this mechanism works in nature and so the Higgs boson exists, then we can observe its decay via pairs of gauge bosons.

The inclusion of mass terms for the chiral fermion fields f creates similar problems as those seen for the bosons. However, the introduction of the Higgs doublet into the fermion sector of the Lagrangian gives terms of Yukawa coupling between the Higgs field and the fermions of the form

$$L = -g_f(\bar{f}_L \cdot \phi)f_R + h.c.$$

where g_f is the Yukawa coupling constant and is characteristic of the considered fermion. So, since the Higgs field assumes a vacuum expectation value different from zero, we find the fermion mass

$$m_f = \frac{g_f v}{\sqrt{2}}$$

Therefore, the Yukawa couplings are determined by the measured masses of the fermions and so the production and decay rates of the Higgs boson through fermion pairs are predicted in the SM.

2.1.2 The limitations of the Standard Model

The Standard Model provides an accurate description of many natural phenomena and a great number of experiments in various field (particle physics, astrophysics) have given important confirmations of its predictions with more and more accuracy and precision. However, the Standard Model presents some flaws. I report some of the problems that the SM leaves unsolved:

- many experimental observations have collected evidence of the presence of the dark matter in the universe and have found that it is the main component of the matter. No particle in the SM is a good candidate for explaining and making up the dark matter [6];
- the asymmetry matter-antimatter in the universe can not quantitatively explained in the SM. The sources of CP violation of the SM, combined in the CKM matrix [2], are too small;
- the flavour oscillations of the neutrinos, observed for the solar, atmospheric and from reactors neutrinos, can be explained and realized only if the neutrinos have a not zero mass. According to the SM, they should be massless;
- there is no reason why only three generations of fermions exist;
- the existence of a fourth force, the gravitational one, is not accounted for:
- the high number (19) of free parameters of the theory to be determined by measurements reduces the predictive power of the theory. A more elegant and general theory of nature would predict these parameters;
- we would like to have an unification of the three coupling constants of the fundamental forces[1] at a high energy scale [7], but in the SM this doesn't happen (see figure 2.2);
- the hierarchy problem explained in more detail in the following section.

The hierarchy problem

The hierarchy problem [8] is maybe the main problem that induced the physicists to design a new theory beyond the Standard Model. A calculation of the mass of the Higgs boson from the standard model Lagrangian, gives for the tree-level, a Higgs mass $m_H = \sqrt{-2\mu^2}$. However, at higher orders (by

[1] According to the Grand Unified Theory (GUT) at high energy there is a simple gauge group with only one coupling constant that at some energy is spontaneously broken to produce the $SU(3)_C \times SU(2)_L \times U(1)_Y$ symmetry group observed at the electroweak energy scale.

considering radiative corrections through loop diagrams), every particle which couples to the Higgs must be included giving a mass parameter

$$\mu^2 = \mu_0^2 + \delta\mu^2 \tag{2.12}$$

where $\delta\mu$ represent the contribution from the radiative corrections. However, the fermionic contribution gives an integral over all possible momentum states which diverges quadratically. Obviously, it not acceptable and it hasn't a physical sense. In order to cancel this divergence, we can suppose that, at a scale of energy Λ, a new more fundamental theory and so new physics appear (in fact, as seen, the many problems arisen in the Standard Model theory make very unlike that this model is correct up to the Planck scale). Therefore, at energy greater than Λ the masses can be calculated in terms of parameters of this new theory. So, imposing a cut-off Λ for the SM radiative corrections, we can renormalized the divergent terms; in fact we find corrective terms quadratically sensitive to the scale Λ

$$m_H^2 = (m_H^2)_0 + cg_f^2(-2\Lambda^2 + 6m_f^2 \ln(\Lambda/m_f) + ...) \tag{2.13}$$

Since there are contributions from loops including scalars and other particles coupling to the Higgs, these various terms can cancel out the divergent terms. However, in order to have this cancelation, the parameters must be very precisely fine tuned and also $(m_H)_0$ must be fixed to obtain the mass observed for the boson vectors and other particles. This cancelation becomes more and more unnatural with the increasing of the cut-off scale (hierarchy problem). To solve the hierarchy problem with a more natural and probable cancelation, an energy cut-off of ~ 1 TeV is required.

The hierarchy problem and the other limitations of the Standard Model suggest that the Standard Model can not be a fundamental general theory, but only an effective theory valid at energy scale below the TeV. So, a new more fundamental theory must be designed, able to extend the Standard Model at scale beyond the TeV scale. One of the most popular, promising and common accepted extensions to the Standard Model and the main topic of my thesis is the Supersymmetry.

2.2 The Supersymmetry

Supersymmetry (SUSY) [9] is the more promising extension of the Standard Model beyond the electroweak energy scale. It preserves all the good features of the SM and can give answers to the questions let unsolved by the SM. It is a generalization of the space-time symmetry of the quantum field theory and introduces a (super-)symmetry between the components of the matter (the fermions) and the boson vectors, mediators of the fundamental forces. According to the SUSY theory, for each fermion of the SM there is a boson super-partner differing only for the spin (0 instead of $\frac{1}{2}$) and for each boson of the SM there is a fermionic super-partner (with spin $\frac{1}{2}$ instead of 1). In this overview, I considerer the Minimal Supersymmetric Standard Model (MSSM) scenario, that is the supersymmetric theory which adds the minimum extra particle content to the Standard Model [10].

The SUSY generators are the Majorana spinors Q_α (with α = 1, 2, 3, 4) which change the particle spin, transforming a bosonic state into a fermionic one and a fermionic state into a bosonic one

$$Q_\alpha|fermion>=|boson> \qquad (2.14)$$
$$Q_\alpha|boson>=|fermion>$$

In addition to the usual commutation rules, they satisfy also anti-commutation rules in order to solve some theoretical problems about the dimension of the particle spectrum (Coleman-Mandula theorem [11] [12]).

At this point, it's necessary to introduce the supersymmetry nomenclature for a clearer presentation of the zoo of new particles. Each superpartner is indicate with the same symbol (letter) of the SM counterpart, but with a tilde $\sim$ over the top of the symbol. The superpartners of the SM fermions, called sfermions, take the prefix s- and so we have for example the sleptons and squarks. The superpartners of the SM vector bosons take a suffix -ino and so we have the gluinos and gauginos (for example the Winos and the Zino superpartners of W and Z respectively).

According to the supersymmetry theory, the SM particles are grouped in irreducible representations of the supersymmetry algebra, called supermultiplets; the superpartners of the SM particles belong to the same multiplet. There are two types of supermultiplets: chiral supermultiplets with fermions (with spin $\frac{1}{2}$) and their superpartners (sfermions of bosonic nature with spin 0) and vector supermultiplets with vector gauge bosons (with spin 1) and their superpartners (gauginos with spin $\frac{1}{2}$). Members of the same supermultiplet must have equal masses and the same electric charge, weak isospin and colour degrees of freedom. Moreover, the supermultiplets must have equal numbers of fermionic and bosonic degrees of freedom. So, we can write the MSSM supermultiplets:

* chiral supermultiplets quark-squark $q_{L,R}$, $\tilde{q}_{L,R}$;

* chiral supermultiplets lepton-slepton $l_{L,R}$, $\tilde{l}_{L,R}$;

* two supermultiplets Higgs-Higgsino Φ_1, Φ_2 e $\tilde{\Phi}_1$, $\tilde{\Phi}_2$;

* vector supermultiplets g, $\tilde{g}$; W^i_μ, $\tilde{W}^i_\mu$; B_μ, $\tilde{B}_\mu$;

In order to give mass to both the up and down type quarks in the Standard Model two Higgs doublets are necessary [13]. Of the eight degrees of freedom available (four per doublet), three are used to give mass to the vector bosons ($W^\pm$ and Z), the remaining five (instead of the only of the Standard Model where we have only one Higgs doublet) give origin to five Higgs physical bosons:

- two scalar neutral (CP-even) Higgs bosons h^0 and H^0;
- one pseudo-scalar (CP-odd) A^0;
- two scalar charged Higgs bosons H^+ and H^-.

While in the Standard Model we have only one scalar field introduced ad hoc to explain the formation of the mass, in the SUSY theory we have more scalar fields and so the introduction of the Higgs doublets seems more natural. The second point is connected to the gaugino sector: in addition to the eight gluinos, we have the higgsino and gauginos. The gauginos are the Winos (superpartners of the $W^\pm$), the Bino (superpartner of the abelian gauge boson of $U(1)_Y$, B_μ) and the Zino (superpartner of the Z). According to the MSSM description, they are not mass eigenstates, but they are in nature mixed to form the real physical mass eigenstates: the mixing between charged Winos and the charged higgsinos ($\tilde{\Phi}_1^+$ and $\tilde{\Phi}_2^-$) gives the four charged charginos $\tilde{\chi}^\pm_{1,2}$, whilst the mixing between the Zino $\tilde{W}^0$, the Bino $\tilde{B}^0$ and the neutral higgsinos ($\tilde{\Phi}_1^0$ and $\tilde{\Phi}_2^0$) give the four neutral neutralinos $\tilde{\chi}^0_{1,2,3,4}$.

After this introduction, we can see the solutions given by the SUSY at the problems of the Standard Model.

2.2.1 Standard Model problem solving

The main problem in the Standard Model is the hierarchy problem (see section 2.1.2): when we calculate the radiative corrections to the Higgs mass, in order to guarantee an Higgs mass of the order of a few hundred GeV we must introduce an artificial fine tuning to cancel diverging terms. In the SUSY, this problem is solved in a natural way: in fact, for calculating the radiative corrections we must take into account the loops of all the particles coupling with the Higgs boson. According to the supersymmetry, for each fermionic (divergent) contribution we have a scalar (boson) one of the form

$$(\Delta m_H^2)_{sc} = c g_{sc}(\Lambda^2 - 2m_s^2 \ln(\Lambda/m_s) + ...) \tag{2.15}$$

Comparing this term with the similar fermionic one in equation 2.13, we can observe that the different spin gives an opposite sign. If the coupling constants

are related by the relation $g_f^2 = g_{sc}$, when we sum the two contributions we have an appreciated cancelation of the leading divergent terms. So, this cancelation is natural and included in the theory. This cancelation must always be preserved. To keep the remaining logarithmic correction in the electroweak scale (100 GeV or below), the masses of the new supersymmetric particles must be less than ~ 1 TeV [14].

A second solution provided by the supersymmetry is the unification of the coupling constants of the three fundamental forces (electromagnetic, weak and strong). As we can see in figure 2.2, with only the Standard Model particles it remains partial, uncomplete; instead, with the introduction of the sparticles we have the hoped unification at the scale of grand unification ($\Lambda_{GUT} \sim 10^{16}$ GeV). In fact, the coupling strengths vary with the increasing of energy and this running is dependent on the particle states accessible at any given energy scale. The introduction of new particles at the TeV scale is necessary to realize the force unification.

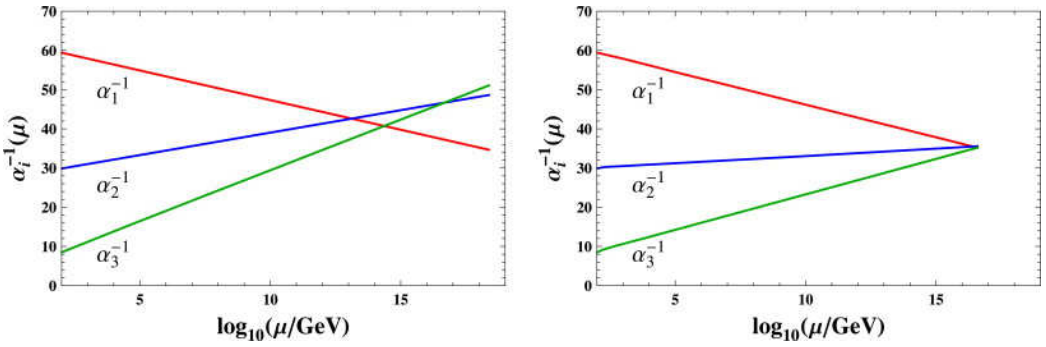

Figure 2.2: Gauge coupling unification according the Standard Model on the left and according to the SUSY theory on the right, where α_1, α_2 and α_3 are proportional to the coupling constants of the three fundamental forces electromagnetic ($U(1)_Y$), weak ($SU(2)_L$) and strong ($SU(3)_C$) respectively. The difference in the running for SUSY is the inclusion of supersymmetric partners of Standard Model particles at scales of order a TeV. The unification is realized only with the introduction of SUSY particles at $\Lambda_{GUT} \approx 10^{16}$ GeV [15].

In a model conserving the lepton L and baryon B numbers, it is possible introduce a new multiplicative quantic number, called R-parity [16]. It is defined as

$$R = (-1)^{3(B-L)+2s}$$

for a particle of spin s. All Standard Model particles and the Higgs boson have an R-parity equals to +1 (even exponent), while all the SUSY particles have an R-parity equals to –1 (odd exponent). If we assume the conservation of the R-parity, we have two important consequences: since any initial state

produced at the LHC have an R-parity of +1 ($R(p) * R(p) = 1 * 1 = 1$), the sparticles (having R-parity –1) must be pair produced, and the energy of the decaying particle must also be twice the mass of the produced supersymmetric particles. If a supersymmetric particle decays, it must decay to particles with a global R-parity of –1 and so each intermediate state of the sparticle decay has to contain at least one sparticle (and in general, an odd number). Moreover, in the final state we must have supersymmetric particles and so the decay chain ends with the lightest supersymmetric particle (LSP). It must be stable. If the LSP is electrically neutral and weakly interacting, it can be an optimal candidate for the dark matter [17]. In many models the LSP is the lightest neutralino $\tilde{\chi}_1^0$.

Another cosmological problem as the entity of the matter-antimatter asymmetry present in the universe can be explained in the SUSY scenario. In fact, the introduction of new particles and fields can provide new sources of CP violation, responsible of this asymmetry.

2.2.2 Supersymmetry breaking

If the supersymmetry was an exact symmetry, the only difference between a SM particle and its superpartner would be the spin (fermion $\leftrightarrow$ boson). In particular, they should have the same mass. For example, we could easily find (and detect) a selectron with the same mass and behaviour as the electron, but with spin 0. Since the supersymmetry particles have not been ever observed, the supersymmetry must be broken. So, in order to give mass to all the particles and sparticles are necessary two mechanisms of symmetry breaking: the SUSY breaking at higher energy and then the electroweak symmetry breaking at the scale of the Higgs vacuum expectation value (246 GeV). We don't know the energy scale of the SUSY breaking; we only know that the masses of the new SUSY particles must be $\sim$ TeV in order to keep natural the mass splittings between the particles and their superpartners, generate a correct Standard Model Higgs vacuum expectation value and continue to provide a solution for the hierarchy problem. This type of breaking is called "soft" supersymmetry breaking [18].

The mechanism of SUSY breaking is unknown. The attempt of introducing a spontaneous symmetry breaking failed since it allows the violation of the electric and colour charges and a not zero mass for the photon. For describing the SUSY breaking, it was introduced an effective Lagrangian containing all possible supersymmetric mass breaking terms. With the increasing of the number of particles and interactions, also the number of parameters increases: this effective Lagrangian introduces 105 new parameters. Starting from this complete effective Lagrangian, I present two possible symmetry breaking mechanisms: Supergravity and gauge mediated supersymmetry breaking. Both the mechanisms introduce a new set of fields at a high energy scale (the hidden

sector), which interact weakly with the fields of the MSSM (the visible sector).

The SUSY breaking happens in the hidden sector and is communicated to the visible one via different mediators. According to supergravity (SUGRA), the mediator is the gravitino (particle of spin 3/2) and, in general, the gravity [19]. In the simplest model (minimal SUGRA, mSUGRA), at the Planck scale, the free parameters of the lagrangian are reduced to five:

- m_0, the common mass of all scalar sparticles;
- $m_{1/2}$, the common mass of all gauginos;
- the supersymmetry breaking trilinear $Hf\bar{f}$ coupling terms and the supersymmetry conserving Yukawa couplings are proportional with constant A_0;
- the ratio of the vacuum expectation values of the two Higgs doublets $\tan\beta = \frac{v_2}{v_1}$;
- the sign of higgsino mass parameter μ.

The best quality of mSUGRA is the small number of free parameters and its capability to easy determinate the MSSM particle spectrum and their interactions.

In Gauge Mediated Supersymmetry Breaking (GMSB) [20], messenger particles are gauge bosons and SM fields; they communicate with the MSSM (visible sector) via ordinary gauge interactions. In this model, the number of free parameters is six:

- F_m defines the scale of supersymmetry breaking;
- M_m defines the messenger scale;
- N_5 is the number of messenger supermultiplets;
- the ratio of the vacuum expectation values of the two Higgs doublets $\tan\beta = \frac{v_2}{v_1}$ (as in mSUGRA model);
- the sign of higgsino mass parameter μ (as in mSUGRA model);
- C_{grav} gives the couplings for decays into gravitinos.

The gravitino is not related to the soft term in Lagrangian and so is expected to be very light. Every final state will contain a gravitino, but the weak coupling between the gravitino and other sparticles will give it a long lifetime.

2.2.3 Supersymmetry searches

We have introduced the supersymmetry and its main features. We have also seen some of the aspects that make the theory so interesting and discussed. Now, finally, we try to follow a sparticle decay chain and to understand the typical signature of a supersymmetry event and how it can be revealed and detected at a collider. I also give a brief overview on the SUSY searches at LEP and Tevatron.

If we assume the conservation of R-parity, at a collider the supersymmetry particles (such as the squarks and gluinos) are initially produced in couples, giving rise to two independent cascade decays (legs). These decays produce many particles (including the LSP), through a sequence of successive two-body decays. The resulting final states are characterized by leptons, energetic jets and high missing energy E^{miss} (a measure of the unbalance in the total event momentum, resulting from the production of invisible undetected particles like neutrinos and the LSP). The SUSY decay cascades can give unusual signatures, very different to anything predicted by the Standard Model. In particular, the LSP and so the E^{miss} signature are the key elements for these SUSY analysis.

If the R-parity is not conserved, as supposed in the R-parity-violating (RPV) models, the LSP decays into SM particles and so the E_T^{miss} signature can't be used for reveal SUSY events. The only way to recognize the SUSY events in these models is the rise of energetic lepton or hadronic jet multiplicities. This signature would guarantee a good rejection of the Standard Model backgrounds.

Searches at e^+e^- colliders: LEP

The large e^+e^- collider, LEP, was in operation at CERN from 1989 to 2000, first at a center of mass energy near the mass of the Z boson, 91.2 GeV, and progressively up to a center of mass energy of 209 GeV. It was formed by four detectors, ALEPH, DELPHI, L3, and OPAL; each one collected ~ 1 fb^{-1} of data [21]. All SUSY particles, except for the gluino, are produced via electroweak interactions. The search is therefore naturally directed toward the lightest ones, typically the NLSP (Next to Lightest Supersymmetry Particle, the second lightest sparticle after the LSP) and the LSP, and the results are interpreted in a fairly model-independent way. Further specifying the model, various search results can be combined to obtain constraints on the model parameters.

In e^+e^- collisions, the missing energy E_{miss} can be directly inferred as $\sqrt{s} - E$, from the center of mass energy $\sqrt{s}$ and from the total energy E of the visible final state products. Similarly, the missing momentum P_{miss} is the opposite of the total momentum of those products. The reason is that the (anti-)electrons are elementary particles and so we know very well them and their properties.

During the runs at the center of mass energy of the Z, the SUSY analysis

were addressed to the search for deviations of the Z width respect to the Standard Model prediction; the sought departures were not observed and so the physicists could only set lower limits on the supersymmetry particle masses. At higher energy, decays of SUSY particles into SM particles or into LSP were looked for; the sought signature was characterized by the presence of isolated leptons and jets and missing energy E^{miss} and momentum P^{miss}. The backgrounds for these SUSY analyses are mainly two:

- the diphoton interactions, where the two γ are emitted from the beam electrons and, interacting, form a leptonic or hadronic system characterized by a low invariant mass. The main part of these particles are produced in the beam direction and so it can't be detected. This visible energy, not recorded in the detector, is interpreted as missing energy and can be wrongly associated with SUSY particles (LSP).

- The production of four fermions via resonance of one or two bosons (W or Z) gives origin at decays involving neutrinos and electrons escaping from the detector; therefore, this Standard Model process increases the missing energy.

The selection cuts on E^{miss} and P^{miss} reduce and almost cancel these backgrounds.

No SUSY signals have been detected [21]. In table 2.3 I report the lower limits set by LEP for some SUSY particle masses. The results are obtained in the MSSM scenario.

Searches at hadron colliders: Tevatron and LHC

At hadron colliders (as LHC), we expect high cross sections for the squarks and gluinos production. Gluinos are Majorana particles and decay with equal probability into a particle-antisparticle ($q\bar{\tilde{q}}$) or a sparticle-antiparticle pair ($\tilde{q}\bar{q}$). Then, if kinematically allowed, the squark decay into $q\tilde{g}$ is dominant. Otherwise the squark can decay into a quark plus a neutralino or a quark plus a chargino. All the neutralinos (obviously except the LSP) and the charginos produced from the squark will themselves decay to any lighter neutralino or chargino, and a Higgs scalar or electroweak gauge boson. Gauginos may also decay into lepton-slepton, neutrino-sneutrino or neutrino-slepton pairs. Neutralino decays to quark-squark pairs are less favoured. Sleptons decay into a lepton and a neutralino, or a neutrino and a chargino.

In hadron collisions the center of mass energy of the colliding partons is not known. Only its probability density can be determined, by making use of universal parton distribution functions (PDFs) obtained from fits to a large set of experimental data. Since most of the beam remnants escape undetected in the beam pipe, only conservation of momentum in the plane transverse to the beam direction can be used, and canonical SUSY signals will be searched for in events with large missing transverse energy E_T^{miss}.

Sparticle	Conditions	Limits (GeV)	Experiment
$\tilde{\chi}_1^{\pm}$	$m_{\tilde{\nu}} > 500$ GeV/c^2	103	LEP2
	$m_{\tilde{\nu}} > M_{\tilde{\chi}^{\pm}}$	85	LEP2
	$\forall m_{\tilde{\nu}}$	45	width Z
	$M_2 < 1$ TeV/c^2	99	LEP2
	RPV	88	LEP2
$\tilde{\chi}_1^0$	$\forall \tan\beta$, $m_{\tilde{\nu}} > 500$ GeV/c^2	39	LEP2
	$\forall \tan\beta$, $\forall m_0$	36	LEP2
	$\forall \tan\beta$, $\forall m_0$, Higgs SUGRA	59	LEP2 combined
	GMSB	93	LEP2 combined
	RPV	23	LEP2
$\tilde{e}_R$	$\Delta M > 10$ GeV/c^2	99	LEP2 combined
$\tilde{\mu}_R$	$\Delta M > 10$ GeV/c^2	95	LEP2 combined
$\tilde{\tau}_R$	$M_{\tilde{\chi}_0^1} < 20$ GeV/c^2	80	LEP2 combined
$\tilde{\nu}$		43	width Z
$\tilde{\mu}_R$, $\tilde{\tau}_R$	stable	86	LEP2 combined
$\tilde{t}_1 \to c\tilde{\chi}_1^0$	$\forall\theta_{mix}$, $\Delta M > 10$ GeV/c^2	95	LEP2 combined
	$\forall\theta_{mix}$, $\forall\Delta M$	59	ALEPH
$\tilde{t}_1 \to bl\tilde{\nu}$	$\forall\theta_{mix}$, $\Delta M > 7$ GeV/c^2	96	LEP2 combined

Table 2.3: LEP lower limits on some sparticle masses. With "GMSB" I mean the results obtained in the Gauge Mediated Supersymmetry Breaking models [22], whilst with "RPV" those in the R-parity-violating models. All the limits are set in the MSSM scenario [23] [24].

Now, I present the most important results obtained by the Tevatron. The Tevatron is a $p\bar{p}$ collider located at Fermilab. It includes two multi purpose detectors: CDF and D$\emptyset$. After a first run at a center of mass energy of 1.8 TeV, which ended in 1996, and during which the two detectors collected about 110 pb^{-1} of data each, both the accelerator complex and the detectors were substantially upgraded for Run II, which began in 2001. The center of mass energy was raised to 1.96 TeV and the instantaneous luminosity reached the level of 4×10^{32} cm^{-2} s^{-1}; almost 12 fb^{-1} of data has been collected by each experiment [25]. The Tevatron ceased operations on 30 September 2011, due to budget cuts; it is not as powerful as the LHC, which began operations in early 2010. The main ring of the Tevatron will probably be reused in future experiments and its components may be transferred to other particle accelerators.

I report the main SUSY analyses performed by the Tevatron experiments [26] [27].

Scalar bottom quark The lightest scalar partners of the third generation (stop and sbottom) may be light enough to be produced copiously at the Tevatron. D$\emptyset$ has searched for a scalar bottom quark assuming it decays

exclusively into a bottom quark and the lightest neutralino (LSP), resulting in events with two b-jets and large E_T^{miss}. The SM background processes are represented by the production of W or Z bosons in association with b-jets and top quark production. No excess of events is observed above the SM predictions which allows DØ to exclude a 247 GeV scalar bottom for a massless scalar neutralino and a 110 GeV neutralino for $160 < m_{\tilde{b}} < 200$ GeV.

Scalar top quark Scalar top quarks have been searched for in various decay channels. The sought signature and the event selection cuts depend on the chosen channel. The Standard Model backgrounds vary according to the decay channel: the main backgrounds are Drell-Yan processes and diboson and top quark pair production. For example, the search for the three-body decay $\tilde{t} \to b\ell\tilde{\nu}$ allows to exclude scalar top masses below 210 GeV for a scalar neutrino mass below 110 GeV.

Trileptons The trilepton final state is known as the "SUSY golden mode" because of the small background level. It can be obtained by the production of a $\tilde{\chi}_1^{\pm}$ and $\tilde{\chi}_2^0$ pair that decay via W and Z bosons (if sleptons are heavy) or via sleptons. CDF analysed events with two electrons or two muons requiring either the third lepton to be an identified lepton (e, μ or τ decaying hadronically) or an isolated track. No excess of events has been observed over the expectation leading to a limit on the cross section times branching ratio into three leptons of 0.1 pb. Interpreted within the mSUGRA model, this limit excludes a $\tilde{\chi}_1^{\pm}$ mass below 168 GeV.

As seen, until now we have no experimental evidence of the existence of the particles predicted by the Supersymmetry theory. The LHC is perhaps our last hope, the detector that could clear and solve many doubts and problems and unveil if the Supersymmetry exists. In fact, it opens a new era allowing the physicists to explore regions never reached before. Its nominal center of mass energy is 14 TeV (see the next chapter 3).

LHC is composed by four main detectors: ATLAS, CMS, LHCb and ALICE. The SUSY analyses at LHC are performed with the two general purpose detectors, ATLAS and CMS. The SUSY analyses of the ATLAS and CMS detectors present many similar aspects (see references in [28]). Here, I focus my attention on the ATLAS SUSY analyses. Assuming the conservation of R parity, the main ATLAS SUSY searches [29] [30] are:

0 lepton The 0-lepton analysis [31] aims at the strong production of squarks and gluinos decaying to the LSP. The main SM background processes are $W \to \tau\nu$, $Z \to \nu\nu$, hadronic tau decays in top events and the multijet QCD background.

Multijet The multijet search [32] focuses on long decay chains of gluinos. The main SM background is the multijet QCD background.

1 lepton Leptons can be produced if W or Z bosons or sleptons occur in the decay chains of the squarks or gluinos. The dominant backgrounds for one lepton analyses [33] are top pair production, W+jets, multijet QCD production.

Two leptons The two lepton analysis [34] is described in more detail below.

***b*-jet analysis** Large mixing between $\tilde{q}_R$ and $\tilde{q}_L$ can yield to $\tilde{b}_1$ being significantly lighter than other squarks. These analyses [35] are looking for b-jets as the sbottom or stop decay usually results in a b-quark. Sbottoms or stops can be produced either via gluino decay (gluino mediated production) or in a direct pair production. The main background processes are $t\bar{t}$ and W+(heavy flavour)jets.

In my analysis I'm interested in events producing two leptons. So I better summarize the decays producing two leptons in the final states and the possible analysis searching for two-lepton SUSY events. Neglecting decays involving the top quark, as already seen, leptons are produced in SUSY cascade through the decays of the charginos and neutralinos. The main processes through which they occur are:

- $\tilde{\chi}_i^0 \to \ell^{\pm}\nu\tilde{\chi}_j^{\mp}$
- $\tilde{\chi}_i^{\pm} \to \ell^{\pm}\nu\tilde{\chi}_j^0$
- $\tilde{\chi}_i^0 \to \ell^{\pm}\ell^{\mp}\tilde{\chi}_j^0$
- $\tilde{\chi}_i^{\pm} \to \ell^{\pm}\ell^{\mp}\tilde{\chi}_j^{\pm}$

So, a two-lepton event can be obtained either through the last two decays on a single leg or one of the first two decays on both legs. The two final state leptons can have same or opposite sign, and identical or different flavour, thus yielding four possible configurations. Each configuration selects a specific mix of the four decays above. From these lepton combinations derive two main independent analysis:

* one analysis searches for same-sign (SS) lepton pairs. The only way to have this signature is one of the first two single-lepton decays on both legs of the event. This happens either through the pair production of two same-sign squarks, or via initial states involving gluino decays. Therefore in models where sparticle production is dominated by the production of at least one gluino, the same-sign lepton pair production can be significant. This is not true in the Standard Model, where same-sign leptons can only be produced through the decay of heavy quarks or in processes

implying the production of three leptons. The backgrounds expected to such a search from the Standard Model are therefore small. Obviously, if squarks and gluinos have low branching ratio (BR) into a single lepton, the requirement that the two leptons be produced in two different legs of the event may considerably reduce also the SS SUSY signal and so the statistical power of this analysis.

* The second analysis searches for inclusive opposite-sign (OS) lepton pairs; all the possible decay chains contribute to this signal that is therefore expected to be significant. However, also the Standard Model backgrounds are higher.

Concluding, until now any experiment has never observed any supersymmetry particle. Because of the SUSY breaking they have masses higher than the energy accessible to colliders and experiments existing before the LHC. For solving the hierarchy problem and having a soft SUSY breaking, the sparticle masses are expected to be ~ 1 TeV. So, finally, now the LHC has the possibility and capability to discover and detect them. If they exist in nature.

Chapter 3

The ATLAS detector at the LHC

ATLAS (A Toroidal LHC ApparatuS) is one of the four main experiments at the Large Hadron Collider (LHC) at CERN, near Geneva. In this chapter I give a brief introduction to the LHC collider and its physics environment, together with a description of the ATLAS detector. Moreover, I describe the methods for the reconstruction and identification of physics objects of interest for my work (leptons, jets and missing transverse energy E_T^{miss}).

3.1 The Large Hadron Collider (LHC)

The Large Hadron Collider (LHC) project was approved by CERN's Council in December 1994, but only in November 2009 it has collected its first collision.

The LHC is designed to provide proton-proton (pp) as well as heavy ions (Pb-Pb) collisions. In pp mode, it has been designed to collide proton beams together at a luminosity of 10^{34} cm^{-2}s^{-1} at a centre of mass energy of 14 TeV, increasing almost an order of magnitude the maximum achievable collision energy, previously reached by the Tevatron (1.96 TeV). A new era for particle physics is open. In Figure 3.1 the production cross sections of some Standard Model processes at proton-(anti)proton colliders are given. The cross section for Higgs boson production at the LHC is of particular interest, since in the case of large Higgs mass it can increase by many orders of magnitude with respect to the Tevatron. In general, the increase in collision energy from the Tevatron to the LHC results in a huge increase in the production cross section for any new particles in the mass range with mass greater than 100-150 GeV. This provides sensitivity to a large region of parameters space (including many theories beyond the Standard Model, such as the supersymmetry) that was inaccessible to the Tevatron.

The LHC is located at CERN, in the existing 26.7 km long tunnel built for the Large Electron-Positron (LEP) collider. The proton beams are kept in

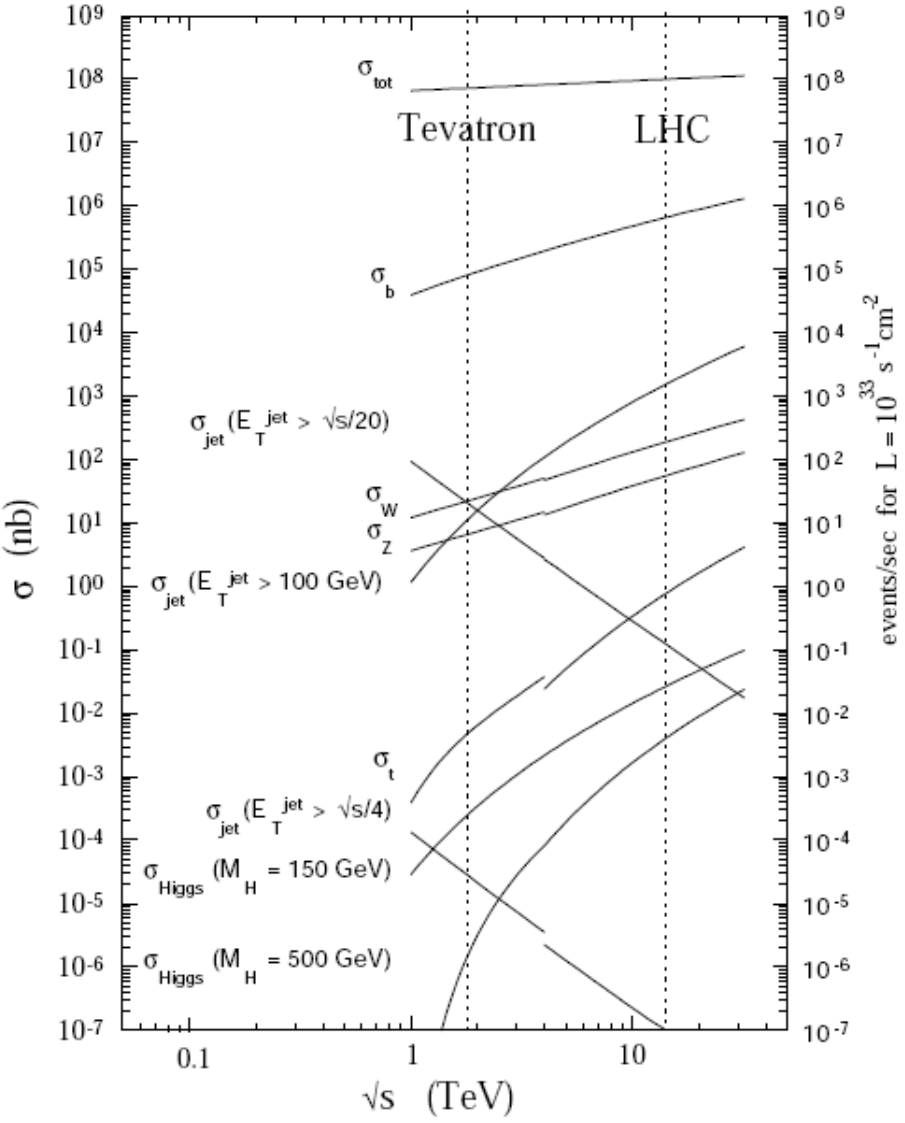

Figure 3.1: Cross section for hard scattering versus the centre of mass energy ($\sqrt{s}$). The right scale represents the expected event rate at a luminosity of 10^{33} cm^{-2} s^{-1} [36].

orbit and bent by superconducting magnets operating at a temperature of 1.9 K and fields above 8 T and are accelerated by a 400 MHz superconducting cavity system. The LEP tunnel has eight possible interaction points, of which four are active at the LHC, where are located the main experiments of LHC: two general purpose experiments, ATLAS and CMS, positioned at Point 1 and Point 5 respectively, with focus on the discovery of new physics; LHCb is located at Point 8 and, as the name suggests, it is designed to study B-physics; ALICE (located at Point 2), is a dedicated experiment for the study of quark-

gluon plasma, produced in the heavy ions (Pb-Pb) collisions. A schematic layout of the LHC is shown in Figure 3.2.

The LHC started operations on 10 September 2008. Unfortunately, immediately after, again during the commissioning phase, an important accident imposed a one year stop. During autumn 2009 operations started again, culminating in the first collisions at $\sqrt{s}$ = 900 GeV, recorded by the LHC experiments on 23 November 2009, and followed shortly after by collisions at 2.36 TeV, the highest energy ever reached before (passing for the first time the energy of Tevatron, 1.96 TeV). For machine safety reasons it was decided to limit the maximum centre-of-mass energy to 7 TeV, and the first collisions at this world record energy took place on the 30 March 2010. From then on the number of proton bunches and the number of bunches per beam has been increasing day by day, reaching an instantaneous luminosity peak of 3.65 $\times$ 10^{33} cm^{-2} s^{-1} in the 2011. After the winter shutdown, on 5 April 2012 LHC starts the physics data taking of this year, recording the first collisions at a centre-of-mass energy of 8 TeV, new world record energy. This centre-of-mass energy increases the machine's discovery potential considerably making the 2012 still more interesting and exciting. The LHC is now scheduled to run until the end of 2012, when it will go into its first long shutdown in preparation for running at an energy of 6.5 TeV per beam ($\sqrt{s}$ = 13 TeV) as of late 2014, with the ultimate goal of ramping up to the full design centre-of-mass energy of 14 TeV.

3.2 The Physics at the LHC

The high energy and high luminosity of LHC offer a large and very ambitious range of physics opportunities like:

- the discovery of particles giving rise to the spontaneous electroweak symmetry breaking in the SM and so check the validity of the Higgs mechanism via the search of the Higgs boson in the whole mass range theoretically and experimentally allowed (from the LEP exclusion limit of 114.4 GeV [37] up to about 1 TeV);
- test of the validity of the SM, performing precision measurements on the known particles and interactions (such as W and top-quark masses and couplings, b-physics and CP violation), in order to observe possible deviations from the SM predictions;
- search for signatures beyond the Standard Model (new physics) such as:
  - the hypothetical supersymmetric particles;
  - new quarks or leptons;
  - eventual new physics at the electro-weak scale;

Figure 3.2: The CERN accelerator complex (top) and the basic layout of the LHC with the four main experiments (bottom).

- hypothetical new gauge bosons Z' and W';

- study of the properties of hadronic matter under extreme conditions, and possibly the transition to a state in which quarks and gluons are deconfined, the so called quark-gluon plasma. This will improve our knowledge of the behavior of matter at the dawn of time shortly after the Big Bang.

Obviously this is an open list...the nature often surprises the mankind and our imagination.

In order to pursue these objectives, it's necessary a very high luminosity, since the cross sections of the processes of interest are very low (as we can see in figure 3.1). But a high luminosity regime introduces many difficulties. One of them is the presence of pileup, that is the superposition of high cross section inelastic underlying collisions over the interesting physics interactions. At design luminosity 23 pileup events per bunch crossing are expected. Another difficulty due to the nature of proton-proton collisions is that QCD processes will dominate over the most important and studied processes. This imposes strong physics performance requirements on the LHC detectors, in particular on the general purpose detectors, ATLAS and CMS:

Trigger: the interaction rate of 40 MHz must be reduced to about 200 Hz recorded in order to allow a permanent storage and further analysis of the events. Therefore, a very selective and at the same time efficient trigger, providing a rejection of $\sim 10^7$, is needed. Moreover, excellent particle identification capabilities are needed already at the trigger stage, in order to extract efficiently the interesting physics signal while reducing the large QCD backgrounds down to acceptable rates.

Fast response, high granularity and resistance to radiations: the rate of events requires a fast and sophisticated electronics, able to discriminate events and minimize the effect of pileup. For very high particle fluxes it's necessary high granularity of the detector and significative resistance to high particle doses in order to assure the optimal operation of the detector and to prevent the fast aging of the detector components.

Full coverage: calorimetry should hermetically cover the full azimuthal angle (2π) and the pseudorapidity region $|\eta| < 5$ (see Section 3.3.1 for the definition of the ATLAS coordinate system). This is required mainly for a reliable measurement of the missing transverse energy (E_T^{miss}), the fundamental ingredient to obtain information about weakly interacting particles as neutrinos, LSPs (and so for my analysis), etc. A large calorimetric coverage is also needed to detect the forward jets produced in association with heavy Higgs boson.

Particle identification: the capability to precisely reconstruct, identify, separate and measure electrons, muons, photons, tau leptons and jets over

a wide range of energy is an essential requirement for every analysis of the LHC experiments.

Efficient vertex tagging: it's necessary to provide secondary vertex information essential for the reconstruction of B-hadron decay, for the tagging of b-jets, for the recognition of events containing the τ lepton and for the study of $t\bar{t}$ events.

3.3 The ATLAS detector

The ATLAS detector [38] is located at Point 1 of the LHC collider. It was completed in 2008 after five years of assembly works. ATLAS is a giant multi-purpose detector. The first its goal is the Higgs search, but it can cope with the study of a large variety of phenomena. Before briefly describing the main sub-systems, in the following subsection I introduce the ATLAS coordinate system and nomenclature.

3.3.1 Coordinate System

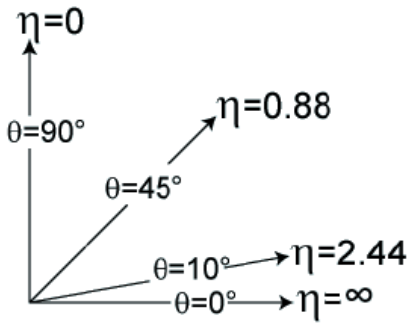

Figure 3.3: Pseudorapidity η as a function of the angle θ.

The nominal interaction point is defined as the origin of the coordinate system. The beam direction defines the z-axis and therefore the x-y plane is transverse to the beam direction (the plane where the transverse kinematic variables (like the transverse momentum p_T, the transverse energy E_T, and the missing transverse energy E_T^{miss}) lie). The x axis points towards the centre of the LHC ring and y points upward. The part of the detector with positive z is called side-A, while that with negative z is the side-C. The azimuthal angle ϕ is measured around the beam axis, and the polar angle θ is the angle from the beam axis. The pseudorapidity is defined as:

$$\eta = -ln[tan(\theta/2)] \tag{3.1}$$

and it is often used instead of the polar angle. The distance ΔR in the pseudorapidity-azimuthal angle $(\eta - \phi)$ space is defined as

$$\Delta R = \sqrt{\Delta\eta^2 + \Delta\phi^2} \tag{3.2}$$

3.3.2 Layout

The overall ATLAS detector layout [38, 39] is shown in Figure 3.4 and its main performance goals are listed in Table 3.1.

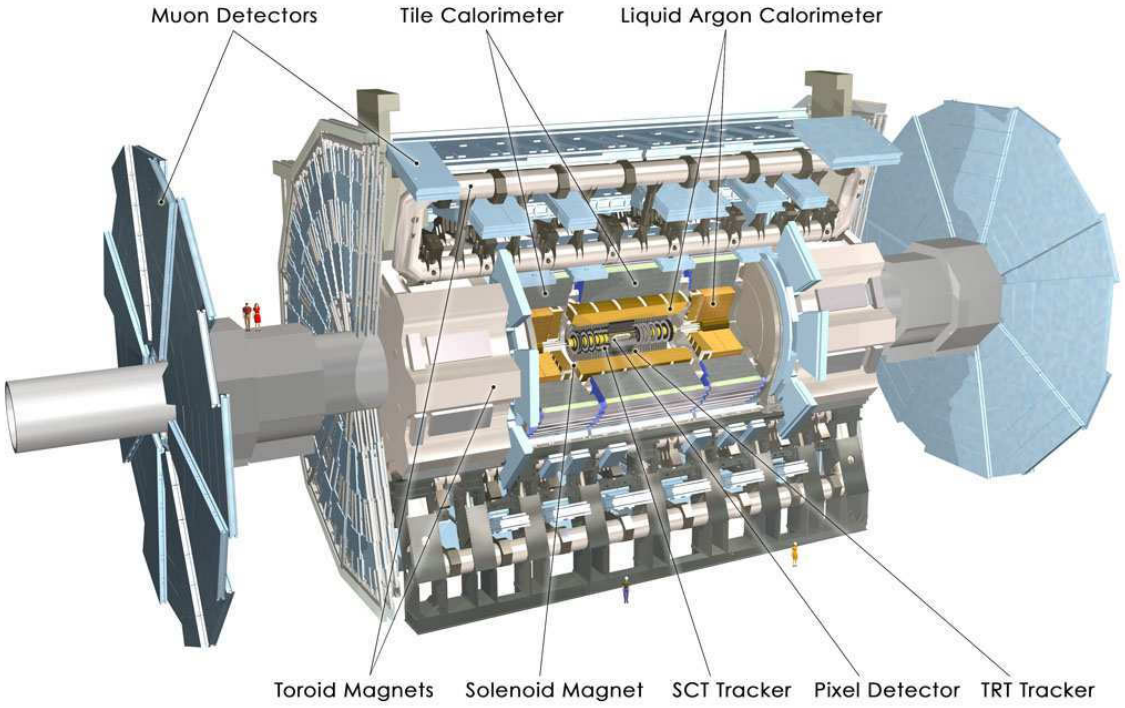

Figure 3.4: The ATLAS experiment.

Detector component	**Required resolution**	η **coverage**	**Trigger coverage**
Tracking	$\sigma_{pT}/p_T = 0.05\%\ p_T \oplus 1\%$	± 2.5	
EM calo	$\sigma_E/E = 10\%/\sqrt{E} \oplus 0.7\%$	± 3.2	± 2.5
HAD calo			
barrel, endcap	$\sigma_E/E = 50\%/\sqrt{E} \oplus 3\%$	± 3.2	± 3.2
forward	$\sigma_E/E = 100\%/\sqrt{E} \oplus 10\%$	$\lvert\eta\rvert \in [3.1, 4.9]$	$\lvert\eta\rvert \in [3.1, 4.9]$
Muon spectr	$\sigma_{pT}/p_T = 10\%$ at 1TeV	± 2.7	± 2.4

Table 3.1: General performance goals of the ATLAS detector. E and p_T are expressed in GeV.

The detector has a cylindric symmetry. The numbers of this detector are incredible: 25 m in height and 44 m in length, while the overall weight is approximately 7000 metric tons. Every ATLAS sub-detectors plays an important role in the reconstruction of particles. They are arranged in layers leading out from the interaction point. Starting from the beam pipe, we can find the tracking chamber, used to reconstruct the trajectory (track) of charged particles. It is enclosed by a solenoid magnet, which provides a magnetic field in the chamber that bends the charged particles. From the bending of the

tracks it's possible to measure the momentum and charge of particles[1]. The electromagnetic calorimeter, placed around the tracking chamber, is just designed to precisely measure the energy of electrons and photons. Outside the electromagnetic calorimeter there is the hadronic calorimeter, which measures the energy of hadronic particles. Finally, the calorimeters are enclosed by the muon spectrometer designed to reconstruct and identify muons. The spectrometer houses large toroidal magnets to deflect the path of muons. Combined with the tracking chambers it provides precise measurements of momentum and charge of the muons.

Before the description of the sub-detectors which form the ATLAS detector, I spend some words on a crucial aspect of each physics analysis: the detector acceptance. With this term, we quantify the spatial detector coverage: in fact, the acceptance is defined, for a given event-type or particle, as the efficiency to reconstruct that event-type due to the coverage of the detector. To maximize the acceptance, each sub-detector comprises a central cylindrical barrel region, closed off at each end by end-caps. As already underlined, the acceptance of the calorimeters is particularly important for an accurate measurement of E_T^{miss}, so their coverage is extended as close to the beam pipe in the forward and backward directions as possible.

3.4 The Inner Detector

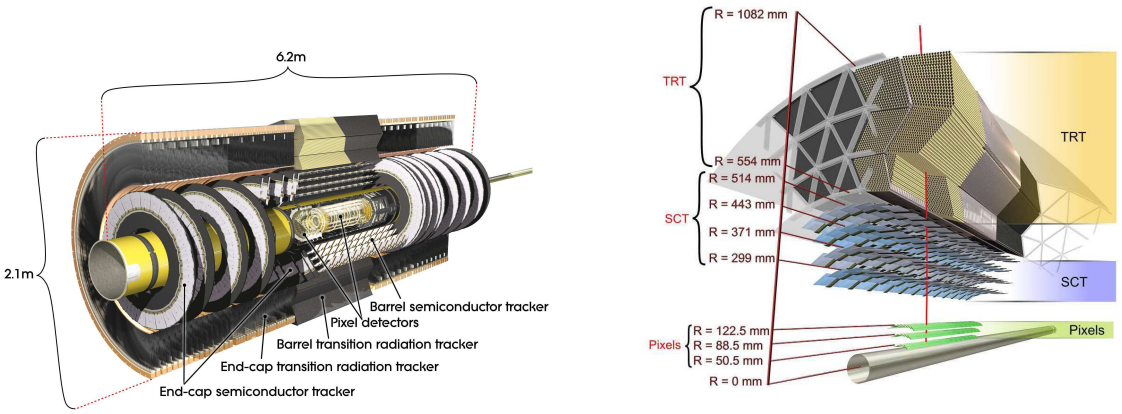

Figure 3.5: Three dimensional views of the ATLAS Inner Detector.

The ATLAS Inner Detector (ID) is designed to provide hermetic and robust pattern recognition, excellent momentum resolution and both primary and secondary vertex measurements for charged tracks above a given p_T threshold

[1]I remind the relation $p(\text{GeV}) = 0.3 \cdot B(\text{Tesla}) \cdot R(\text{m})$ where p is the momentum, B the magnetic field provided by the magnets and R the radius of curvature of the track.

(nominally 0.5 GeV); it provides a coverage in pseudorapidity up to $|\eta| < 2.5$.

The Inner Detector, whose three dimensional view is shown in Figure 3.5, is 7 m long, has a radius of 115 cm and is contained inside the superconducting solenoid magnet (2T). It is the sub-detector nearest to the beam pipe. It consists of three parts: the barrel region, covering the central pseudorapidity region ($|\eta| \leq 1$, ± 80 cm from the collision point), in which the sensors are arranged in concentric cylinders around the beam axis, and two end-cap regions, covering the gap $1 \leq |\eta| \leq 2.5$, with disks perpendicular to the beam axis.

Since the environment at nominal conditions is expected to have a very high track density, the granularity of the detector has to be very fine. This leads to the choice of the silicon semiconductor technology: pixel detectors close to the interaction region and silicon strips in the outer part. Due to the significant amount of material introduced by the silicon trackers and because of their cost, to obtain the large number of tracking points required for the pattern recognition, straw tube trackers are used at higher radii. This gives the possibility of continuous track following with much less material and a lower cost. These are the main features of the three detectors constituent the inner detector.

These three detectors are independent but complementary; the combination of the three techniques offers very robust pattern recognition and high precision in both ϕ and z coordinates. In fact, each track emerging from the interaction point crosses the beam pipe (1 mm of beryllium with a radius of 2.5 cm), at least three pixel layers, four double silicon strips planes (SCT, Semi-Conductor Tracker) and about 36 straw tubes of the Transition Radiation Tracker (TRT).

Pixel Detector

The system consists of three barrels at average radii 5, 9, 12 cm and five disks on each side between radii 12 and 19 cm along the beam line, in order to provide a complete angular coverage.
The pixel detector is designed to provide a very high granularity, high precision set of measurements as close to the interaction point as possible. The system provides three precision measurements over the full pseudorapidity range and determines the impact parameter resolution and the ability of the Inner Detector to find short lived particles such as B hadrons and τ leptons. In particular, the first detector layer, called B-layer, placed as close as possible to the beam line (about 4 cm from the interaction point), is crucial for the impact parameter measurements and vertexing.
The two dimensional segmentations of the sensors allow to have space points without any of the ambiguities associated with crossed strip geometry, but requires the use of advanced electronic techniques for the readout.

All pixel sensors are identical and have a minimum pixel size in $R - \phi \times z$ of 50×400 μm^2. The pixel layers are segmented in R -ϕ and z. The intrinsic accuracies are 10 μm ($R\phi$) and 115 μm (z for the barrel and R for the endcap disks). The pixel detector has approximately 80.4 million readout channels, necessary for the pattern recognition in the crowded environment of the LHC.

Semi-Conductor-Tracker (SCT)

Behind the pixel detector the SCT detector completes the high precision tracking, with eight precision position measures (hits) per track in the intermediate radial range, contributing to the measurement of momentum, impact parameter and vertex position, as well as providing good pattern recognition thanks to the high granularity.
It consists of four concentric barrel layers positioned between radii 30 and 52 cm and 9 disks on either side covering the required pseudorapidity range. The SCT is composed by two planes of silicon strip detectors. The innermost presents a relative rotation (stereo angle) of 40 mrad respect on the outermost, which lies with its long axis parallel to the beam pipe. They consist of two 6.4 cm long daisy-chained sensors with a strip pitch of 80 μm. In the end-cap region, the detectors have a set of trapezoidal strips running radially and a set of stereo strips at an angle of 40 mrad. The mean pitch of the strips is also approximately 80 μm. The intrinsic accuracies per module in the barrel are 17 μm ($R\phi$) and 580 μm (z), and in the disks are 17 μm ($R\phi$) and 580 μm (R). The total number of readout channels in the SCT is approximately 6.3 million.

Transition Radiation Tracker (TRT)

The TRT is the largest component of the ID, filling the majority of the ID cavity. It is composed by straw tube detector (drift chambers), interleaved with layers of polypropylene fibres and foils: a charged particle that passes through the boundary region between materials with a different refraction index emits X-ray radiation whose intensity is proportional to the relativistic Lorentz γ. The TRT works with two threshold levels, the ratio of the high threshold hits versus all the hits can be used to discriminate electrons and pions. To detect the transition photons the tubes are filled with a mixture containing Xenon. The straws are 65 μm thick Kapton tubes and have an internal diameter of only 4 mm to limit the occupancy. The detector consists of a central section which has a barrel geometry for $|\eta| \leq 0.8$ and two end-cap sections consisting of multi-plane wheels at higher $|\eta|$. The barrel region has a total of 73 layers of axial straw tubes (parallel to the beam axis) and extends from an inner radius of 56 cm to an outer radius of 107 cm.
The two end-caps have 18 wheels of radially oriented straw tubes, the first 14 nearest the interaction point cover a radius of 64 to 102 cm and the last four wheels extend down to a radius of 48 cm to provide coverage of the full

pseudorapidity range.
The total number of TRT readout channels is approximately 351000.
The TRT detector provides typically 36 measurements per track for nearly all pseudorapidity with spatial resolution of 170 μm. This contribute significantly to the momentum measurement, since the lower precision per point, compared to the silicon, is compensated by the large number of measurements and the higher average radius.

3.5 Calorimetry

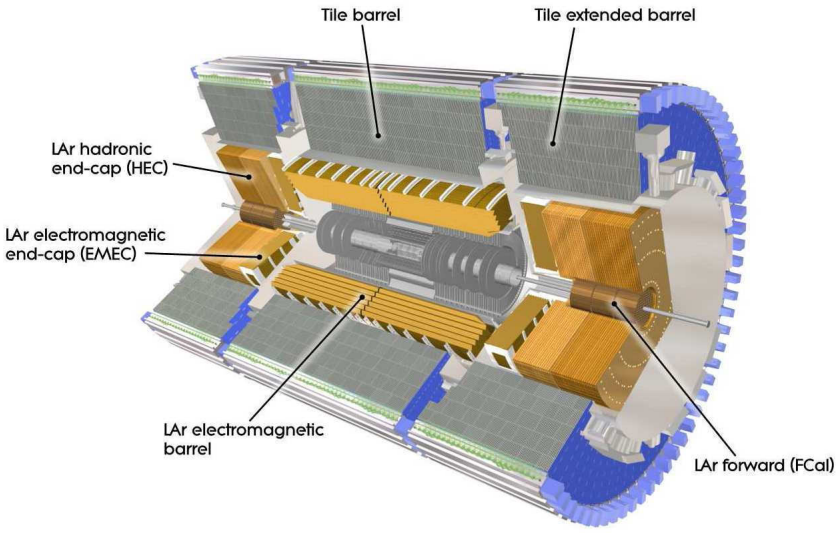

Figure 3.6: The calorimeter system.

ATLAS has two different types of calorimeter, like the most important general purpose detectors: a (LAr) electromagnetic calorimeter and an hadronic one. The purpose of these sub-detectors is to measure the energy of the particles and their direction from their energy deposits. In general, the ATLAS calorimeters consist of sampling detectors with full ϕ-symmetry and coverage around the beam axis. The calorimeters closest to the beam-line are located in three cryostats, one barrel and two end-caps. The barrel cryostat contains the electromagnetic barrel calorimeter and the solenoid magnet, whereas each of the two endcap cryostats contains an electromagnetic endcap calorimeter (EMEC), a hadronic end-cap calorimeter (HEC) (providing the angular coverage $1.5 < |\eta| < 3.2$) located behind the EMEC, and a forward calorimeter

(FCal) to cover the region closest to the beam ($3.1 < |\eta| < 4.9$). All these calorimeters use liquid argon (LAr) as active detector medium; liquid argon has been chosen for its intrinsic linear behaviour and good characteristics in terms of electronic noise, energy resolution, radiation resistance and stability of response over time.
In Figure 3.6 we can see an overview of the ATLAS calorimeter system.
These calorimeters cover the range $|\eta| <4.9$, using different techniques in order to satisfy the widely varying requirements of the physics processes of interest over this large $|\eta|$-range.
The total thickness of the EM calorimeter is greater than 22 radiation lengths (X_0) in the barrel and greater than 24 X_0 in the end-caps. The approximate 9.7 interaction lengths (λ) of active hadronic calorimeter in the barrel (10 λ in the end-caps) are adequate to provide good resolution for high-energy jets. Together with the large η-coverage, this thickness will also ensure a good E_T^{miss} measurement, which is important for many physics signatures and in particular for SUSY particle searches.

3.5.1 LAr Electromagnetic Calorimeter

The electromagnetic (EM) calorimeter is a LAr detector with accordion-shaped kapton electrodes and lead absorber plates over its full coverage. It is divided into two half barrels (covering the $|\eta| < 1.4$ region) and two end-caps ($1.4 < |\eta| < 3.2$) each subdivided into two coaxial wheels. The region between the barrel and end-cap EM calorimeters, $1.37 < |\eta| < 1.52$, is expected to have poorer performance because of the lack of instrumented material. It is often referred to as crack region. It is important to take into account this region to calculate a correct value of E_T^{miss}. To ensure maximum azimuthal coverage the EMCalo was designed with an accordion geometry (visible in figure 3.7): readout electrodes and lead absorbers are laid out radially and folded so that particles can not cross the calorimeter without being detected, providing very uniform performance in terms of linearity and resolution as a function of ϕ . The lead thickness in the absorber plates has been optimized as a function of η in terms of EM calorimeter performance in energy resolution. The electrodes work as transmission lines as well, so that no dead regions must be introduced.

Over the region devoted to precision physics ($|\eta| < 2.5$), the EM calorimeter is segmented into three longitudinal sections. For the end-cap inner wheel, the calorimeter is segmented in two longitudinal sections and has a coarser lateral granularity than for the rest of the acceptance.
In the region of $|\eta| < 1.8$, there is a presampler detector to correct for the energy lost by electrons and photons upstream in the tracker and in the calorimeter cryostat, that contains the solenoid coil. The presampler consists of an active LAr layer of thickness 1.1 cm (0.5 cm) in the barrel (end-cap) region.

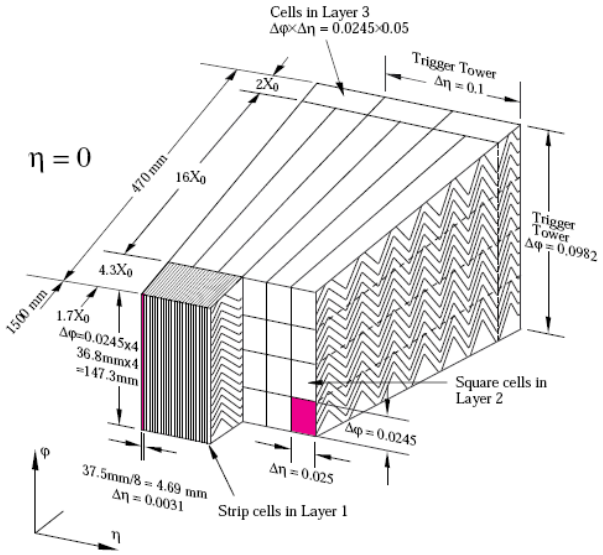

Figure 3.7: Design of a module of an accordion LAr calorimeter.

3.5.2 Hadronic Calorimeters

The Hadronic Calorimeter is realized with a variety of techniques depending on the region: central, end-cap and forward.

The tile calorimeter is placed directly outside the EM calorimeter envelope, in the central region. It is divided into a barrel that covers the region $|\eta| < 1.0$, and in two extended barrels covering the range $0.8 < |\eta| < 1.7$. It is a sampling calorimeter using steel as the absorber and scintillating tiles as the active material. The barrel and extended barrels are divided in the azimuthal direction into 64 modules (Fig. 3.8). There are three segmentations in depth, for a total depth of 9.7 interaction lengths λ at $\eta = 0$. The tiles are 3 mm thick and the total thickness of the steel plates in one period is 14 mm. Two sides of the scintillating tiles are read out by wavelength shifting fibres into two separate photomultiplier tubes. In η, the readout cells built by grouping fibres into the photomultipliers are pseudo-projective towards the interaction region. The resulting granularity is $|\Delta\eta \times \Delta\phi| \sim 0.1 \times 0.1$.

The hadronic end-cap calorimeter (HEC) is a copper/liquid-argon sampling calorimeter with a flat plate design, which covers the range $1.5 < |\eta| < 3.2$ and is housed in the same cryostat that contains the EM and forward calorimeter. The HEC is formed by two cylindrical wheels, with a radius of 203 cm, in each end-cap cryostat, each wheel containing two longitudinal sections. Each of the four HEC wheels is constructed by 32 identical wedge-shaped modules. The modules of the front wheels are made of 24 copper absorber plates interleaved with 8.5 mm LAr gaps, providing the active medium for this sampling calorimeter.

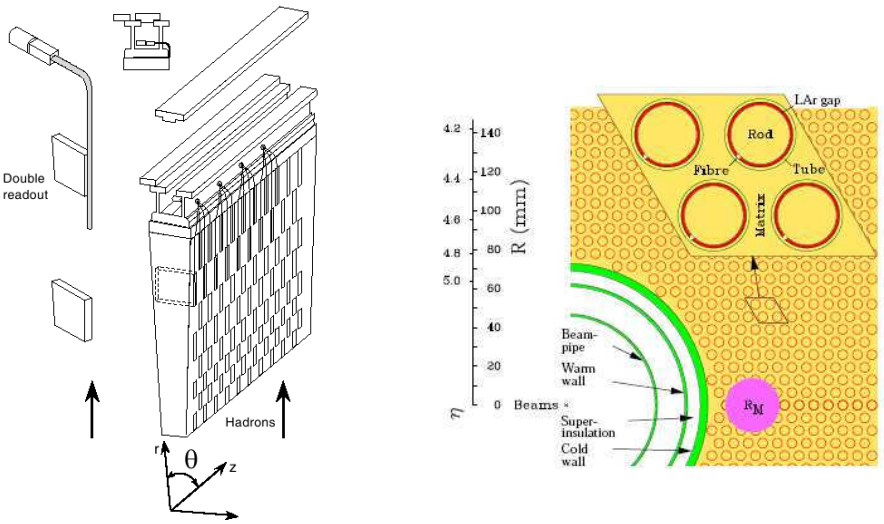

Figure 3.8: Design of a module of the tile calorimeter (left), and of FCal with the matrix of copper plates and the copper tubes and rods with the LAr gap for the electrodes (right).

The forward calorimeter (FCal) is a particularly challenging detector due to the high level of radiation it has to cope with. It is integrated into the end-cap cryostats, and provides coverage over $3.1 < |\eta| < 4.9$. The FCal is approximately 10 interaction lengths deep, and consists of three modules in each end-cap: the first, made of copper, is optimized for electromagnetic measurements, while the other two are of denser material (tungsten) in order to measure the energy of hadronic interactions. Due to the high radiation dose expected in this region, the electrode structure is different from the accordion geometry, consisting of a structure of concentric rods and tubes parallel to the beam axis. The LAr in the gap between the rod and the tube is the sensitive medium (Fig. 3.8). This geometry allows for excellent control of the gaps, which are as small as 0.25 mm in the first section, in order to avoid problems due to ion buildup.

3.6 Muon Spectrometer

The muon spectrometer (MS) forms the outer part of the ATLAS detector and is designed to detect charged particles (muons) exiting the barrel and end-cap calorimeters and to measure their momentum in the pseudorapidity range $|\eta| < 2.7$. It is also designed to trigger on these particles in the region $|\eta| < 2.4$. The designed performance goal is a stand-alone transverse momentum resolution of approximately 10% for 1 TeV tracks. Muon momenta from few GeV ($\sim$ 5-6 GeV) to $\sim$ 3 TeV may be measured by the spectrometer alone with an adequate momentum resolution and excellent charge identification.

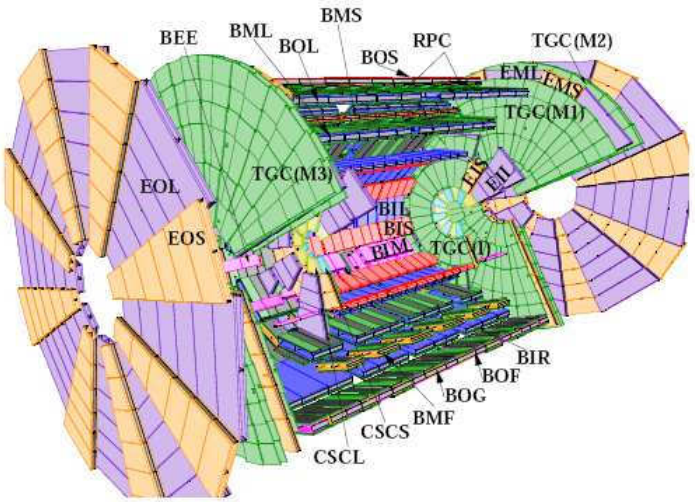

Figure 3.9: Schematic view of the ATLAS muon spectrometer with all the chamber typologies: the precision measurement tracking chambers (MDT and CSC) and the trigger chambers (RPC and TGC). In the end-cap, the first TGC layer (I) is located in front of the innermost tracking layer; the next three layers stand in front (M1) and behind (M2 and M3) the second MDT wheel. The first letter (B and E) of the MDT naming scheme refers to barrel and end-cap chambers, respectively. The second and third letters refer to layer (inner, middle, and outer) and sector (large and small) types, respectively.

The large volume magnetic field necessary to bend the particle trajectories arriving from the interaction region is provided by the large superconducting barrel toroid in the region $|\eta| < 1.4$, by two smaller end-cap magnets in the $1.6 < |\eta| < 2.7$ region and by a combination of the two in the transition region ($1.4 < |\eta| < 1.6$). The ϕ symmetry of the eight-coils forming the toroid is reflected in the symmetric structure of the muon chamber system, consisting of eight octants.
Barrel chambers are of rectangular shape and arranged cylindrically around the beam pipe; endcap chambers are trapezoidal and arranged in planes orthogonal to the beam pipe. The chambers in the barrel are arranged in three concentric cylindrical shells around the beam axis at radii of approximately 5 m, 7.5 m and 10 m, called respectively BI (Barrel Inner), BM (Barrel Medium) and BO (Barrel Outer). The endcap chambers are arranged in four disks on each side of the interaction point perpendicular to the beam axis, called EI (Endcap Inner), EE (Endcap Extra), EM (Endcap Middle), and EO (Endcap Outer), located at distances of $|z| \sim 7.4$ m, 10.8 m, 14 m, and 21.5 m from the interaction point. An auxiliary set of chambers, called BEE (Barrel End-cap Extra), are installed on the cryostats of the end-cap toroids.
The general layout of the muon system is shown in Figure 3.9.

The chamber technologies employed in the ATLAS muon spectrometer are four:

Monitored Drift Tube chambers (MDT): they perform the precision momentum measurement and cover the pseudorapidity range $|\eta| < 2.7$ (except in the inner most endcap layer where their coverage is limited to $|\eta| < 2.0$).

Cathode-Strip Chambers (CSC): they are located in the forward region ($2 < |\eta| < 2.7$). They are characterized by higher rate capability and time resolution, essential to operate in the innermost tracking layer.

Resistive Plate Chambers (RPC): they are located in the barrel region ($|\eta| < 1.05$), set in three layers. They compose a system of fast trigger chambers providing track information within a few tens of nanoseconds after the passage of the muon.

Thin Gap Chambers (TGC): these chambers, set in four layers, complete the trigger on muon tracks in the end-cap region ($1.05 < |\eta| < 2.4$).

The purpose of the precision-tracking chambers is to determine the coordinate of the track in the bending plane. However, the trigger chamber coordinate can be used to provide a "second-coordinate" measurement of track coordinates orthogonal (so in the non-bending plane) to the measurement given by the MDTs and CSCs. To achieve an high sagitta resolution, the locations of MDT wires and CSC strips along a muon trajectory must be known to better than 30 μm. To this effect, a high-precision optical alignment system monitors the positions and internal deformations of the MDT chambers; it is complemented by track-based alignment algorithms.

3.7 Magnetic System

The magnet system in ATLAS is complex. It weighs 13000 tonnes and operates at a temperature of 4.8 K, storing 1600 MJ of energy when operational. It is formed by four large superconducting magnets: a solenoid and a toroid system (three toroids). The spatial arrangement of the coils of the magnets is shown in Figure 3.10.

The central solenoid is coaxial with the beam axis and provides a 2 T axial magnetic field for the inner detector. To achieve the desired calorimeter performance, it's necessary to reduce the material thickness in front of the calorimeter: that is one of the reasons to choose a magnet with a solenoid assembly with a thickness of just 45 mm (that is only ~ 0.66 radiation lengths). The inner and outer diameters of the solenoid are 2.46 m and 2.56 m and its axial length is 5.3 m.

The toroid system consists of three large air-core toroids: two end-cap toroids (giving a magnetic field of 1T) that are inserted at each side of the

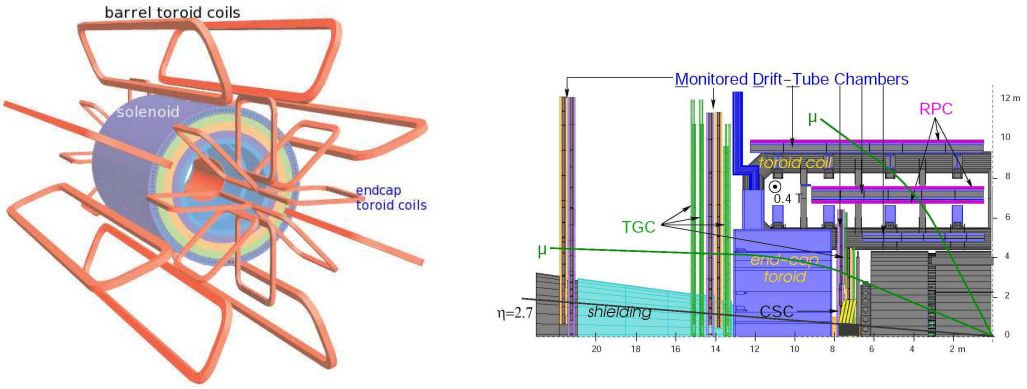

Figure 3.10: Left: geometry of the ATLAS magnetic system. Right: effects of the magnetic field on the trajectory of the muons passing trough the barrel and the endcap of the muon system.

barrel toroid (0.5 T) and line up with the central solenoid. Each of the three toroids consists of eight coils assembled radially and symmetrically around the beam axis. The barrel toroid coils are housed in eight individual cryostats. The overall size of the barrel toroid system as installed is 25.3 m in length, with inner and outer diameters of 9.4 m and 20.1 m respectively.
The magnetic field strength is roughly constant and cover the region $0 < |\eta| < 2.5$.

3.8 Forward Detectors

An essential task for the detector is to determine precisely the luminosity recorded by the experiment. Without a precise estimation of data integrated luminosity many experiments (especially those searching new physics) would be impossible. This goal is accomplished by a set of redundant measurements, taken by three very forward detectors: the LUCID (LUminosity measurement using Cerenkov Integrating Detector), ALFA (Absolute Luminosity for ATLAS) and ZDC (Zero-Degree Calorimeter).

LUCID is located at ± 17 m from the interaction point. It detects inelastic *p*-*p* scattering in the forward direction and is the main online relative-luminosity monitor for ATLAS.

The second detector ALFA lies at ± 240 m; it consists of scintillating fibre trackers.

The third system ZDC plays a key role in determining the centrality of heavy-ion collisions. It is located at ± 140 m from the interaction point. The ZDC modules consist of layers of alternating quartz rods and tungsten plates which can measure neutral particles at pseudorapidities $|\eta| > 8.2$.

In addition, the Minimum Bias Trigger Scintillators (MBTS), mounted in front of the electromagnetic end-caps, has been used as luminosity detectors

in early data analysis, beyond providing a minimum bias trigger signal.

3.9 Trigger and data acquisition (TDAQ)

The Trigger and Data Acquisition system (TDAQ) of the experiment is designed to select a manageable rate of interesting events for permanent storage and further analysis keeping the background rate low.
Given a target data flux of about 300 MB/s and an expected event size of $\sim$ 1.6 MB, the design output rate is $\sim$ 200 Hz. The request appears incredible. However, a three levels trigger architecture can satisfy the required five order of magnitude online event selection: a fast first level trigger (LVL1), implemented on custom hardware, is followed by two software based High Level Trigger systems (HLT): the second level trigger (LVL2) and the Event Filter (EF). The schema of the three levels TDAQ architecture is shown in Figure 3.11 [40].

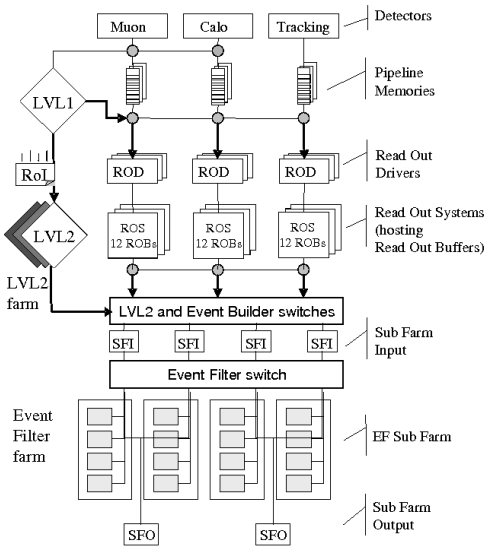

Figure 3.11: Overview of the ATLAS TDAQ system.

Each trigger level refines the decisions made at the previous level using more sophisticated algorithms and lower rates.
The LVL1 trigger searches for high transverse-momentum muons, electrons, photons, jets, and τ leptons decaying into hadrons, as well as large missing and total transverse energy. Its selection is based on information from a subset of detectors, as for example on timing from an electrostatic beam pick-up (BPTX), coarse detector information from muon trigger chambers and towers of calorimeter cells, together with multiplicity information from the MBTS and very forward detectors. The LVL1 selects events with a maximum rate of 75kHz and a latency of less than 2.5 μs (about 100 bunch crossings). During

this time, the front-end electronics of the various sub-detectors keep the complete event data in pipeline memory buffers: in fact, if the data for rejected events are discarded, the data for selected ones (up to 160 GB/s) are passed via the Readout Drivers (RODs) into 1600 Readout Buffers (ROBs). Event data remain there and are pulled by LVL2 and by the Event Builder (EB) nodes on demand.
In each event, the L1 trigger also defines one or more Regions-of-Interest (RoIs), i.e. the geographical coordinates in η and ϕ of those regions within the detector where its selection process has identified interesting features. The RoI data include information on the type of feature identified and the criteria passed.

For each event accepted by LVL1, a list of the Regions of Interest (RoIs) is given to LVL2, which provides a rejection factor of 70-100, bringing the rate to 1 kHz with an average latency of 40 ms. The L2 examines the RoIs using more detector information than L1, and working in parallel on more RoIs and subdetectors with more complete algorithms.

The final stage of the event selection is carried out by the event filter, which reduces the event rate to roughly 200 Hz. The EF then has access to the complete event and uses reconstruction algorithms similar to the ones used offline within an average event processing time of the order of four seconds. Better information on energy deposition improves the threshold cuts, while track reconstruction in the inner detector significantly enhances the particle identification.
Events selected by the EF are then moved to permanent event storage at CERN computer centre. Since we want to have a final event rate not greater than 200 Hz not all the available trigger chains are allowed to make a decision (some of them have a too high output rate when the luminosity is high). When this happens the trigger chain is prescaled: only a certain fraction of the events that fire the trigger is actually recorded.

3.10 The ATLAS analysis software

The ATLAS software framework, Athena [41], provides a computer simulation of the ATLAS detector. It is able to simulate the response of the detector to different proton-proton collisions. The Athena software framework is of fundamental importance for many physics analysis and performance studies: in fact, with event generators like MC@NLO [42], HERWIG [43] and PYTHIA [44], it allows to simulate Monte Carlo events. These Monte Carlo events are useful both in the absence of real data, providing a way of dreaming up new physics analyses and quantifying expected detector performance, and in the presence of data, when the Monte Carlo provides an irreplaceable tool for comparisons between expectations and observations (for example, in my SUSY analysis they are essential to test the Standard Model and reveal eventual deviations). Conventional python scripts (called jobOptions) are used to control an Athena

application configuration at run-time. The complexity of the physics events that are analyzed at the LHC and the diversity of the detectors that constitute the ATLAS experiment demand for a detailed description of the event generation and simulation of the detector response. The ATLAS simulation program is a multi-stage process:

1 - Event generation: the production of particle four vectors from specified physics processes in order to reproduce the final state of a p-p collision.

2 - Simulation: the events generated in the previous step are passed through a GEANT4 [45] simulation of the ATLAS detector to produce GEANT4 hits. GEANT4 simulates the interaction of the particles with the detector and infrastructure components, recording their tracks, the energy deposited in the various part of the detector, as if the particles were real in a real detector. So, in the simulation it takes into account the correct and precise geometry of ATLAS.

3 - Digitization: the process whereby the GEANT4 hits from the simulation are re-processed in order to simulate the detector output in a form similar to the one which might be expected from readout electronics in the actual experiment. This produces "digits", such as times and voltages, as would be produced by a real particle in the real detector.

4 - Reconstruction: the process whereby the raw data digits from the previous step of digitization are reconstructed into tracks and energy deposits. Here, as happens in a real detector, the software takes the voltages, times and other signals from the hardware in the detector and deduces the physics of the detected collisions and processes.

To simulate pile-up, hits from various types of event (signal, minimum bias, cavern background, beam gas and beam halo) must be overlapped.

Programs like Atlfast [46] and AcerDET [47] skip this "full" analysis chain described above: they take the generated events (from the first step) and apply resolution functions based on appropriate parameterizations to the particles in order to simulate the effect and the reconstruction done by the detector (arriving directly at the fourth step).

3.11 ATLAS reconstruction

In this section I describe the the ATLAS reconstruction of the physics objects interesting for my SUSY analysis, presented in the following chapter: electrons, muons and jets. After these, I can introduce the missing transverse energy E_T^{miss}.

3.11.1 Track reconstruction

The reconstruction algorithms of many physics objects, in particular of electrons and muons, are based on the tracking, the reconstruction of tracks. In fact, from track properties, such as TRT hits and the impact parameter, we can retrieve useful identification and physics information, as the lifetime of the particle that produced the track.

The ATLAS tracking algorithms follow an inside-out sequence aiming to collect hits in the inner detector and to fit them to find the track. So they start from seed finding in the silicon layers of the inner detector. The seeds are then used to build roads, within which hits may be found while moving towards the outer edge of the silicon detector. Finally, the search is extended to the TRT and then the collection of hits is fit to obtain the final track parameters. A particle passing through the barrel region of the TRT crosses about 36 TRT tubes on its way out.

An important characteristic of the tracking system is the capability or reconstruct both primary and secondary vertices. The track resolution along the z coordinate is about 100 μm in the pixels and the resolution on the position of the primary vertex is comparable. This very good resolution is fundamental for the impact parameter measurements and is also essential in the presence of pileup to distinguish objects associated with the primary interaction from superimposed activity. In fact, the reconstruction of the primary vertex allows to discriminate tracks that come from other interactions in the $\sim$ 5 cm long interaction region. The vertex position resolutions in x and z improve with the increasing of the numbers of tracks.

3.11.2 Electrons

The ATLAS electromagnetic (EM) calorimeter (see section 3.5.1) is designed to be able to identify efficiently electrons (and photons) within a large energy range (5 GeV - 5 TeV) and to measure their energies with a linearity better than 0.5% [49].

For the identification and reconstruction of electromagnetic clusters a sliding window algorithm [50] is used. Rectangular clusters are formed with a fixed size, in such a way that their position corresponds to the maximum amount of energy deposited inside them (the minimum threshold of energy is 3 GeV). The cluster size depends on the particle type being reconstructed and on the calorimeter region. For example, the electrons need large clusters due to their high interaction probability in the upstream material and also due to the fact that they bend in the magnetic field, radiating soft photons. Several series of these kinds of clusters are then built by the reconstruction software, corresponding to different sliding window sizes. These clusters are the starting point of the calibration and selection of electron candidates.

For each of the reconstructed clusters, the reconstruction tries to find a matching track within a $\Delta\eta \times \Delta\phi$ range of 0.05×0.10 with momentum p

compatible with the cluster energy E ($E/p < 10$). If one track is found, the reconstruction checks for the presence of an associated conversion. An electron candidate is created if a matching track is found while no conversion is flagged. These electron candidates are the starting point of a more refined identification based on shower shapes and on respective cuts.

Three levels of quality of the electron identification criteria are defined:

Loose cuts: they perform a simple electron identification based only on limited information from the calorimeters. Objects of the cuts are the hadronic leakage and the shower-shape variables, derived from the middle layer of the EM calorimeter only. The loose cuts provide excellent identification efficiency, but poor background rejection.

Medium cuts: this set of cuts improves the background rejection quality, exploiting cuts on the energy deposits in strips in the first layer of the EM calorimeter and on the tracking variables. The tracking variables considered in the cuts include the number of hits in the pixels, the number of silicon hits (pixels plus SCT) and the transverse impact parameter. The medium cuts increase the jet rejection by a factor of 3.4 with respect to the loose cuts. Moreover the strip-based cuts allows to separate electrons from pions. However, we have a reduction of $\sim 10\%$ of the identification efficiency.

Tight cuts: this set of cuts makes use of all the particle identification tools available for electrons. So, in addition to the cuts defining the medium electron quality, cuts are applied on the number of vertexing layer hits (to reject electrons from conversions), on the number of hits in the TRT, on the ratio of high-threshold hits to the number of hits in the TRT (to reject the dominant background from charged hadrons) and on the difference between the cluster and the extrapolated track positions in η and ϕ. This set of cuts tight presents two different final selections named tight (isol) and tight (TRT); they are optimised differently for isolated and non-isolated electrons. In the case of tight (isol) cuts, an additional energy isolation cut is applied to the cluster, using all cell energies within a cone of $\Delta R < 0.2$ around the electron candidate. This set of cuts is characterized by the highest isolated electron identification efficiency and the highest rejection against jets. Instead, the tight (TRT) cuts do not include the additional explicit energy isolation cut, but in order to further remove the background from charged hadrons they present tighter cuts on the TRT information.

Signal Monte Carlo based methods are used for the calibration of the electrons. They correct for the energy deposited in the material in front of the calorimeter, calibrate the cluster energy deposited in the calorimeter and correct for leakage outside the cluster (lateral leakage) and beyond the calorimeter (longitudinal leakage).

3.11.3 Muons

The muon signature is very clean and so many physics processes at the LHC are accessible only through the detection of highly energetic muons, because of the overwhelming QCD background. The reconstruction of muons is based on information from the Muon Spectrometer, Inner Detector and calorimeters. There are different kinds of muon candidates, depending on the use of the detector information in reconstruction:

Stand-alone muons are reconstructed combining the hits of the muon spectrometer into segments to form a track. In order to obtain the muon momentum at the interaction point we must correct the muon momentum measured using this track for the (parameterized) energy loss of the muon in the calorimeter. The track is extrapolated back to the beam axis to obtain the η and ϕ coordinates of the muon and the impact parameter with respect to the interaction point. The name "stand-alone" is due to the fact that only the hits of the muon system are used for the reconstruction.

Combined muons are built combining the stand-alone muons with an inner detector track. The muon trajectory in the inner detector provides also information regarding the direction of flight and impact parameter.

Segment tagged muons are reconstructed starting from the inner detector. The reconstruction algorithms use as a seed an inner detector track and then search for track segments in the precision muon chambers that can be associated to the inner detector track.

Calorimeter tagged muons are built, as the segment tagged muons, starting from an inner detector track. This track is identified as a muon if it's possible to associate energy depositions compatible with the minimum ionizing particle hypothesis to it.

These different algorithms of muon reconstruction provide a useful redundancy. However, to avoid overlaps at reconstruction level just one muon is flagged as BestMatch when a stand-alone muon matches more than one inner detector track. Overlaps between the tagged and combined muons are removed by combining candidates that share the same inner detector track.

To evaluate the muon performance in detail ATLAS uses two different chains: STACO [51] and MuId [52]. These chains correspond to different sets of algorithms that build the classes of candidates listed above. Both muon combination algorithms create combined tracks out of pairs of muon-only and inner-detector-only tracks. To do this, a match χ^2 is used and corrections are made for energy loss in the calorimeter. STACO does a statistical combination of the track vectors to obtain the combined track vector, while MuId re-fits the combined track, starting from the ID track and then adding Muon measurements.

3.11.4 Jets

Hadronic particles in ATLAS deposit their energy mainly in the calorimeter system. The ATLAS calorimeters have a high granularity (about 187000 cells independently read-out) and a high particle stopping power over the whole detector acceptance ($|\eta| < 4.9$). These and other calorimeter features (see section 3.5) allow a high quality jet reconstruction also in the challenging environment of the proton-proton collisions of LHC.

The jet reconstruction techniques and algorithms exploit the many information content in the cells: energy, time, quality and gain. The cells are primarily set at the so-called electromagnetic scale (EM)[2], as it has been determined by electron test beams and simulations. ATLAS calorimeters are not compensating[3] so EM showers generate larger signal than hadrons depositing the same energy, therefore a specific correction for hadronic signals is needed. However it is very difficult to use individual cell signals; in fact, they can be negative due to noise effects and it is challenging to determine the source of the signal without signals from neighbours. So, for the jet reconstruction are used collection of cells, such as towers or topological clusters. In case of the towers, the cells are projected onto a fixed grid in pseudorapidity (η) and azimuthal angle (ϕ). The tower bin size is $\Delta\eta \times \Delta\phi = 0.1 \times 0.1$ in the whole acceptance region of the calorimeters ($|\eta| < 4.9$ and total coverage in ϕ) with $100 \times 64 = 6400$ towers in total. The signal contribution of the projective calorimeter cells to a tower signal is proportional to the overlap fraction of the cell area with the tower. Thus, the tower signal is the sum of possibly weighted cell signals (all cells are included). The resulting tower signal is on the electromagnetic energy scale, as the cell signals. No further corrections or calibrations are applied at this stage.
The alternative representation of the calorimeter signals for jet reconstruction are topological cell clusters, which are basically an attempt to reconstruct three-dimensional energy deposits representing the showers developing for each particle entering the calorimeter. The clustering starts with seed cells having a signal-to-noise ratio above a certain threshold (4). All directly neighbouring cells of these seed cells, in all three dimensions, are collected into the cluster. Neighbours of these added cells are considered only if they have a signal-to-noise ratio above a certain secondary lower threshold (2). Finally, a ring of guard cells with a positive signal significance (threshold 0) is added to the cluster. Figure 3.12 shows a simulated QCD event with 4 jets in the final state: we can see the event at particle level and in the ATLAS calorimeters. The difference between towers or clusters jets is shown; a given calorimeter signal definition like clusters may reproduce the jet shape at particle level better in certain regions of the calorimeters than in others. For example, from the de-

[2]The electromagnetic scale (EM) corresponds to the energy deposited in the calorimeter calculated under the assumption that all processes are purely electromagnetic in nature.

[3]An hadronic calorimeter is not compensating if its response e to the electromagnetic component is different from the response h to the hadronic component. So $e/h \neq 1$.

picted event in this figure the cluster signals represent the transverse energy flow of particles inside a jet better than the tower jets in the central and endcap regions, while in the forward region the clusters cannot resolve individual showers anymore and thus cannot reproduce the jet shape very well; in these regions a better representation os jet structure is provided by the the tower jets. Furthermore, the noise suppression for the cluster jets leads to consider fewer cells than for the tower jets.

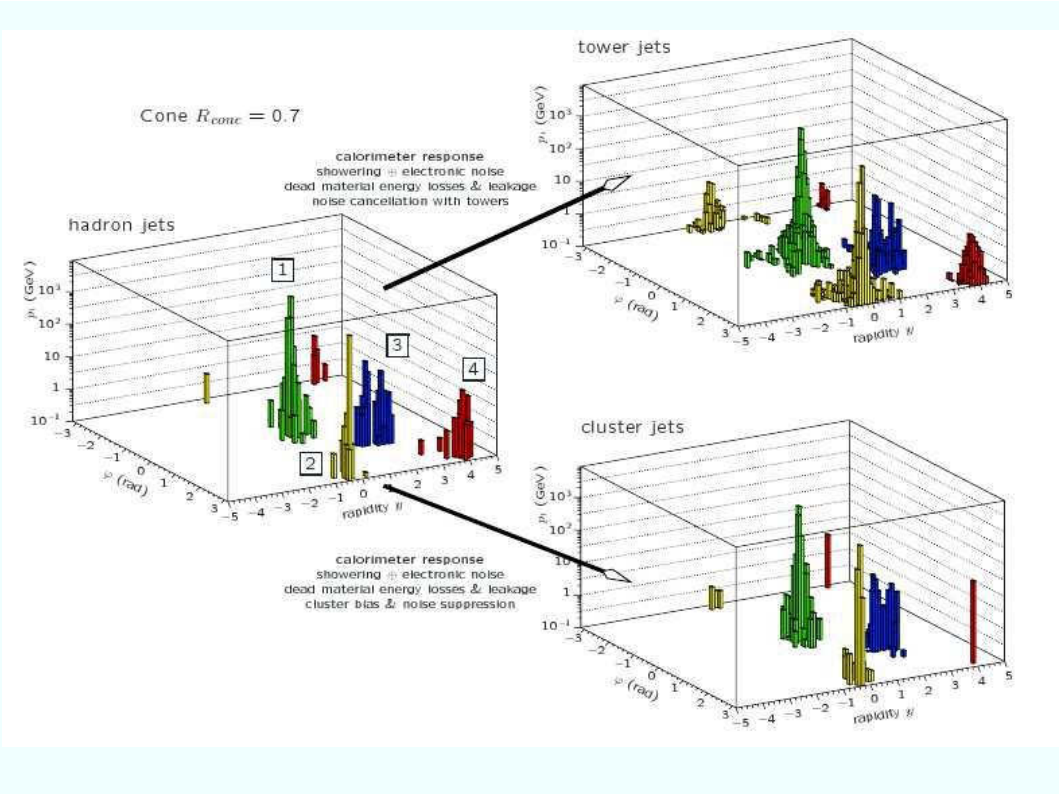

Figure 3.12: A simulated QCD event with four jets in the final state, as seen at particle level and in the ATLAS calorimeters when using towers or clusters [39].

The main common feature of all jet finder implementations in ATLAS is the full four-momentum recombination whenever the constituents of a jet change, either through adding a new constituent, or by removing one, or by changing the kinematic contribution of a given constituent to the jet. Also, in the ATLAS reconstruction software framework ATHENA, the same jet finder code can be run on objects like calorimeter signal towers, topological cell clusters in the calorimeters, reconstructed tracks, and generated particles and partons.

Many algorithms have been used or proposed for defining jets. In this section I briefly describe that used for defining the jets considered in my SUSY analysis: the recursive recombination cluster algorithms [53].
The Cluster Algorithms are based on pair wise clustering of the initial constituents. In general, the algorithms define a distance between objects and

some conditions upon which clustering should be terminated. Two distances d are introduced: d_{ij} between objects (particles, pseudojets) i and j and d_{iB} between object i and the beam (B). The (inclusive) clustering proceeds by identifying the smallest of the two distances; if it is d_{ij} then recombines objects i and j, while if it is d_{iB} then calls the object i jet and remove it from the list of objects. The distances are recalculated and the procedure repeated in a recursive way until no objects are left. The quantities, d_{ij} and d_{iB} are evaluated as follows:

$$d_{ij} = min(k_{Ti}^{2p}, k_{Tj}^{2p}) \frac{\Delta_{ij}^2}{R^2} \tag{3.3}$$

$$d_{iB} = k_{Ti}^{2p} \tag{3.4}$$

where

$$(\Delta)_{ij}^2 = (y_i - y_j)^2 + (\phi_i - \phi_j)^2 \tag{3.5}$$

and k_{Ti} , y_i and ϕ_i are respectively the transverse momentum, rapidity and azimuthal angle of particle i. R is the usual radius parameter while p is the parameter that governs the dependence of the energy on the geometrical (Δ_{ij}) scales. For large values of R, the equation 3.3 shows that the distance d_{ij} becomes small, and thus more merging takes place before jets are complete. Defined these distances, now I introduce one of the cluster algorithms, used in my analysis and in general in ATLAS: the Anti - k_T . For the Anti - k_T algorithm [54], $p = -1$ in Equation 3.4. This means that in the vicinity $\Delta R < R$ of a hard object, all softer objects will be merged with the harder object in order of their closeness in ΔR. Thus the jet boundary is unaffected by soft radiation. If two comparably hard objects are within $R < \Delta R < 2R$ of each other, energy will be assigned to one of them depending upon their relative k_T and distance. The ordering of the merging is not meaningful for this algorithm, so if we have an hard objects within $\Delta R < R$ of each other, a single jet will be formed containing both hard objects and the soft objects within their vicinity in a similar way as in the first case proposed. In ATLAS Anti-k_T has been adopted as default with $R = 0.4$ or $R = 0.6$. In the SUSY analyses (and so in my analysis), the chosen value of R is 0.4.

3.12 Missing transverse energy

The missing transverse energy (E_T^{miss}) in ATLAS is primarily reconstructed from energy deposits in the calorimeters and reconstructed muon tracks. We have many sources of energy deposits and muon tracks: in addition to the hard scattering process of interest, we must considerer the underlying events, multiple interactions, pileup and coherent electronics noise, particles not coming from the LHC collisions. For a correct determination of E_T^{miss}, it's necessary classify the energy deposits into various types (e.g. electrons or jets) and calibrating them accordingly. In fact the ATLAS calorimeters are not compensating and so the response to a electron is different from that to a jet.

Another source of E_T^{miss} is the presence of dead regions where the energy loss is not revealed.

The E_T^{miss} reconstruction algorithm starts from the energy deposits in calorimeter cells that survive a noise suppression procedure (with a method similar to that described in the previous section for the cells and topological clusters necessary for the jet reconstruction). In a first time, the cells can be calibrated using global calibration weights depending on their energy density (guaranteeing a certain robustness because it does not rely on other reconstructed objects). In a subsequent step, the method can be refined and the cells can be calibrated according to the reconstructed object they are assigned to. Corrections are applied for the muon energy and for the energy lost in the cryostat.

Therefore, we can express what observed before with the following definition of the missing transverse energy:

$$E_T^{miss} = \sqrt{(E_x^{miss})^2 + (E_y^{miss})^2} \tag{3.6}$$

where E_T^{miss} components include contributions from transverse energy deposits in the calorimeters (Calo), corrections for energy loss in the cryostat (Cryo) and measured muons (Muon):

$$E_{x,y}^{miss} = E_{x,y}^{miss,Calo} + E_{x,y}^{miss,Cryo} + E_{x,y}^{miss,Muon} \tag{3.7}$$

The first contribution, the Calo term, is calculated in the following way:

$$E_x^{miss,Calo} = -\sum_{i=1}^{Ncell} E_i \sin\theta_i \cos\phi_i \quad E_y^{miss,Calo} = -\sum_{i=1}^{Ncell} E_i \sin\theta_i \sin\phi_i \tag{3.8}$$

where E_i, θ_i and ϕ_i are the cell energy, polar angle and azimuthal angle respectively. Because of the high granularity of the calorimeter (about 187000 cells), it is essential to suppress noise contributions to E_T^{miss} that could compromise the measure. A way to do this is the reduction of the number of cells $Ncell$ in the sum, using only cells belonging to topological clusters (see Section 3.11.4). In the topoclusters building procedure, only cells with a signal to noise ratio above a threshold are considered, while only noise cells and cells flagged as very noisy in the ATLAS database, which represent about 0.1% of the total cells in the calorimeter, are removed.

The muon contribution to E_T^{miss} is calculated from the momenta of muons measured in a range of pseudorapidity $|\eta|$ <2.7:

$$E_{x(y)}^{miss,Muon} = -\sum_{selmuons} E_{x(y)}^{muon} \tag{3.9}$$

In the region $|\eta| < 2.5$ only good-quality muons in the muon spectrometer with a matched track in the inner detector are considered. The muon contribution is calculated in a different way for isolated and non-isolated

muons, where with non-isolated are labeled those muons within the distance $R = \sqrt{(\Delta\eta)^2 + (\Delta\phi)^2} < 0.3$ from a jet in the event. The p_T of an isolated muon is determined from the combined measurement of the inner detector and muon spectrometer. In this case the energy lost by the muon in the calorimeters ($E_{x,y}^{miss,Calo,Muon}$) is not added to the calorimeter term. Instead, for a non-isolated muon, the energy lost in the calorimeter can not be separated from the nearby jet energy. The muon spectrometer measurement of the muon momenta after energy loss in the calorimeter is therefore used unless there is a significant mis-match between the spectrometer and the combined measurement. In this case the combined measurement minus the parameterized energy loss in the calorimeter is used. For higher values of the pseudorapidity outside the fiducial volume of the inner detector ($2.5 < |\eta| < 2.7$), there is no matched track requirement and the muon spectrometer is used alone.

Chapter 4

The flavour subtraction analysis

The typical signature predicted by the supersymmetry theories is characterized by high transverse missing energy E_T^{miss} because of the presence of new hypothetical supersymmetric neutral particles, the neutralinos, that escape from the detector without being detected. Moreover, at LHC we would have high squark and gluino production cross-sections; their decays would produce energetic jets. So, the main clues of a supersymmetry event are high E_T^{miss} and very energetic jets. However, slepton, gaugino or electroweak gauge boson decays can also contain leptons. In my work, I seek supersymmetry in events containing exactly two leptons. The preference for this signature respect on the zero lepton and the one lepton ones is due to the better knowledge and estimation of the Standard Model backgrounds we have in the two lepton channel. In fact, the request of two leptons suppresses some background difficult to model and predict (such as the QCD processes). However, on the other side, this analysis has a discovery potential lower than the other channels and so it's necessary a higher statistic; with the increasing of the luminosity and of the collected statistic this problem will become less important.

In this Chapter, I present a complete analysis searching for evidence of supersymmetry signal in events with exactly two leptons (e or μ with opposite charge) and high transverse missing energy E_T^{miss}. I perform the analysis on data collected until the summer 2011 (for a integrated luminosity of $\sim$ 1 fb^{-1}) by the ATLAS detector at an energy in the centre of mass $\sqrt{s}$ of 7 TeV. In my analysis, called "flavour subtraction", I look for decay chains in supersymmetric events which can only produce lepton-pairs with identical flavour leptons: for example, events containing the decay chains $\tilde{\chi}_2^0 \to \tilde{\ell}^{\mp}\ell^{\pm} \to \tilde{\chi}_1^0\ell^{\mp}\ell^{\pm}$ or $\tilde{\chi}_2^0 \to \tilde{\chi}_1^0\ell^{\mp}\ell^{\pm}$. If these supersymmetric events realize in nature, they would be responsible for an excess of identical flavour leptons (e or μ) leptons over pairs with different flavour leptons beyond the Standard Model prediction. From the measurement of this excess, we hope to find the evidence (or a hint) of the existence of Supersymmetry and to make mass measurements (exploiting the end points of invariant mass distributions) or, in the worst of cases, we could set limits on the sparticle masses. Events in which the two leptons are produced by independent sparticle decays are canceled as a result of the subtraction procedure.

In this analysis, the backgrounds characterized by equal branching ratios for the production of lepton-pairs of identical and different flavour are removed, canceled by subtracting the number of observed different flavour lepton-pairs from the number of observed identical flavour lepton-pairs. It is a very important feature of this analysis because the dominant Standard Model backgrounds to a two-lepton search in events with high missing transverse energy are generally ones for which the branching ratios for decays to identical flavour lepton-pairs equal the branching ratios for decays to different flavour lepton-pairs. The most notable is $t\bar{t}$ production: it dominates two-lepton searches and its estimation using data-driven techniques is generally made difficult by the need to kinematically reconstruct the $t\bar{t}$ events to obtain a relatively clean control region. Therefore, in the flavour subtraction analysis remain only the flavour asymmetric backgrounds, which produce identical flavour lepton-pairs and rarely different flavour lepton-pairs: Z/γ^*+jets events and W Z pair production events. The latter has a low cross-section, whilst the former is suppressed by the cut on missing transverse energy (but it remains the most challenging Standard Model background).

A second point that makes this analysis so interesting and promising is the small systematics uncertainties related with the excess of identical flavour lepton-pair. In fact, many of the uncertainties in the different flavour event rates are shared by the identical flavour event rates thus canceling in large measure through the subtraction procedure.

This chapter, after the presentation of the event samples analyzed (section 4.1) and of the ingredients of the physics analysis (leptons, jets and E_T^{miss} in section 4.2), I will describe the recipe for performing the two lepton analysis. Then in the second half of the chapter, I will introduce the subtraction technique used to quantify the identical flavour excess in data. For the correct interpretation of this excess in terms of new physics, it is essential to understand (and so estimate) the contribution to the measured identical flavour excess from the Standard Model processes: therefore I will describe the partially data-driven techniques used to predict this distribution (section 4.7). At the conclusion of the work, the comparison between the observed and the expected identical flavour excess allows to set a limit in this excess, based on a statistical technique employing toy Monte Carlo experiments.

4.1 Event Samples

4.1.1 Data

The datasets analyzed in my work correspond to the data collected until the summer 2011 at $\sqrt{s} = 7$ TeV during stable periods of pp collisions with nominal magnetic field conditions. The considered runs are those from 178044 to 184169 (data-taking periods B-G). For each run only those luminosity blocks satisfying data quality criteria for inner detector, calorimeters and jet and

missing transverse energy reconstruction were analyzed. After these selections, the total integrated luminosity is 1035.18 pb^{-1} for the Egamma stream and 1035.04 pb^{-1} for the Muon stream.

4.1.2 Monte Carlo samples

All the Monte Carlo samples considered for the analysis were produced by the ATLAS central production teams. In appendix the complete list of the MC samples used with the appropriate cross sections are given. Top quark pair-production and single top-quark production was simulated with MC@NLO [42], using the CTEQ66 next-to-leading (NLO) parton distribution functions [55]. Samples of W+jets and Z+jets events (including as decay products one and two lepton respectively) were both generated using the ALPGEN [56] generator with the CTEQ6L1 parton distribution functions [57]. HERWIG [43] was used to generate the diboson samples (WW, WZ and ZZ). Fragmentation and hadronization for the ALPGEN and MC@NLO samples was performed with HERWIG, using Jimmy [58] for the underlying event model. All Monte Carlo samples take into account the effect of the interaction with the ATLAS detector passing through a full GEANT4 [45] simulation of the ATLAS detector. The approach employed to consider the presence of multiple interactions per crossing is described in detail below (section 4.5).

4.2 Object definitions

In section 3.11 I described how the different physics objects (jets, electrons, muons and missing transverse energy E_T^{miss}) are reconstructed in ATLAS. Now I introduce the basic kinematic cuts and identification prescriptions used in this analysis.

The basic electron candidates, reconstructed by the standard ATLAS electron reconstruction algorithms, must fulfil medium identification requirements (see section 3.11.2). Moreover, the selected electrons must have $p_T > 20$ GeV and $|\eta^{cl}| < 2.47$, where η^{cl} is the pseudo-rapidity of the electron calorimeter cluster. If an electron overlaps with a jet ($0.2 < \Delta R < 0.4$)[1], then the electron candidate is rejected. A particular request takes in account for the dead OTX. For the final selection, we define "signal electrons" requiring tight identification requirements (presented in section 3.11.2), track-match. In addition they must be isolated, satisfying a track based isolation[2] ($p_T cone20/p_T < 0.10$) and if the leading lepton in the event is an electron it must have $p_T > 25$ GeV.

Selected muons are reconstructed using the STACO algorithm as either combined or segment-tagged muons (see section 3.11.3). The candidate muons must satisfy the requirements $p_T > 10$ GeV and $|\eta| < 2.4$. Furthermore, there

[1] I remember the definition of the distance $\Delta R = \sqrt{(\Delta\phi)^2 + (\Delta\eta)^2}$.

[2] With $p_T cone20$ we mean the sum of the p_T of all the tracks in a cone of $\Delta R = 0.2$ around the electron.

are requirements of hits in the different components of the inner detector of ATLAS in order to reconstruct the track in the detector and to ensure that is a real and good track. To reject cosmic muons, there are other two requests on the transverse impact parameter of the muon with respect to the primary vertex (d_0) and on the longitudinal impact parameter (z_0) that all the muons have to satisfy: $z_0 < 1.0$ mm and $d_0 < 0.2$ mm. The muons considered in the analysis, called signal muons, must be isolated, satisfying a track based isolation, $p_T cone20 < 1.8$ GeV and if the leading lepton in the dilepton event is a muon, it must have $p_T > 20$ GeV.

Jets are reconstructed using the anti-k_T jet clustering algorithm with a radius parameter $R = 0.4$. (the AntiKt4Topo algorithm, for further details see the section 3.11.4). They must have $p_T > 20$ GeV and $|\eta| < 2.8$. Jets must not overlap a selected electron within $\Delta R = 0.2$. Events containing a jet classified as bad jet, where the bad jets are jets not associated to in-time real energy deposits in the calorimeters, are removed in order to remove background events not produced by the proton-proton interactions, such as hardware problems (HEC spike, EM coherent noise), LHC beam conditions, and cosmic-ray showers.

The calculation of E_T^{miss} is based on the modulus of the vector sum of the transverse momenta of the reconstructed objects (jets and selected leptons), as seen in section 3.12.

4.3 Trigger strategy

The events for this analysis are drawn from two separate trigger streams: the Egamma stream and the Muon stream. Events in the Egamma stream are selected by requiring the presence of at least one electron with $p_T > 20$ GeV at the Event Filter level, whilst events in the Muon stream must present at least one muon with $p_T > 10$ GeV at the Event Filter level. We use the same triggers both for data and for Monte Carlo: EF_e20_medium as electron trigger and EF_mu18 as muon trigger. To avoid event duplication across the Egamma and Muon streams, the following prescription is adopted:

- all $e^{\pm}e^{\mp}$ di-electron events are taken from the Egamma stream in data with the appropriate electron trigger fired. The request of exactly two leptons in the event implicates no selected muons in addition to the two selected electrons. The p_T of the leading electrons must be greater than 25 GeV.

- All $\mu^{\pm}\mu^{\mp}$ di-muon events are taken from the Muon stream in data and must fire the muon trigger. There must be exactly two selected muons and no selected electrons. The p_T of the leading muons must be greater than 20 GeV.

- Different flavour $e^{\pm}\mu^{\mp}$ dilepton events are taken from both streams. In the Egamma stream we take events that have exactly one electron and

one muon, firing the electron trigger and with the leading electron with $p_T > 25$ GeV. Instead, from the Muon stream we take events for which the muon trigger is fired, having the leading muon with $p_T > 20$ GeV and that fail the electron trigger or not contain an electron with $p_T > 25$ GeV.

In Monte Carlo, events containing muons are re-weighted in order to have the same muon trigger efficiency for data and for Monte Carlo.

4.4 Event selection

In order to ensure that the selected events are really produced in the proton-proton interaction, the first step in the event selection consists in the rejection of events including either a bad jet or a candidate cosmic muon. For a significant part of the data statistics used in this analysis, because of a dead Front-End-Board (FEB), a region in the LAr calorimeter ($-0.1 < \eta < 1.5$ and $-0.9 < \phi < -0.5$) is dead. We discard events containing a selected jet or a good electron (that satisfies object selection) pointing to this $\eta - \phi$ region. We request the first primary vertex in the event have at least 5 tracks. This further cut allows to have a well defined first primary vertex and has the important consequence reducing the chance of selecting a cosmic event which typically have a primary vertex with only two tracks. Finally we select the events containing exactly two-leptons (electrons or muons) with $m_{ll} > 12$ GeV (to remove low-mass resonances, which are poorly modeled by the available Monte Carlo).

4.5 Pile-Up

During the first part of 2011, the peak luminosity of the LHC reached the $\sim 2 \times 10^{33}$ cm^{-2} s^{-1}; the bunches in the LHC are grouped in bunch trains with an in-train bunch separation of only 50 ns. This implies, considering an inelastic cross section of ~ 60 mb, that an average of 6 inelastic interactions will be produced for each beam crossing (pileup)[3].

In order to allow a meaningful comparison between data observations and Monte Carlo predictions, the superimposed interactions have to be simulated with the correct multiplicity. The Monte Carlo (MC) samples used to estimate the SM background have been produced before the data taking and include therefore on uncorrect simulation of the number of superimposed events per crossing. For the correct MC simulation bunch spacing of 50 ns has been considered and so the Monte Carlo sample events must be re-weighted in an appropriate way to reproduce the data conditions and so the pile-up. In order

[3]I remind that the rate R (that is the expected number of events per unit time) of a process is given by $R = L \cdot \sigma$ where L is the instantaneous luminosity and σ the cross section of the process.

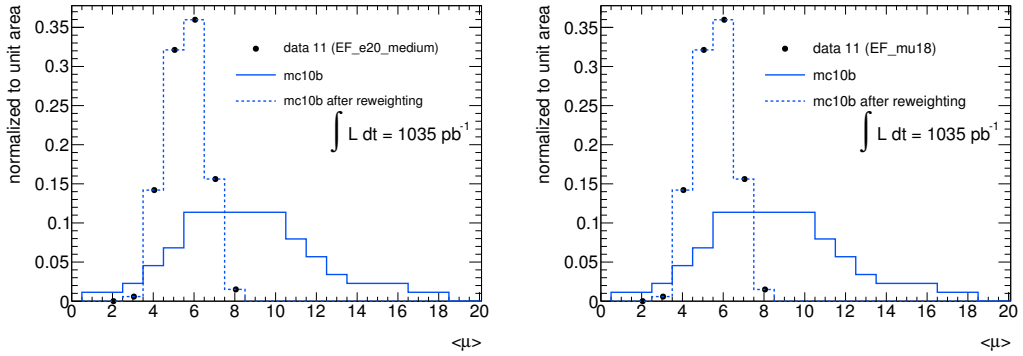

Figure 4.1: Distribution of $< \mu > |_{LB,BCID}$, the number of interactions averaged per luminosity block and bunch crossing ID. The simulated distributions for the Monte Carlo samples are shown for both egamma(a) and muon stream(b) separately. The data distributions (black dots) and initial Monte Carlo distributions (mc10b) show an evident discrepancy. Instead, after pileup reweighing (blue dotted), they show perfect agreement [59].

to obtain these weights, we considerer the average number of interactions per luminosity block and bunch crossing $< \mu > |_{LB,BCID}$. The distributions of $< \mu >$ are shown in Figure 4.1 for Egamma and Muon stream separately. The discrepancy between MC and data is evident. All Monte Carlo samples are produced with the same fixed $< \mu >$ distribution (see Figure 4.1). So, the pileup weights for the MC events for Egamma and Muon streams are singularly obtained to reproduce the correct multiplicity and the $< \mu >$ distributions observed and measured in data. These weights are listed in Table 4.1.

4.6 Signal regions

The signal region (SR) is the region of the space of the parameters where the signal (the hypothetical supersymmetry signal) is expected to be dominant, with a reduced background of Standard Model processes. Therefore, to select an appropriate SR, we must consider a specific benchmark model: in the chosen model, we calculate the expected signal S and optimize the significance $S/\sqrt{B}$, where B is the Standard Model predicted background. This optimization allows to select the signal regions where we will seek the supersymmetry events.

The flavour subtraction analysis has been performed in parallel to an inclusive two lepton analysis; in this analysis, we investigate phase space regions not covered by the inclusive analysis. The choice to enlarge the inclusive signal regions increases the possible signal statistics. The first two signal regions considered are:

1. **(FS-SR1)** $E_T^{miss} > 80$ GeV with a veto over the dilepton invariant mass range between 80 and 100 GeV.

Table 4.1: Weights for Monte Carlo pileup re-weighting. They are based on GRL for Egamma and Muon stream for the runs 178044-184169 and the corresponding triggers EF_e20medium and EF_mu18.

	mc10b	
$< \mu >$	egamma stream	muon stream
0	0	0
1	0	0
2	0.00218437	0.00218467
3	0.258861	0.258897
4	3.1242	3.12463
5	4.71067	4.71132
6	3.16552	3.16595
7	1.37379	1.37384
8	0.13261	0.131571
9	0	0
10	0	0

2. **(FS-SR2)** $E_T^{miss} > 80$ GeV and 2 or more jets.

It's interesting to note that these signal regions are thought to reduce the background (as Z+jets) irreducible for the flavour subtraction analysis. Instead, these signal regions are not optimized to suppress the reducible top background. Both the (similar) signal regions are considered because they are complementary in the search of SUSY signals that could have either low number of jets or a mass edge overlapping the Z mass region.
On the other hand, we decide to include a third signal region, also studied in the inclusive analysis. We require a high E_T^{miss} cut in order to increase the significance of hypothetical signal with regards to the total background. The signal region proposed is:

1. **(FS-SR3)** $E_T^{miss} > 250$ GeV.

This signal region permits the use of data-driven estimations for top provided by the dilepton group.

4.7 Estimation of Standard Model background

In order to understand and interpret in a correct way the results of an analysis on real data events, it is essential to estimate the Standard Model process contributions to the final numbers and distributions. If this is true for every physics analysis (also for Standard Model one), this estimation is even more important in an analysis searching new physics: it is only the comparison between data and Standard Model to allow to draw conclusions on the eventual presence of new physics in the data collected and to put exclusion limits.

The main Standard Model backgrounds to an analysis selecting two leptons (opposite sign) events are:

* $Z/\gamma^* \rightarrow ll$+jets
* fully-leptonic $t\bar{t}$
* dibosons
* single top
* fakes, that is events with one or both the leptons of the event that are not real leptons but isolated no leptonic tracks (generally jets) that fake the lepton passing the definition cuts. The main fake sources are single top, $W \rightarrow l\nu$+jets, QCD, heavy-flavour decays and semi-leptonic $t\bar{t}$.

For a general opposite sign dilepton analysis the dominant background is represented by $t\bar{t}$ events. However, in the flavour subtraction analysis, the $t\bar{t}$ events are naturally canceled because of the top (antitop) quark decays with the same branching ratio into electrons and muons (and so identical flavour and different flavour dilepton events are expected in the same number). As we will see in the following, this cancellation is not perfect, therefore the residual $t\bar{t}$ background after the subtraction must be estimated in order to interpret the results in the correct way in terms of an (eventual) excess with respect to the Standard Model. The main background in my analysis is constituted by $Z/\gamma^* \rightarrow ll$+jets background since only identical flavour dilepton events are produced.

The Standard Model backgrounds are estimated using a combination of data-driven, partially data-driven and Monte-Carlo-only techniques. The Monte Carlo datasets (introduced in section 4.1.2 and reported in Appendix) provide the first and immediate tool for the comparison between Standard Model predictions and data observations. I show the data - Monte Carlo comparison presenting the distributions of the most interesting variables for the three dilepton opposite sign channels ($e^{\pm}e^{\mp}$, $\mu^{\pm}\mu^{\mp}$ and $e^{\pm}\mu^{\mp}$): the missing transverse energy (E_T^{miss}) in figure 4.2, the dilepton invariant mass in figure 4.3 and the jet multiplicity in figure 4.4. In the plots, only the events passing the event selection cuts presented in section 4.4 are included. The Standard Model contributions predicted by the Monte Carlo are normalized to the data integrated luminosity and superimposed on the data observations (depicted with black points) in order to make evident and clear the comparison. Both the results are represented with the appropriate errors: the data observations with the statistical uncertainty, while the Monte Carlo results with an error band including the statistical and the systematic contributions to the total uncertainty. The sources of systematic uncertainty are introduced in the next section 4.7.1. I chose to show these distributions since the signal regions studied in the flavour subtraction analysis (see section 4.6) are just defined with cuts on these three variables; only if the agreement between data and Monte Carlo simulations

is good at this point, we can apply further cuts to define and investigate the signal regions and have a valid tool to interpret the analysis results in terms of eventual Supersymmetry signal. From the figures, we can ascertain the satisfactory agreement between data and Monte Carlo (Standard Model) predictions: they are compatible within the assumed uncertainty. After the event selection cuts, the main Standard Model contributions are represented by the Z and $t\bar{t}$ processes. The analogue distributions for the events in the signal regions of the flavour subtraction analysis are shown in the analysis section 4.10 (figure 4.16 for the E_T^{miss} distribution, figure 4.15 for the invariant mass and figure 4.17 for the jet multiplicity).

After having dealt with the data-Monte Carlo comparison, now we can treat the partially data-driven techniques of estimation. So in the next sections I give a brief overview of the partially data-driven estimations; the only Monte Carlo predictions for the single top and diboson backgrounds are shown in the complete tables of the flavour subtraction analysis (section 4.8). For completeness I report also estimations performed by other members of the ATLAS SUSY group. However, the not original work is limited to backgrounds less important: the cosmic muons (coming from the sky, component of the cosmic rays arriving till the Earth) (section 4.7.2), fakes (section 4.7.3) and $t\bar{t}$ (section 4.7.5). Instead, I perform the more important and fundamental data-driven estimation of the Z background. These estimations have many possible uncertainties that must be considered to perform a correct study and refine the interpretation of the results. Only taking into account these uncertainties the comparison between data and Standard Model estimates can be done in a robust and a reliable way (as we have made in the figures showing the dilepton distributions). So, before describing the estimation of the Standard Model processes and backgrounds, in the next section I briefly describe the various systematic uncertainties and their impact on the analysis (in additional to the statistical uncertainty due to limited Monte Carlo statistics, often denoted stat.).

4.7.1 Systematic uncertainties

The systematic uncertainties which will be considered in my work are:

Luminosity: the uncertainty on the luminosity is taken to be 3.7% [60].

Cross Section: the uncertainty due to the cross-section is taken to be 5% for most Monte Carlo samples considered. However, there are two exceptions to this: QCD and $t\bar{t}$. For QCD, we assign a cross-section uncertainty of 100% to account for the expected poor-modeling of fake events in Monte Carlo. Instead we assign 7% uncertainty on the $t\bar{t}$ cross-section based [61, 62].

JES$_{up/down}$: the energy of hadronic jets, as measured in the calorimeter, has an intrinsic scale uncertainty. If the jet energy (and momentum) is varied

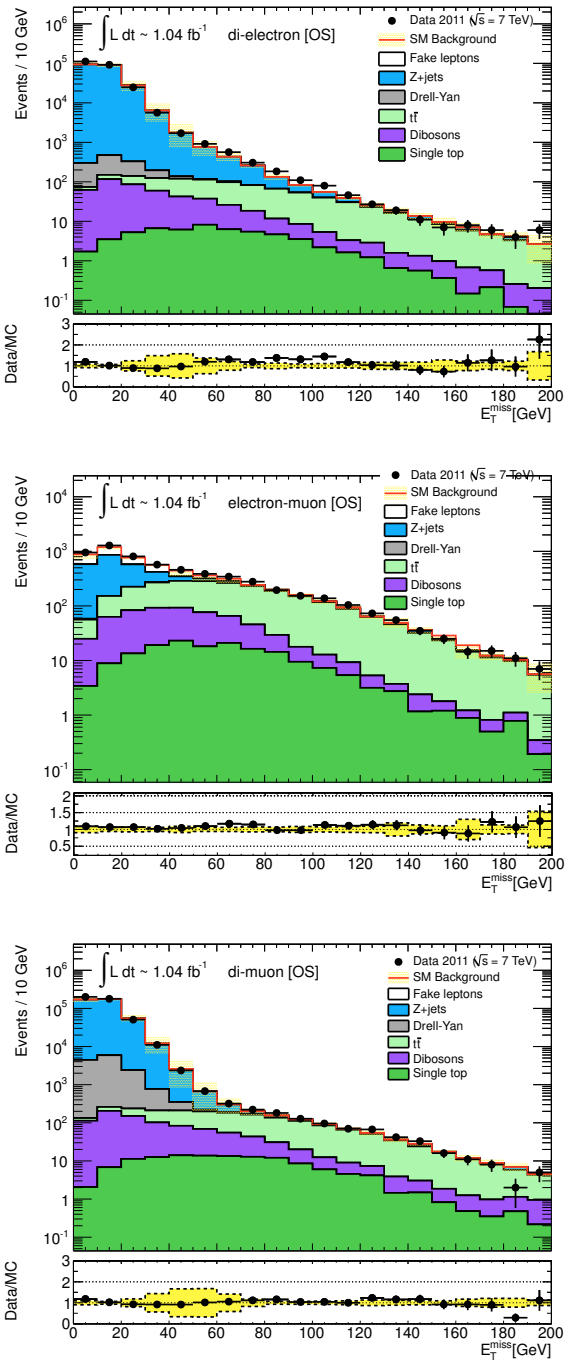

Figure 4.2: Distributions of the transverse missing energy (E_T^{miss}) of two-lepton events in data and Monte Carlo in the three opposite-sign channels $e^{\pm}e^{\mp}$ (top), $e^{\pm}\mu^{\mp}$ (center) and $\mu^{\pm}\mu^{\mp}$ (bottom). Errors on data points are statistical Poisson limits, whilst the error band on the Monte Carlo represents the statistical, cross-section, luminosity uncertainties and JES, JER (see section 4.7.1). In the bottom histogram the black data points and the yellow uncertainty band have been divided by the total Monte Carlo to show whether the fractional deviation of the data from the Monte Carlo lies within the uncertainty band. The Monte Carlo line is the sum of all the Standard Model backgrounds.

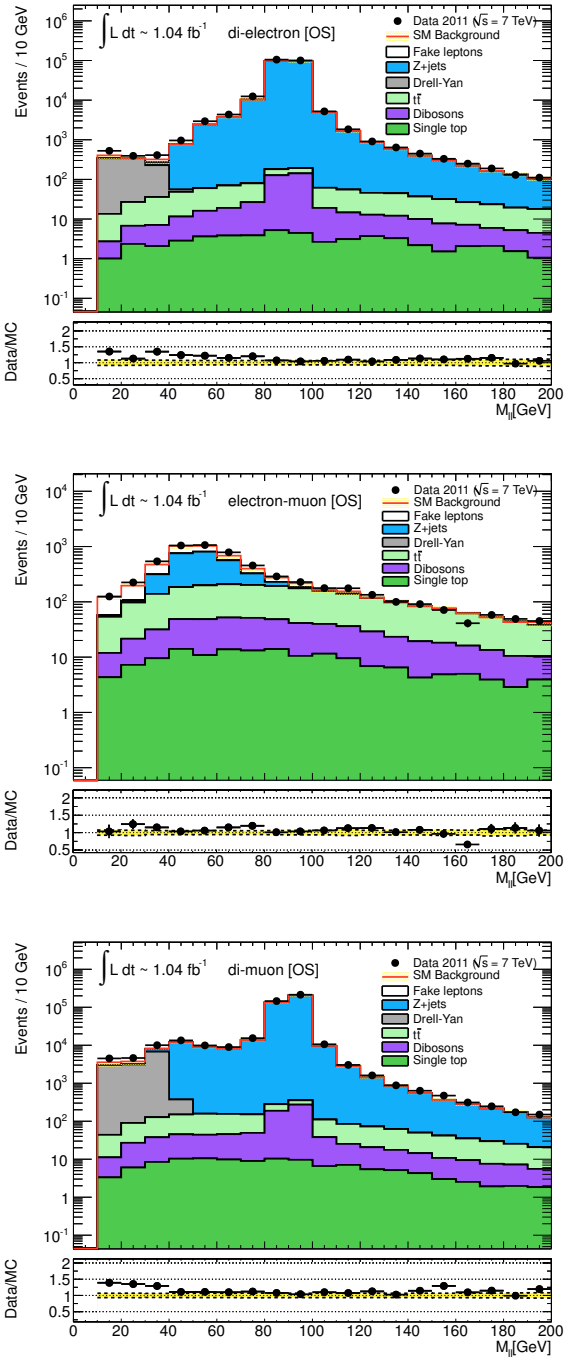

Figure 4.3: Distributions of the invariant mass ($m_{\ell\ell}$) of two-lepton events in data and Monte Carlo in the three opposite-sign channels $e^{\pm}e^{\mp}$ (top), $e^{\pm}\mu^{\mp}$ (center) and $\mu^{\pm}\mu^{\mp}$ (bottom). Errors on data points are statistical Poisson limits, whilst the error band on the Monte Carlo represents the statistical, cross-section, luminosity uncertainties and JES, JER (see section 4.7.1). In the bottom histogram the black data points and the yellow uncertainty band have been divided by the total Monte Carlo to show whether the fractional deviation of the data from the Monte Carlo lies within the uncertainty band. The Monte Carlo line is the sum of all the Standard Model backgrounds.

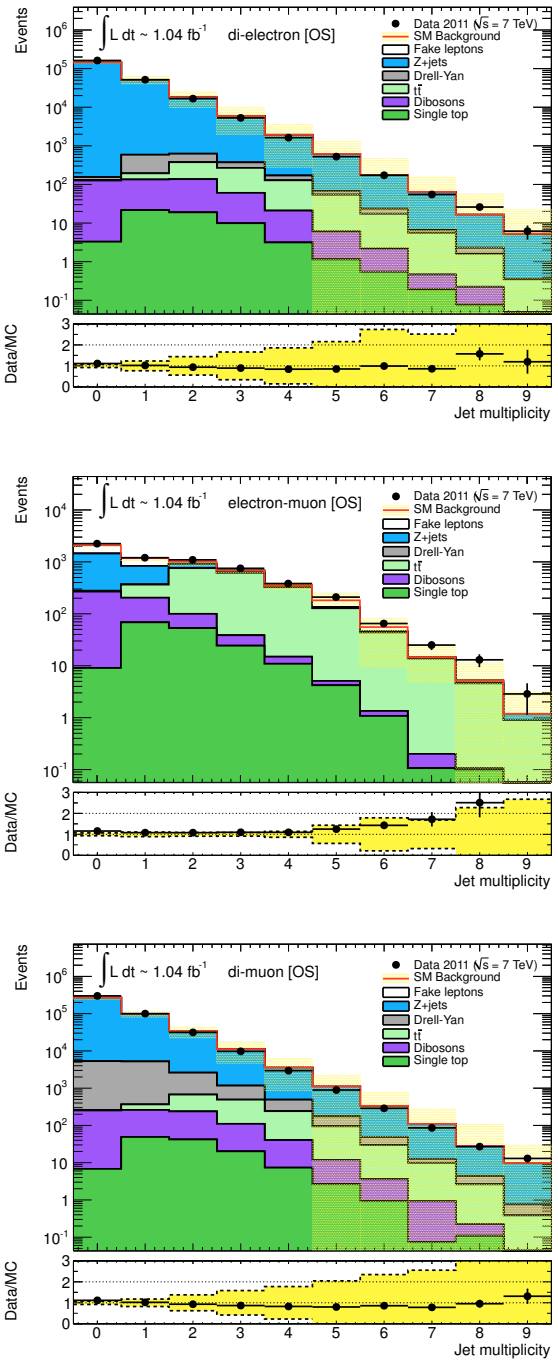

Figure 4.4: Distributions of the jet multiplicity of two-lepton events in data and Monte Carlo in the three opposite-sign channels $e^{\pm}e^{\mp}$ (top), $e^{\pm}\mu^{\mp}$ (center) and $\mu^{\pm}\mu^{\mp}$ (bottom). Errors on data points are statistical Poisson limits, whilst the error band on the Monte Carlo represents the statistical, cross-section, luminosity uncertainties and JES, JER (see section 4.7.1). In the bottom histogram the black data points and the yellow uncertainty band have been divided by the total Monte Carlo to show whether the fractional deviation of the data from the Monte Carlo lies within the uncertainty band. The Monte Carlo line is the sum of all the Standard Model backgrounds.

Table 4.2: Additional uncertainty for JES pileup correction.

	$0< \eta <2.1$	$2.1< \eta <4.5$
$20 < p_T < 50$ GeV	5%	7%
$50 < p_T < 100$ GeV	2%	3%
$p_T > 100$ GeV	no add. uncertainty	

within the estimated uncertainties, the results of the analysis change. This term of systematics takes into account the asymmetric uncertainty due to the scaling of the jet energy up or down. We can evaluate it using a particular and appropriate tool provided by the Jet Combined group. In order to perform a correct estimate of this systematic, we have to take into account also the significant increase of the pile-up in 2011 runs. So another uncertainty has to be added in quadrature: in Tab. 4.2 you can find the relative contribution, derived from the expected difference from data and MC of the jet offset calculated from the mean tower energy in the zero-bias stream.

JER: this systematic considers the impact of additional jet energy resolution [63]. Each jet is smeared according to a Gaussian distribution, with unit mean, and a width (sigma) given by the p_T (where p_T is given in units of GeV) dependant resolution function (Equation 4.1):

$$0.55\sqrt{\frac{(4.6)^2}{p_T^2} + \frac{0.846^2}{p_T} + 0.064^2} \tag{4.1}$$

The JER provider provides JER uncertainties up to $p_T = 500$ GeV and $|\eta| = 2.8$. An extra absolute uncertainty of 7% has to be added, if the jets is in $|\eta|$ >2.8 (this is a conservative estimate). All jets above the η and p_T boundaries are calculated with the boundary values.

$E_{e,up/down}$**:** this is an asymmetric uncertainty due to the scaling up or down of the electron energy scale.

$\mu_{MS,up/down}$ **and** $\mu_{ID,up/down}$**:** these are the asymmetric uncertainties on the scale of the MS and ID components of muon p_T. We apply Monte Carlo muon momentum corrections based on the muon momentum resolution [64].

res$_e$**:** this uncertainty considers the impact of additional electron energy resolution. The electron energy is smeared using a Gaussian with p_T (in GeV) and η dependent sigma. This function is given by:

$$\sqrt{(S(1+\Delta S)\sqrt{E_{cl}})^2 + (C(1+\Delta C)E_{cl})^2 - (S\sqrt{E_{cl}})^2 - (CE_{cl})^2} \tag{4.2}$$

where S and C are the sampling and constant terms (0.1 and 0.007 respectively), ΔS is the uncertainty on the sampling term (0.2), and ΔC

is the uncertainty on the constant term (1% in the barrel and 4% in the end-cap).

pdf: this is the uncertainty due to uncertainties in the parton distribution functions. In our analysis for this uncertainty source it is assigned a conservative 5% error.

For all the uncertainties which affect object definitions, the missing transverse energy is corrected accordingly: each object in the container is removed (vectorially) from the missing energy and the object added back in, but with corrected contributions to the x and y components.

4.7.2 Cosmic estimation

Cosmic rays are energetic charged subatomic particles, originating in outer space. They may produce secondary particles that penetrate the Earth's atmosphere and surface. When a cosmic ray traverses the ATLAS detector, a cosmic muon can be reconstructed as two back-to-back, opposite sign muons, and in such way it can affect the analysis of the pp collision. To avoid this and reduce the cosmic contamination in the final states selected for the analysis, we must look for variables able to discriminate between the muons from the collisions and the cosmic muons. A consideration can drive our choice and research: the cosmics traverse the detector randomly in space and time since their downward flux through the detector is homogeneous; so the track and the impact parameters d_0^{PV} and z_0^{PV} respect on the primary vertex (PV) can be the sought variables. In fact, after a good identification of the primary vertex (for such purpose in the event selection we request that the primary vertex has at least 5 tracks associated), for the cosmic muons these variables are expected to be uniform and homogeneously distributed, whilst for the collision muons they should be peaked near the interaction point. The $|z_0^{\mathrm{PV}}|$ and $|d_0^{\mathrm{PV}}|$ distributions (of the isolated muons passing the trigger, vertex and cleaning cuts) shown in Figure 4.5 confirm the correctness of our supposition: the muons from hard scattering processes, identifiable in the figures by the high number they are produced (and detected) in a narrow region respect on the primary vertex, are concentrated at very low values of $|z_0^{\mathrm{PV}}|$ and $|d_0^{\mathrm{PV}}|$ whilst the muons corresponding to cosmic rays (more random and produced in a number of many orders of magnitude less than those from the pp collisions), characterized by a low multiplicity, are distributed also at high values of $|z_0^{\mathrm{PV}}|$.

For estimating the content of cosmic muons in the data in the regions of interest (typically the signal regions), we exploit these variables to define a control region containing a pure cosmic sample. Then, a scale factor permits to retrieve the cosmic contamination in the data as the product of the number of cosmics in the pure sample and the scale factor [66]. For this aim, we reverse the $|z_0^{\mathrm{PV}}| < 1$ mm and $|d_0^{\mathrm{PV}}| < 0.2$ mm cuts used for the cosmic rejection in the event selection (section 4.4).

Figure 4.6 shows the $|z_0^{\mathrm{PV}}|$ distribution for the muons passing the cut against cosmics on the transverse impact parameter d_0^{PV}: it is crucial for understanding how we can choose the cosmic control region and the appropriate scale factor that connects it with the analysis region with $|z_0^{\mathrm{PV}}| < 1$ mm. There are two methods for estimating the cosmic contribution to the signal-like muon region. The first one exploits the uniformity of the longitudinal impact parameter z_0^{PV} and the consequent approximately flat shape of the distribution. The control region is formed by the slice of the muons with $T_\ell < |z_0^{\mathrm{PV}}| < T_h$ mm, where T_ℓ is an appropriate lower threshold and T_h is the similar higher threshold. Exploiting the behaviour of the z_0^{PV} distribution, the scale factor is provided simply by the ratio between the control regions area and the signal region area:

$$N_{\mathrm{cosmics}}(|z_0^{\mathrm{PV}}| < 1 \text{ mm}) = \frac{1 \text{ mm}}{|T_\ell - T_h| \text{ mm}} \times N_{\mathrm{muons}}(T_\ell < |z_0^{\mathrm{PV}}| < T_h \text{ mm}) \quad (4.3)$$

The dependence of the cosmic estimation on the variations of the lower and upper bound of the control region is a source of systematics associated with the method. Table 4.3 presents the observed number of events for different control region definitions and the corresponding estimations for $|z_0^{\mathrm{PV}}| < 1$ mm. If we choose a too small value T_ℓ for the control region lower boundary ($|z_0^{\mathrm{PV}}| >$ 1 mm) we have an increasing of the cosmic muon estimation due to the contamination from collision-like muons. So, this first technique estimates 6.1 $\pm$ 1.4(stat) $\pm$ 1-3(syst) cosmic muons $|z_0^{\mathrm{PV}}| < 1$ mm in events with 2 muons.

	N_{muons}		$N_{\mathrm{cosmics}}(\lvert z_0^{\mathrm{PV}}\rvert < 1$ mm)	
	$\lvert z_0^{\mathrm{PV}}\rvert < 100$ mm	$\lvert z_0^{\mathrm{PV}}\rvert < 150$ mm	$\lvert z_0^{\mathrm{PV}}\rvert < 100$ mm	$\lvert z_0^{\mathrm{PV}}\rvert < 150$ mm
$\lvert z_0^{\mathrm{PV}}\rvert > 1$ mm	2114	2242	21 $\pm$ 2	15.0 $\pm$ 1.6
$\lvert z_0^{\mathrm{PV}}\rvert > 5$ mm	576	704	6.1 $\pm$ 1.4	4.9 $\pm$ 1.0
$\lvert z_0^{\mathrm{PV}}\rvert > 10$ mm	541	669	6.0 $\pm$ 1.3	4.8 $\pm$ 1.0

Table 4.3: Number of observed muons in the control region and corresponding estimation of cosmics at $|z_0^{\mathrm{PV}}| < 1$ mm with the first method on 1.04 fb^{-1} of data for different control region definitions. Uncertainties are statistical only [59].

The second method, as the first, builds a cosmic control region using the z_0^{PV} variable; however, it doesn't rely on the approximation of flat $|z_0^{\mathrm{PV}}|$ distribution, but it stresses the failures of this approximation at very high and low values (where there is the signal muon region) of this variable. In order to describe in a better and more accurate way these extremes, the distribution is fitted with a gaussian curve. Fixing the parameters of the gaussian fit in an appropriate control region, the cosmic contribution in the signal region is retrieved. The conservative estimation of this technique is of 5.4 $\pm$ 0.4(stat) $\pm$ 0.5(syst) cosmics muons at $|z_0^{\mathrm{PV}}| < 1$ mm.

In order to complete the estimate, we must considerer the effect of the cuts on E_T^{miss}, multiplicity of jets and $m_{\ell\ell}$ that define the signal region of the flavour subtraction. The performed studies show that the application of these cuts makes the already small cosmic contamination of the signal sample negligible.

These results concern the dimuon events. Obviously, we could also have a coincidence of a single reconstructed collision electron and a single reconstructed cosmic muon and so have a cosmic contribution to the $e\mu$ channels. However, it is much less likely[4] than the coincidence of two reconstructed muons from a cosmic event and any collision event. This sets a conservative estimate of the contribution in the $e\mu$ channels of $\leq 10^{-3}$.

[4]We cut very tightly on the d_0 and z_0 of muons with respect to the first primary vertex, and the events described must have leptons from two different vertices.

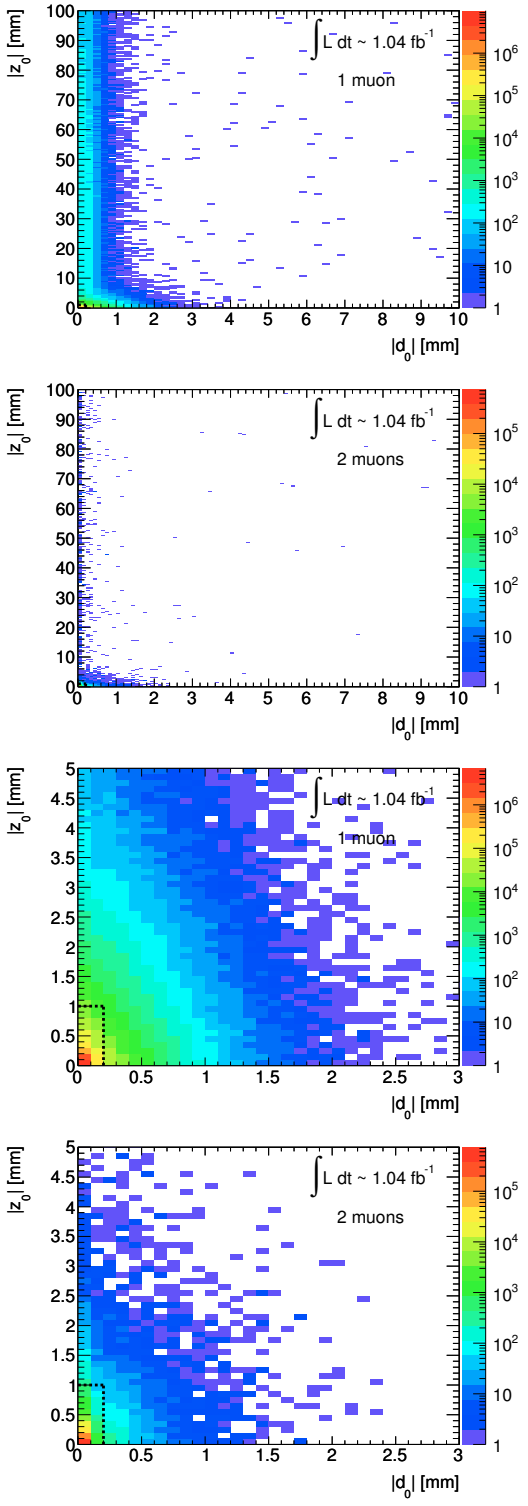

Figure 4.5: Distribution of $|z_0^{\mathrm{PV}}|$ and $|d_0^{\mathrm{PV}}|$ for selected muons in events with one muon (top) and two muons (bottom). Plots at the bottom show a zoom of the top distributions in the $|z_0^{\mathrm{PV}}| < 5$ mm and $|d_0^{\mathrm{PV}}| < 3$ mm region. Each entry corresponds to one muon, not to one event. Dashed lines denote the cut values used to select signal-like muons [59].

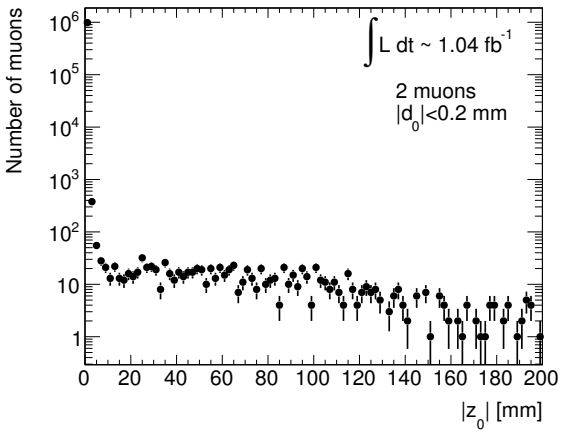

Figure 4.6: Distribution of $|z_0^{\mathrm{PV}}|$ for muons with $|d_0^{\mathrm{PV}}| < 0.2$ mm [59].

4.7.3 Fake estimation

The fake dilepton event is an event where one or both the leptons of the event are not real leptons but isolated no leptonic tracks (generally jets) that fake the lepton passing the definition cuts. This is the dominant background for the dilepton same sign analysis, whilst in the dilepton opposite sign analysis is secondary. In a dilepton opposite sign analysis, the main processes that contribute to the events with at least one fake lepton are W+jets and semi-leptonic $t\bar{t}$ (with a real lepton from the W decay and a jet faking a lepton), $b\bar{b}$ where the light or heavy flavour jet fakes a lepton. Fake muons are also those from heavy flavour decays. The fake background estimation is performed using a Matrix Method [67]. At the base of this method of estimate, there is the capability to distinguish a real lepton from a fake one. Two different selection criteria for the leptons are defined:

tight: these leptons pass all standard object selection requirements as described in section 4.2;

loose: these leptons are defined in order to enhance (fake) leptons originating from QCD-processes; the electron and muon identification requests are looser: we accept electrons fulfilling "medium" requirement (instead of tight, as for the standard signal electrons) and invert the isolation cut on both the muons and electrons.

To give a sense to this selection criteria we need to determine the composition of the samples in terms of real (R) and fake (F) leptons passing the selection criteria; to do that it's necessary the calculation of the probabilities r and f for leptons real and fake respectively to pass these requirements. In fact, using these probabilities the matrix method allows to estimate the expected contribution to the signal region from events containing fake leptons scaling with an appropriate factor the number of observed events in data in the signal region (obviously containing loose-loose (LL), loose-tight (LT), tight-loose (TL) and tight-tight (TT) lepton pairs). These factors can be obtained inverting equation 4.4.

$$\begin{bmatrix} N_{TT} \\ N_{TL} \\ N_{LT} \\ N_{LL} \end{bmatrix} = \begin{bmatrix} rr & rf & fr & ff \\ r(1-r) & r(1-f) & f(1-r) & f(1-f) \\ (1-r)r & (1-r)f & (1-f)r & (1-f)f \\ (1-r)(1-r) & (1-r)(1-f) & (1-f)(1-r) & (1-f)(1-f) \end{bmatrix} \begin{bmatrix} N_{RR} \\ N_{RF} \\ N_{FR} \\ N_{FF} \end{bmatrix} \tag{4.4}$$

The problem about the determination of real and fake probabilities is solved using pure control regions, where the leptons are expected to be mainly real or fake. The fraction of leptons passing the tight cuts gives the real efficiency and the fake-rate. The quality of the estimation mainly depend on the purity of the chosen control region. For the real efficiency, the choice is easier; we can extract the real efficiency from a Z control region defined by the request

of exactly 2 leptons of opposite sign and identical flavour, and with invariant mass within 5 GeV of the nominal Z mass (that is the window 86-96 GeV). The choice of the fake-control region is a bit trickier; it is a QCD enriched region and the QCD background is more difficult to handle. The definition cuts of this region involve the E_T^{miss}, the jet multiplicity, the dilepton invariant mass and the azimuthal distance between E_T^{miss} and leptons and their variations allow to build many fake control regions. The choice of which QCD control region to use is a compromise of fake rate stability (moving near this region), statistics and purity, where the purity is defined by subtracting the contamination processes from the data, where the contamination of a certain QCD control region is the amount of prompt leptons in this region:

$$\text{purity} = \frac{N_{\text{data}}^{\text{dilep}} - N_{\text{not-QCD}}^{\text{dilep}}}{N_{\text{data}}^{\text{dilep}}} \quad \sim \quad \frac{N_{\text{QCD}}^{\text{dilep}}}{N_{\text{data}}^{\text{dilep}}}$$

In addition to, we check the compatibility of the composition in the QCD control region and the signal regions. Therefore the final choice of control region does not critically influence the method:

- the control region for muons is defined by the cut: $E_T^{miss} < 30$ GeV;
- the control region for electrons is characterized by: $E_T^{miss} < 30$ GeV, $\Delta\phi(lep, E_T^{miss}) < 0.5$ and $N_{jets} >= 1$.

At this point, from the real and fake control regions just defined, we can retrieve the fake-rates and real efficiencies. The real efficiency for a dilepton event is given by

$$\tilde{\epsilon}_{real} = \frac{N_{TT}}{N_{\sum TL}} = \frac{N_{TT}}{N_{Tl} + N_{lT} + N_{TT}} = \frac{rr}{2r(1-r) + rr}$$

where I indicate with "l" a lepton which passes loose selection, but fails tight, with "T" a lepton which passes tight selection, and with "L" a lepton which at least passes the loose selection; r represents the one-lepton real efficiency

$$r = \frac{2\tilde{\epsilon}_{real}}{1 + \tilde{\epsilon}_{real}} \tag{4.5}$$

Using the same notation, the fake-rate for a dilepton events is

$$\tilde{\epsilon}_{fake} = \frac{N_{\sum Tl}}{N_{\sum lL}} = \frac{N_{lT} + N_{Tl}}{N_{ll} + N_{lT} + N_{Tl}} = \frac{2(1-f)f}{(1-f)(1-f) + 2(1-f)f}$$

where f is the one-lepton fake-rate

$$f = \frac{\tilde{\epsilon}_{fake}}{2 - \tilde{\epsilon}_{fake}} \tag{4.6}$$

and so it can be simply calculated as

$$f = \frac{N_T}{N_L} = \frac{N_T}{N_l + N_T} \tag{4.7}$$

In all the equations N with any combinations of l, L and/or T, means the number of leptons, single or pairs, that are non-tight (l), inclusive loose (L) or tight (T). The notation N_{Tl} or N_{lT} indicates ordered lepton pairs, while $N_{\sum Tl}$ is the sum over the ordered Tl and lT pairs. In the real efficiency calculation we always require at least one tight lepton (tag), and for the fake-rate calculation always one non-tight lepton (anti-tag).

The real efficiency obtained from the Z control region is reported in Table 4.4, while the fake-rate are shown in Table 4.5.

	Efficiency	$N_{TT}/(N_{TT} + N_{T,l})$
Electrons	86.1515 ± 0.0595	412176/544687
Muons	98.5780 ± 0.0152	755025/21783

Table 4.4: The real efficiency measured from the Z control region. Numbers are quoted in percent [59].

	Fake rate	
	Rate	Purity
Electrons	10.96 ± 0.02	94.94
Muons	47.63 ± 1.26	98.54

Table 4.5: The fake rates including statistical error calculated from the chosen QCD control regions indicated in the text. All numbers are quoted in percent [59].

The statistical uncertainty on these event-weights (efficiencies) is calculated by adding or subtracting the statistical uncertainty to the lepton numbers and computing new weights. The average difference of the nominal and the upper and lower weight is the statistical uncertainty of the weights. In addition, the statistical uncertainty of the weighted number of total events (TT+Tl+lT+ll) is added in quadrature.

The systematic uncertainty takes into account the effect on the fake rates of the variation of the QCD control region. By taking the average of the differences between our nominal estimates and the estimates using a high and low fake rate we got a measure of the systematic uncertainty.

In table 4.7.3, I report the estimation for the fake contribution in the flavour subtraction signal regions FS-SR1 and FS-SR2, as obtained in [59]. For FS-SR3 the statistic is too poor to make a worthy estimation.

		FS-SR1	FS-SR2
$e^{\pm}e^{\mp}$	Est fake	5.27±2.393(syst.)±1.71(stat.)	1.50±0.662(syst.)±1.52(stat.)
	data	344	336
$e^{\pm}\mu^{\mp}$	Est fake	30.22±5.585(syst.)±6.12(stat.)	32.26±7.699(syst.)±6.30(stat.)
	data	750	741
$\mu^{\pm}\mu^{\mp}$	Est fake	21.76±4.911(syst.)±6.12(stat.)	19.38±5.788(syst.)±5.72(stat.)
	data	551	567

Table 4.6: Estimated fake (Est fake) contribution and number of observed events (data) in the flavour subtraction signal regions FS-SR1 and FS-SR2 in the $e^{\pm}e^{\mp}$, $e^{\pm}\mu^{\mp}$ and $\mu^{\pm}\mu^{\mp}$ channels [59].

4.7.4 Z+jets background estimation

As already observed, Z/γ^*+ jets represents an irreducible background for the flavour subtraction analysis since the Z decays in identical flavour lepton pair and not in different flavour one[5]. So its estimation is crucial for the interpretation of the excess of identical flavour dilepton events in the data in terms of new physics.

	FS-SR1	FS-SR2	FS-SR3
$e^{\pm}e^{\mp}$	75.40 ± 6.34 ± 6.04	50.64 ± 19.73 ± 4.78	0.01 ± 0.05 ± 0.01
$e^{\pm}\mu^{\mp}$	40.87 ± 4.12 ± 4.10	29.17 ± 5.97 ± 3.44	1.03 ± 0.04 ± 0.62
$\mu^{\pm}\mu^{\mp}$	37.42 ± 5.82 ± 3.64	42.77 ± 11.48 ± 4.04	0.74 ± 0.16 ± 0.53

Table 4.7: Number of the Z/γ^*+ jets dilepton opposite sign events predicted by using only Monte Carlo in the three signal regions of the flavour subtraction analysis. The systematic and statistical uncertainties are reported. The systematic error includes the cross-section, luminosity uncertainties and JES, JER (see section 4.7.1).

In addition to the only Monte Carlo estimation (reported in table 4.7 for the three dilepton channels $e^{\pm}e^{\mp}$, $e^{\pm}\mu^{\mp}$ and $\mu^{\pm}\mu^{\mp}$ for the three signal regions of the flavour subtraction analysis) we can use a partially data-driven technique. The method is common to other background data-driven estimations (and it has been just briefly introduced for the cosmic estimation): the first step is the definition of a good control region (CR) where the expected dominant contribution is given by the background under investigation, whilst the other

[5]The branching ratio for the Z boson in identical flavour leptons (electrons or muons) is 6.7%, whilst that in different flavour leptons is less than (2.4×10^{-3})% [3].

Standard Model processes and the expected signal are negligible or at least of little importance. This choice and check is obviously performed with the aid of the Monte Carlo. Then, the Monte Carlo predictions allow to evaluate the scale factor to pass from the number of events in the (background) control region to that in the signal region where the hypothetical supersymmetry signal is sought and expected to be maximal: this final number represents the estimation of the contribution of the considered background to the signal region.

Now, we can apply this general guideline to the Z/γ^*+ jets. If we take into consideration the distributions of the main variables for the two lepton events selected by the analysis cuts (the E_T^{miss} in figure 4.2, the dilepton invariant mass in figure 4.3 and the jet multiplicity in figure 4.4), it appears evident that the more discriminating variable is the dilepton invariant mass: under the mass peak of the Z boson, the Z+jets contribution is many order of magnitude greater than the sum of the other Standard Model backgrounds. So it seems obvious to define the Z control region requesting a dilepton invariant mass falling under an appropriate window around the Z mass peak. It's interesting to understand which width of the window can optimize the control region and how the estimation of Z contribution in the signal region depends on this choice. So I consider three different mass windows:

* $85 < m_{\ell\ell} < 95$ GeV
* $80 < m_{\ell\ell} < 100$ GeV
* $75 < m_{\ell\ell} < 105$ GeV

For evaluating the three choices, I take into account two features as terms of comparison and criteria for the selection: the ratio between Z and the other Standard Model background contributions and the purity. They are similar and related, but while the ratio between Z and the other backgrounds is computed only exploiting the Monte Carlo predictions, the purity is calculated using also the data observations (see the following definition in equation 4.8). Obviously, the ideal control region is that with the highest ratio Z background to the other ones and that minimizes the error (statistical and especially systematic) on the estimation in the signal region; in fact, these are just the purposes we design the control region. The purity of the sample (already introduced for the fakes) can be defined as:

$$\text{purity} = \frac{N_{\text{data}}^{\text{dilep}} - N_{\text{not-}Z}^{\text{dilep}}}{N_{\text{data}}^{\text{dilep}}} \tag{4.8}$$

It is defined as the fraction of the data events expected coming from the Z background on the total data events falling under the relative Z peak mass; so it gives a quantitative estimate of the purity of the data sample selected. This feature is closely connected to the first one; also in this case, the ideal control region has the highest purity. In table 4.8 I report the results obtained

for the three mass windows. As expected, the most narrow window is that which appears preferable: the 99.84% of the MC events comes from the Z. In order to have a greater robustness of the control region against eventual fluctuations, I select also the second mass window (80-100 GeV). In fact, a larger control region can allow a reliable and more accurate description and estimation of the Z contribution in the signal region; the purity is good and the Z represents the 99.81% of the total Standard Model background (according to the Monte Carlo predictions). So I use both the first two cuts as base cuts for the definition of the control region. Furthermore, this choice allows me to study the systematic effect on the partial data-driven estimation due to the variation of the control regions.

	$85 < m_{\ell\ell} < 95$ GeV	$80 < m_{\ell\ell} < 100$ GeV	$75 < m_{\ell\ell} < 105$ GeV
	$e^{\pm}e^{\mp}$		
$N(ee)$ from Z	163083.97 ± 403.84	194352 ± 440.85	204487.31 ± 452.20
$N(ee)$ from other bg	268.81 ± 16.40	377.98 ± 19.44	453.26 ± 21.29
$N(ee)\|_Z/N(ee)\|_{noZ}$	606.69	514.18	451.15
Purity	0.9984	0.9981	0.9979
	$\mu^{\pm}\mu^{\mp}$		
$N(\mu\mu)$ from Z	288161.56 ± 536.81	341372.31 ± 584.27	356487.16 ± 597.07
$N(\mu\mu)$ from other bg	453.17 ± 21.29	640.14 ± 25.30	778.28 ± 27.90
$N(\mu\mu)\|_Z/N(\mu\mu)\|_{noZ}$	635.88	533.28	458.04
Purity	0.9985	0.9982	0.9979
	Total $\ell\ell$		
$N(\ell\ell)$ from Z	451245.53 ± 671.75	535724.31 ± 731.93	560974.47 ± 748.98
$N(\ell\ell)$ from other bg	721.98 ± 26.87	1018.13 ± 31.91	1231.54 ± 35.09
$N(\ell\ell)\|_Z/N(\ell\ell)\|_{noZ}$	625.01	526.19	455.50
Purity	0.9985	0.9982	0.9979

Table 4.8: Number of Z events and of other Standard Model processes in the three different invariant mass windows obtained from the Monte Carlo simulations. It is reported also the ratio between the number of Z events and that of the remaining backgrounds and the purity of the samples. The error is only statistic.

The purity of the samples are high. However, as we can see in figure 4.7 (and figure 4.8), the contributions of $t\bar{t}$ and especially diboson events are still significant. So, for reducing this signal contamination in my control regions, I introduce a second cut. In figures 4.7 and 4.8, I show the E_T^{miss} distributions for the events (both simulated by the Monte Carlo and real) passing the first cut on the invariant mass ($85 < m_{\ell\ell} < 95$ GeV and $80 < m_{\ell\ell} < 100$ GeV respectively). The E_T^{miss} represents the second discriminating variable always used for the definition of a good Z control region: the Z decay in two charged leptons is characterized by a low missing transverse energy. So, the second cut

requests a $E_T^{miss} < 20$ GeV. In this way, I suppress the $t\bar{t}$ process, characterized by higher E_T^{miss} (due to the two neutrinos produced in the dilepton $t\bar{t}$ decay) and I appreciably reduce the diboson background that has a longer and more gradual tail respect on the Z. From table 4.9 it is possible assess the effects of this cut in the two mass window selected: after the E_T^{miss} cut, the $t\bar{t}$ background is almost null, whilst the diboson events are halved. So, we have a rise of the purity of the two control regions (they reach the same value of 99.92%) and of the ratio Z background to the other ones. Effectively, this couple of cuts is able to select two pure Z control regions.

CR1	$85 < m_{\ell\ell} < 95$ GeV	$+ E_T^{miss} < 20$ GeV
Total $\ell\ell$		
$N(\ell\ell)$ from Z	451245.53 ± 671.75	379595.50 ± 616.11
$N(\ell\ell)$ from other bg (no Z)	721.98 ± 26.87	308.37 ± 17.56
$N(\ell\ell)$ from $t\bar{t}$	137.63 ± 11.73	7.86 ± 2.80
$N(\ell\ell)$ from diboson	564.23 ± 23.75	299.36 ± 17.30
$N(\ell\ell)\|_Z / N(\ell\ell)\|_{noZ}$	625.01	1230.97
$N(\ell\ell)\|_Z / N(\ell\ell)\|_{t\bar{t}}$	3278.78	48284.44
$N(\ell\ell)\|_Z / N(\ell\ell)\|_{dib}$	799.76	1268.02
Purity	0.9985	0.9992

CR3	$80 < m_{\ell\ell} < 100$ GeV	$+ E_T^{miss} < 20$ GeV
Total $\ell\ell$		
$N(\ell\ell)$ from Z	535724.31 ± 731.93	448023.19 ± 669.35
$N(\ell\ell)$ from other bg (no Z)	1018.13 ± 31.91	380.74 ± 19.51
$N(\ell\ell)$ from $t\bar{t}$	277.70 ± 16.66	16.82 ± 4.10
$N(\ell\ell)$ from diboson	700.00 ± 26.46	361.38 ± 19.01
$N(\ell\ell)\|_Z / N(\ell\ell)\|_{noZ}$	526.19	1176.72
$N(\ell\ell)\|_Z / N(\ell\ell)\|_{t\bar{t}}$	1929.15	26630.26
$N(\ell\ell)\|_Z / N(\ell\ell)\|_{dib}$	765.32	1239.75
Purity	0.9982	0.9992

Table 4.9: Number of Z events and of other Standard Model processes in the two different invariant mass windows selected. In the table, the ratio between the number of Z events and of the remaining backgrounds and the purity of the samples are indicated. The contributions of $t\bar{t}$ and diboson, the two main backgrounds for the Z estimation, are reported in detail. The error is only statistic. Similar numbers are indicated for the control regions after the E_T^{miss} cut.

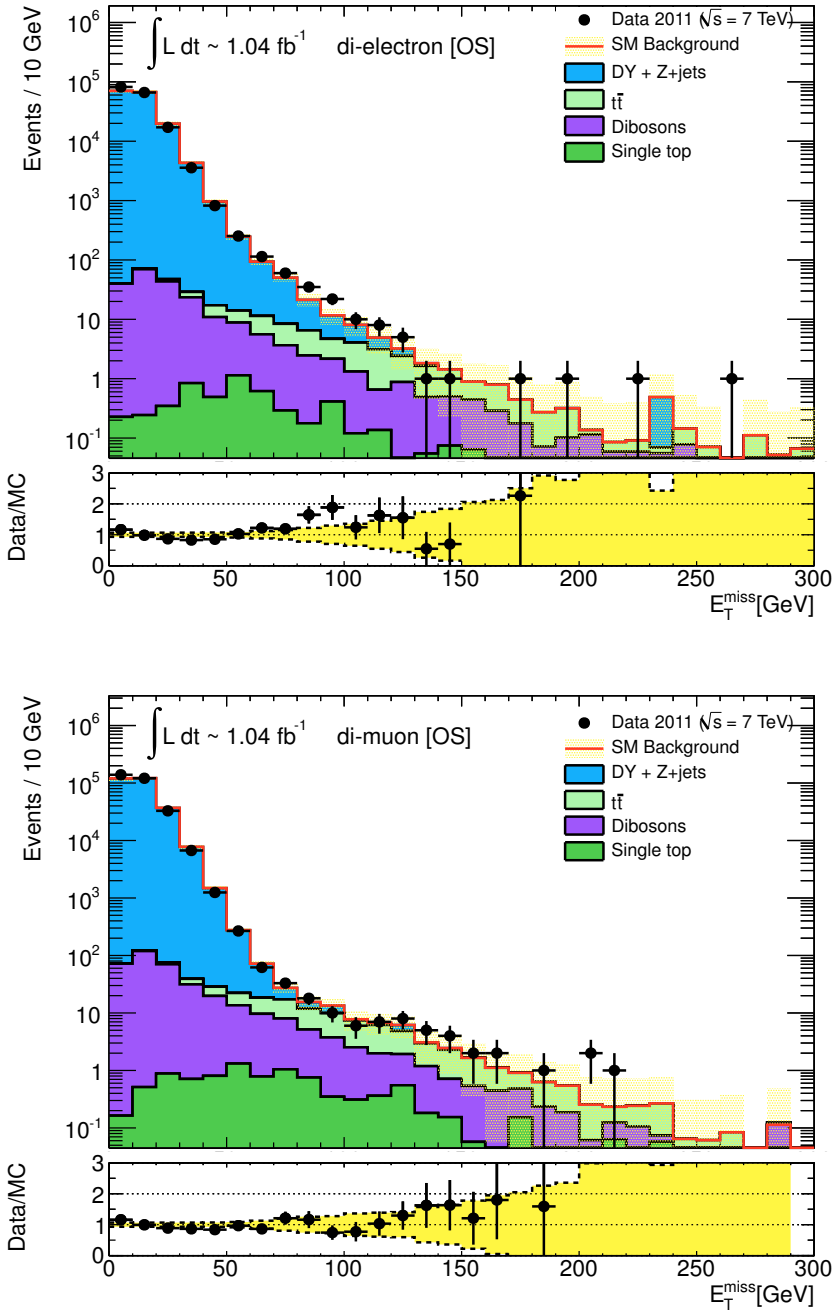

Figure 4.7: The E_T^{miss} distribution for opposite sign ee (top) and $\mu\mu$ (bottom) events with $85 < m_{\ell\ell} < 95$ GeV. This mass window is used for the definition of CR1 and CR2.

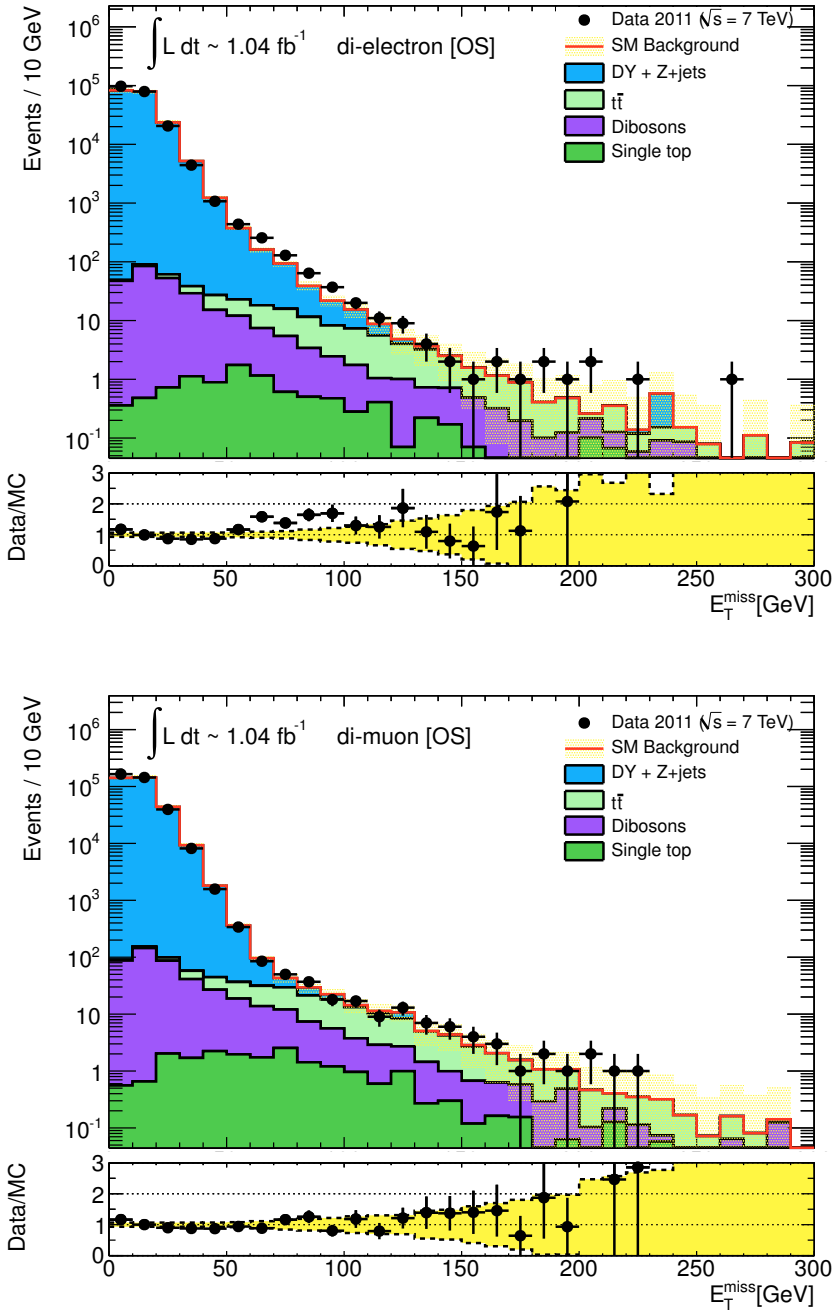

Figure 4.8: The E_T^{miss} distribution for ee (top) and $\mu\mu$ (bottom) events with $80 < m_{\ell\ell} < 100$ GeV. This mass window is used for the definition of CR3 and CR4.

At this point, I can define two different control regions[6]:

CR1: $85 < m_{\ell\ell} < 95$ GeV and $E_T^{miss} < 20$ GeV;

CR3: $80 < m_{\ell\ell} < 100$ GeV and $E_T^{miss} < 20$ GeV.

I exploit these two control regions to obtain two separate estimations of the Z contribution to the signal regions FS-SR1 and FS-SR3 of the flavour subtraction (see section 4.6 for the definition of the signal regions). The second signal region FS-SR2 presents a jet requirement (the number of jets in the event have to be at least 2), so it seems convenient and useful to introduce a similar request also in the definition of the control region in order to better reproduce the dynamics of the signal region and in consequence have two more homogenous regions. If we examine the distributions of the jet multiplicity of the events of the control regions CR1 and CR3 shown in figures 4.9 and 4.10 respectively, it is evident the extreme purity of the samples and it is possible foresee the effect of the introduction of the cut on the number of jets: the request of at least 2 jets in the events cuts away an important slice of Z events with 0 and only one jet, whilst the diboson events have generally an higher jet multiplicity. From the table 4.10, we can numerically realize the expected reduction of the purity in the last control regions. However, the ratio betwen the Z contribution and the other ones and the purity remain good and satisfying. Also the statistic appears sufficient to infer estimates on the signal regions.

So, the control regions for the FS-SR2 are:

CR2: $85 < m_{\ell\ell} < 95$ GeV, $E_T^{miss} < 20$ GeV and $N(j) > 1$;

CR4: $80 < m_{\ell\ell} < 100$ GeV, $E_T^{miss} < 20$ GeV and $N(j) > 1$.

After the definition of the control regions, I can quantitatively introduce the partially data-driven technique used for the Z estimation in the signal regions. The master equation 4.9 connects the number of data events from Z in the control region ($N_{Z/\gamma^*}^{\text{data,CR}}$) to the Z contribution in the appropriate signal region $N_{Z/\gamma^*}^{\text{est,SR}}$ by means of a scale factor β_Z:

$$N_{Z/\gamma^*}^{\text{est,SR}} = \beta_Z \cdot N_{Z/\gamma^*}^{\text{data,CR}} \tag{4.9}$$

where β_Z is retrieved by the Monte Carlo simulations and is defined by

$$\beta_Z = \frac{N_{Z/\gamma^*}^{\text{MC,SR}}}{N_{Z/\gamma^*}^{\text{MC,CR}}}. \tag{4.10}$$

[6]The reason of the numeration of the control regions will be clear few lines below, after the definition of another couple of control regions.

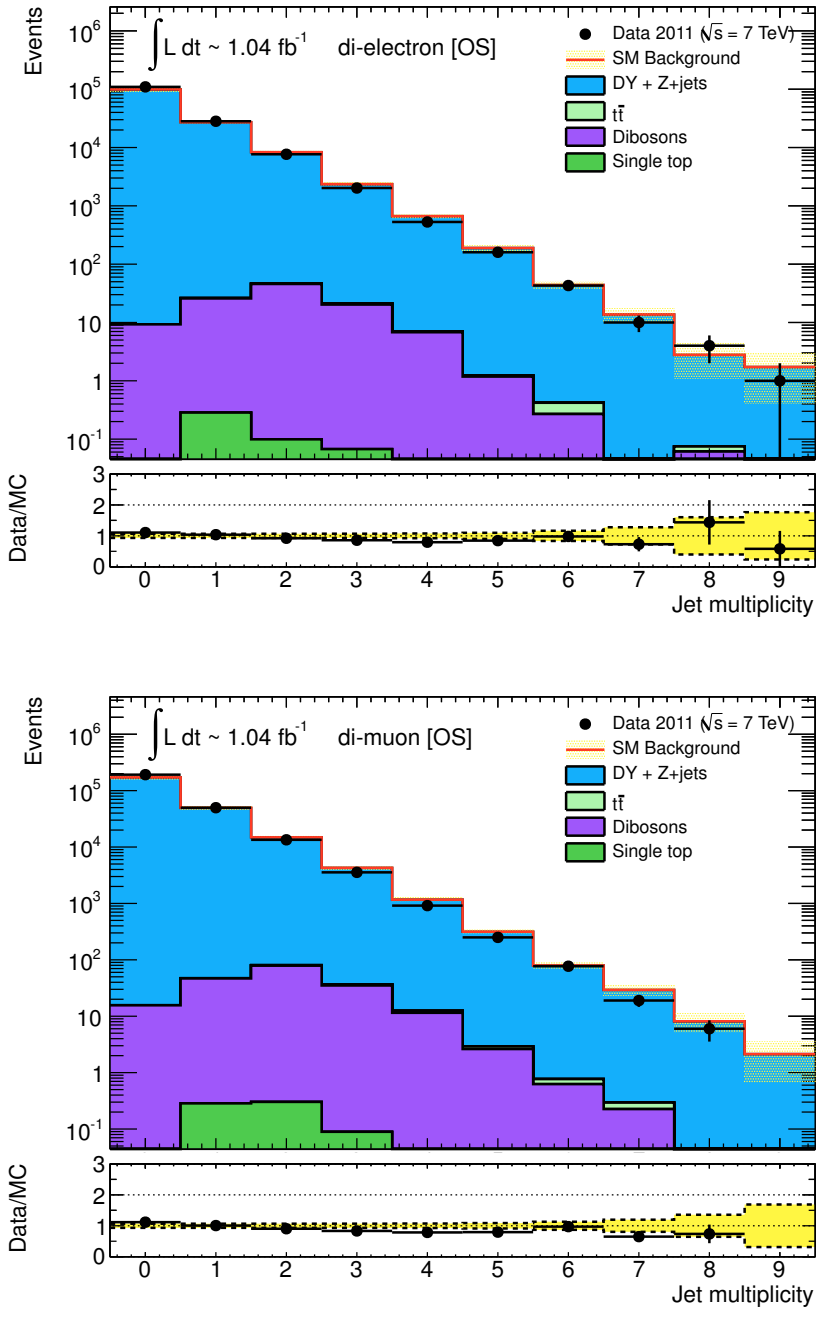

Figure 4.9: The jet multiplicity for opposite sign ee (top) and $\mu\mu$ (bottom) events with $85 < m_{\ell\ell} < 95$ GeV and $E_T^{miss} < 20$ GeV (CR1).

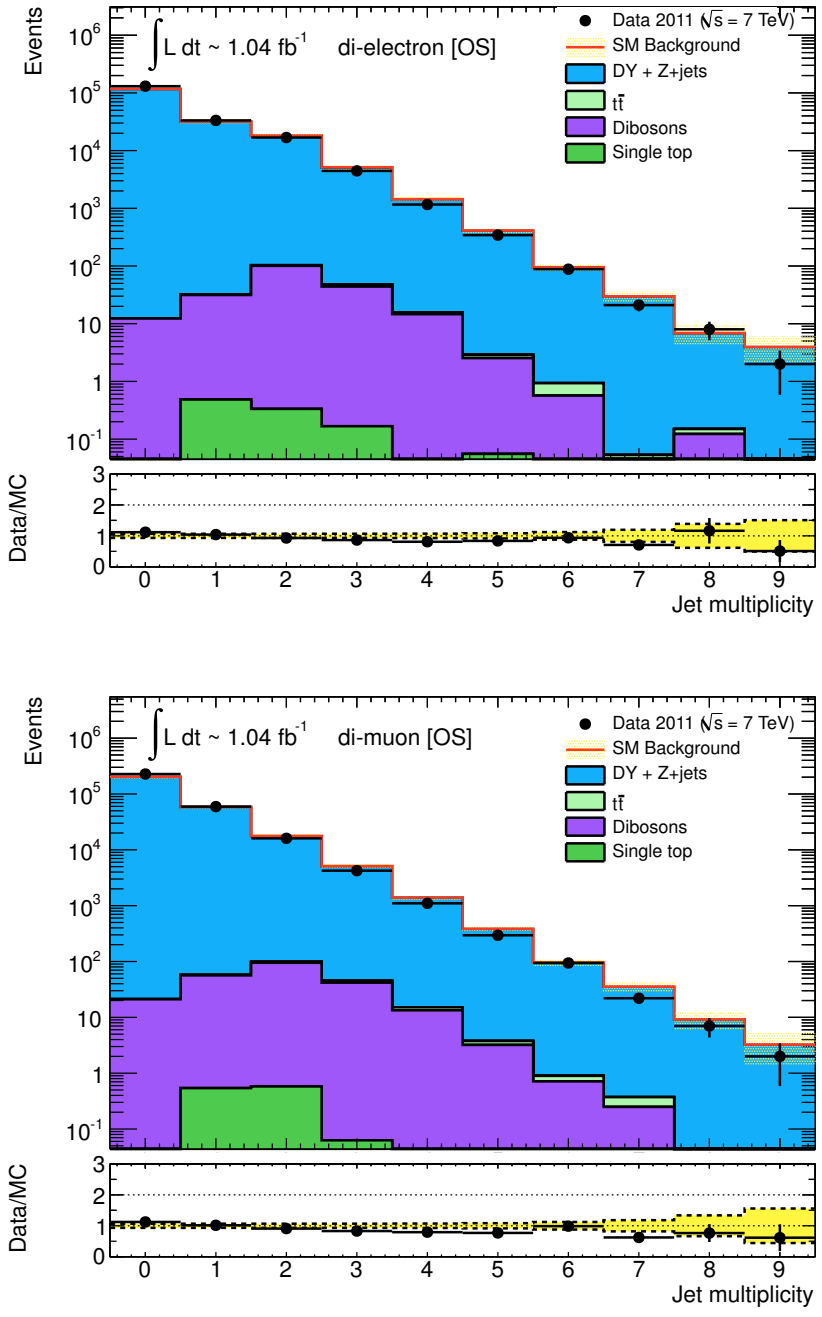

Figure 4.10: The jet multiplicity for opposite sign ee (top) and $\mu\mu$ (bottom) events with $80 < m_{\ell\ell} < 100$ GeV and $E_T^{miss} < 20$ GeV (CR3).

CR2	CR1 + Njet > 1
Total $\ell\ell$	
$N(\ell\ell)$ from Z	32104.81 $\pm$ 179.18
$N(\ell\ell)$ from other bg (no Z)	210.09 $\pm$ 14.49
$N(\ell\ell)\|_Z / N(\ell\ell)\|_{noZ}$	152.82
Purity	0.9927
CR4	CR3 + Njet > 1
Total $\ell\ell$	
$N(\ell\ell)$ from Z	38084.56 $\pm$ 195.15
$N(\ell\ell)$ from other bg (no Z)	257.58 $\pm$ 16.05
$N(\ell\ell)\|_Z / N(\ell\ell)\|_{noZ}$	147.86
Purity	0.9925

Table 4.10: Number of Z events and of other Standard Model processes in the control regions after the jet requirement. The ratio between the number of Z events and of the remaining backgrounds and the purity of the samples are indicated. The error is only statistic.

$N^{\mathrm{MC,SR}}_{Z/\gamma^*}$ and $N^{\mathrm{MC,CR}}_{Z/\gamma^*}$ are the number of OS dilepton Z/γ^* Monte Carlo (MC) events in the signal and control region respectively. The number of the Z/γ^* data events in the control region, $N^{\mathrm{data,CR}}_{Z/\gamma^*}$ is estimated by subtracting from the data events in this region the non-Z/γ^* events evaluated with the use of the Monte Carlo:

$$N^{\mathrm{data,CR}}_{Z/\gamma^*} = \left(N^{\mathrm{data}} - N^{\mathrm{MC}}_{W} - N^{\mathrm{MC}}_{t\bar{t}} - N^{\mathrm{MC}}_{\mathrm{singleTop}} - N^{\mathrm{MC}}_{\mathrm{dibosons}}\right)^{\mathrm{CR}}, \qquad (4.11)$$

Before using numerically these formulas, I draw your attention to a essential, vital point: to perform any data analysis and in particular a partial data-driven technique, we must be confident that the Monte Carlo predictions well describe the collected data. So I exploit the distributions used to evaluating and defining the various control regions for the comparison data-Monte Carlo: in both the dilepton channels ($e^{\pm}e^{\mp}$ and $\mu^{\pm}\mu^{\mp}$) the $m_{\ell\ell}$ and jet multiplicity distributions are in good and satisfactory agreement making possible the data-driven estimate. I don't show and I don't consider the $e^{\pm}\mu^{\mp}$ channel since, as already noticed at the beginning of this section, the dilepton Z decay presents almost only identical flavour lepton pairs and so the $e^{\pm}\mu^{\mp}$ contribution is very small and its statistic very poor. So we can not use this technique for this channel, but we are constrained to use only the Monte Carlo.

The Monte Carlo prediction offer also a good validation technique: the comparison between the results from data and from Monte Carlo allows to realize the robustness and goodness of this estimation method. In table 4.11 the input ingredients for the four control regions are reported; following the recipe given by the master equation 4.9, we can obtain the sought Z/γ^* es-

	CR1	CR2
$e^{\pm}e^{\mp}$		
$N^{\text{data,CR}}$	148258.00 ± 385.04	10432.00 ± 102.14
$N^{\text{MC,CR}}_{\text{non-}Z/\gamma^*}$	112.11 ± 10.59	76.66 ± 8.76
$N^{\text{data,CR}}_{Z/\gamma^*}$	148145.89 ± 385.19	10355.34 ± 102.51
$N^{\text{MC,CR}}_{Z/\gamma^*}$	137698.53 ± 371.08	11506.16 ± 107.27
$\mu^{\pm}\mu^{\mp}$		
$N^{\text{data,CR}}$	260005.00 ± 509.91	18256.00 ± 135.11
$N^{\text{MC,CR}}_{\text{non-}Z/\gamma^*}$	196.26 ± 14.01	133.42 ± 11.55
$N^{\text{data,CR}}_{Z/\gamma^*}$	259808.74 ± 510.10	18122.58 ± 135.61
$N^{\text{MC,CR}}_{Z/\gamma^*}$	241896.98 ± 491.83	20598.65 ± 143.52
	CR3	CR4
$e^{\pm}e^{\mp}$		
$N^{\text{data,CR}}$	176607.00 ± 420.25	12495.00 ± 111.78
$N^{\text{MC,CR}}_{\text{non-}Z/\gamma^*}$	138.58 ± 11.77	94.09 ± 9.70
$N^{\text{data,CR}}_{Z/\gamma^*}$	176468.42 ± 420.41	12400.91 ± 112.20
$N^{\text{MC,CR}}_{Z/\gamma^*}$	162461.92 ± 403.07	13569.97 ± 116.49
$\mu^{\pm}\mu^{\mp}$		
$N^{\text{data,CR}}$	308879.00 ± 555.77	21814.00 ± 147.70
$N^{\text{MC,CR}}_{\text{non-}Z/\gamma^*}$	242.16 ± 15.56	163.49 ± 12.79
$N^{\text{data,CR}}_{Z/\gamma^*}$	308636.84 ± 556.89	21650.51 ± 148.25
$N^{\text{MC,CR}}_{Z/\gamma^*}$	285561.28 ± 534.38	24514.59 ± 156.57

Table 4.11: The observed number of events from data in the control regions and the contribution of non $-$ Z/γ^* background sources in these regions. The MC expectations for Z/γ^* events in these control regions are also reported.

timation reported in tables 4.12, 4.13 and 4.14 for the FS-SR1, FS-SR2 and FS-SR3 respectively. It's interesting to note that the agreement between data and Monte Carlo is satisfactory: in the control regions the results differ only of few percent, while the signal region estimations are compatible in the errors. The uncertainties on the estimates are based on statistical uncertainties from the MC as well as several sources of systematic uncertainties, typical of the use of Monte Carlo (see section 4.7.1): jet energy scale (JES) fluctuations (both upward and downward), jet energy resolution fluctuations, and changes in the energy scale of the leptons. For the computation of the final systematic, we considerer the larger of the upward/downward fluctuations for jet and lepton energy scale changes. Furthermore, the comparison between the estimates from the two couples of control regions (CR1, CR2 and CR3, CR4) allows to evaluate the dependence of the results on the definition of control regions; this is another source of systematic uncertainty. However, the effect of this

variation is quite minimal: the results vary only of 1-2% and are perfectly compatible in the errors. Finally an observation on the scale factor β_Z: for the first last signal regions (FS-SR3) it is very small, whilst in the first two (FS-SR1 and FS-SR2) it is larger. It is a waited result: in fact, the high E_T^{miss} request of FS-SR3 ($E_T^{miss} > 250$ GeV) depresses the statistic of events in this region and so $N^{\mathrm{MC,SR}}$ in the β_Z definition (given by eq: 4.10).

FS-SR1		
	From CR1	From CR3
	$e^{\pm}e^{\mp}$	
β_Z	$5.48 \times 10^{-4} \pm 0.35 \times 10^{-4}$(stat.)	$4.64 \times 10^{-4} \pm 0.30 \times 10^{-4}$(stat.)
$N_{Z/\gamma^*}^{\mathrm{est,SR}}$	81.18 ±4.50(sys.) ± 9.01(stat.)	81.88 ±4.53(sys.) ± 9.05(stat.)
$N_{Z/\gamma^*}^{\mathrm{MC,SR}}$	75.40 ±6.04(stat.)	
	$\mu^{\pm}\mu^{\mp}$	
β_Z	$1.55 \times 10^{-4} \pm 0.11 \times 10^{-4}$(stat.)	$1.31 \times 10^{-4} \pm 0.09 \times 10^{-4}$(stat.)
$N_{Z/\gamma^*}^{\mathrm{est,SR}}$	40.27 ± 10.45(sys.) ± 6.35(stat.)	40.43 ± 10.48(sys.) ± 6.36(stat.)
$N_{Z/\gamma^*}^{\mathrm{MC,SR}}$	37.42 ±3.64(stat.)	

Table 4.12: The scale factors and partial data-driven predictions for the Z/γ^* contribution for OS dileptons in the flavour subtraction signal region SR1 for the ee, $\mu\mu$ channels. The comparison between the estimations from CR1 and CR3, differing for the invariant mass cut, is shown.

FS-SR2		
	From CR2	From CR4
	$e^{\pm}e^{\mp}$	
β_Z	$4.40 \times 10^{-3} \pm 0.29 \times 10^{-3}$(stat.)	$3.73 \times 10^{-3} \pm 0.24 \times 10^{-3}$(stat.)
$N_{Z/\gamma^*}^{\mathrm{est,SR}}$	45.56 ±11.74(sys.) ± 6.75(stat.)	46.26 ±11.82(sys.) ± 6.80(stat.)
$N_{Z/\gamma^*}^{\mathrm{MC,SR}}$	50.64 ±4.78(stat.)	
	$\mu^{\pm}\mu^{\mp}$	
β_Z	$2.08 \times 10^{-3} \pm 0.12 \times 10^{-3}$(stat.)	$1.74 \times 10^{-3} \pm 0.09 \times 10^{-3}$(stat.)
$N_{Z/\gamma^*}^{\mathrm{est,SR}}$	37.69 ± 4.80(sys.) ± 6.14(stat.)	37.67 ± 4.80(sys.) ± 6.14(stat.)
$N_{Z/\gamma^*}^{\mathrm{MC,SR}}$	42.77 ±4.04(stat.)	

Table 4.13: The scale factors and partial data-driven predictions for the Z/γ^* contribution for OS dileptons in the flavour subtraction signal region SR2 for the ee, $\mu\mu$ channels. The comparison between the estimations from CR2 and CR4, differing for the invariant mass cut, is shown.

In conclusion, the partial data-driven technique provides a robust estimation of the Z/γ^* contributions in the three signal regions of the flavour

FS-SR3		
	From CR1	From CR3
	$e^{\pm}e^{\mp}$	
β_Z	$7.26 \times 10^{-8} \pm 4.35 \times 10^{-8}$(stat.)	$6.16 \times 10^{-8} \pm 4.20 \times 10^{-8}$(stat.)
$N_{Z/\gamma^*}^{\text{est,SR}}$	0.01(1) $\pm$0.67(sys.) $\pm$ 0.01(stat.)	0.01(1) $\pm$0.67(sys.) $\pm$ 0.01(stat.)
$N_{Z/\gamma^*}^{\text{MC,SR}}$	0.01 $\pm$0.01(stat.)	
	$\mu^{\pm}\mu^{\mp}$	
β_Z	$3.06 \times 10^{-6} \pm 0.91 \times 10^{-6}$(stat.)	$2.59 \times 10^{-6} \pm 0.83 \times 10^{-6}$(stat.)
$N_{Z/\gamma^*}^{\text{est,SR}}$	0.79 ± 0.06(sys.) $\pm$ 0.25(stat.)	0.80 ± 0.06(sys.) $\pm$ 0.25(stat.)
$N_{Z/\gamma^*}^{\text{MC,SR}}$	0.74 $\pm$0.53(stat.)	

Table 4.14: The scale factors and partial data-driven predictions for the Z/γ^* contribution for OS dileptons in the flavour subtraction signal region SR3 for the ee, $\mu\mu$ channels. The comparison between the estimations from CR1 and CR3, differing for the invariant mass cut, is shown.

subtraction analysis in a positive and satisfactory agreement with the Monte Carlo predictions.

4.7.5 $t\bar{t}$ background estimation

The fully leptonic $t\bar{t}$ is one of the most challenging Standard Model background for a dilepton opposite sign analysis. Instead, in the flavour subtraction analysis, we have a natural cancelation of this background, due to the symmetry between identical flavour and different flavour leptons in the decay of the two top quarks. So, after the flavour subtraction, the $t\bar{t}$ is negligible and under control.

For the estimation of the $t\bar{t}$ contribution in the signal regions, the partially data-driven procedure is classical and common to the other background estimates (and already introduced in the previous sections): we select an appropriate control region with high purity and where the $t\bar{t}$ is (expected to be) dominant and from the number of observed data ($t\bar{t}$) events in this control region, scaling for a suitable scale factor, we obtain the sought estimate. Considering the distributions of the principal variables for the two lepton events selected by the analysis cuts (the E_T^{miss} in figure 4.2, the dilepton invariant mass in figure 4.3 and the jet multiplicity in figure 4.4), the more discriminating variable seems to be the missing transverse energy: for $E_T^{miss} > 80$ GeV the $t\bar{t}$ becomes the dominant background. However, a similar definition cut for the CR is not acceptable for the flavour subtraction analysis since the signal regions of this analysis (at least the first two, FS-SR1 and FS-SR2) are defined by a analogous request (see section 4.6) and so we would have control and signal regions overlapping. Just for this reason, for the flavour subtraction analysis we can not use this technique; the $t\bar{t}$ contribution to the signal regions

is estimated only with the use of the Monte Carlo predictions. Only for the third signal region FS-SR3 (with the request of high missing transverse energy: $E_T^{miss} > 250$ GeV), the signal and control regions are not overlapping and so we have a partially data driven estimation. Therefore, in this section, I'll describe only briefly and qualitatively the base of one of the two "top-tagging" techniques used to the estimation, that using the cotransverse mass variable, m_{CT} [68] already exploited in the published 2010 analysis, Refs. [69] and [70].

I introduce the control region for the third signal region of flavour subtraction analysis FS-SR3:

- 60 GeV $< E_T^{miss} <$ 100 GeV for $e\mu$ pairs and 80 GeV $< E_T^{miss} <$ 100 GeV for identical flavour lepton pairs.
- at least two jets must satisfy the conditions of the cotransverse mass top tagger algorithm.

The top tagger algorithm is based on the cotransverse mass variable [68] and is able to select events with a kinematics compatible with that of $t\bar{t}$ event. The cotransverse mass can be defined for heavy states δ produced in pairs, each decaying into an invisible α and visible χ_i particles in the following way:

$$m_{CT}^2(\chi_1, \chi_2) = [E_T(\chi_1) + E_T(\chi_2)]^2 - [\mathbf{p_T}(\chi_1) - \mathbf{p_T}(\chi_2)]^2 \tag{4.12}$$

The $t\bar{t}$ event fulfils perfectly these requirements, since the final products of a top quark (δ) leptonic decay are one neutrino (α), one charged lepton and one jet (therefore χ can be a lepton, a jet, or a lepton-jet combination) and so it is possible use and compute this variable. Furthermore, the $t\bar{t}$ event presents another important and interesting feature: the two leptonic decay chains, starting from the top and anti-top quarks, have similar composition and characteristics; in particular the visible products χ_1 and χ_2 have the same mass. So, we have an important and crucial consequence: m_{CT} possesses an endpoint. Setting $m(\chi_1) = m(\chi_2) \equiv m(\chi)$, we can write it as:

$$m_{CT}\left[m^2(\chi)\right] < m_{CT}^{\max}\left[m^2(\chi)\right] = \frac{m^2(\chi)}{m(\delta)} + \frac{m^2(\delta) - m^2(\alpha)}{m(\delta)} \tag{4.13}$$

This is foundation of this algorithm: for a $t\bar{t}$ event we can construct three different cotransverse mass combinations ($m_{CT}(\ell\ell)$, $m_{CT}(jj)$, $m_{CT}(jl, jl)$) and each one satisfies the relative inequality of Eq. 4.13 obtained substituting for (δ, α) respectively (W, ν), (t, W), and (t, ν). This observation provides us the sought criterion and the general idea for selecting the $t\bar{t}$ events: an event is tagged as top event only if the endpoint given by the Eq. 4.13 is fulfilled for the three different cotransverse mass combinations. This algorithm selects $t\bar{t}$ events with an efficiency of about 87% while rejecting about 73% of the other Standard Model processes.

After the ticklish definition of the control region, we can estimate the $t\bar{t}$ contributions in the signal region FS-SR3 using the master equation

$$(N_{t\bar{t}})_{SR} = \beta_{t\bar{t}} \cdot (N_{t\bar{t},data}^{tag})_{CR} \tag{4.14}$$

where the scale factor $\beta_{t\bar{t}}$, used to extrapolate from the control region to the signal region, is retrieved by the Monte Carlo predictions and is given by

$$\beta_{t\bar{t}} = \frac{(N_{t\bar{t},MC})_{SR}}{(N^{tag}_{t\bar{t},MC})_{CR}}$$

where $N_{t\bar{t},MC})_{SR}$ ($(N^{tag}_{t\bar{t},MC})_{CR}$) is the number of $t\bar{t}$ events expected by Monte Carlo in the signal (control) region. $(N^{tag}_{t\bar{t},data})_{CR}$ is the number of observed $t\bar{t}$ in data in the control region and is obtained by subtracting the predicted number of non-$t\bar{t}$ events in the control region ($(N_{non-tt,MC})_{CR}$) from the total number of observed events in the control region $(N_{data})_{CR}$

$$(N^{tag}_{t\bar{t},data})_{CR} = \left((N^{tag}_{t\bar{t},data})_{CR} - (N^{tag}_{non-tt,MC})_{CR}\right)$$

For giving a useful estimation we must also give the uncertainty associated to it. For the data observation the uncertainty is statistical, while for the terms provided by the Monte Carlo predictions, in addition to the statistical uncertainty, we have also the classical sources of systematic error already presented in section 4.7.1: luminosity, cross section, limited Monte Carlo statistics, jet energy scale (JES) and resolution (JER). Furthermore, for the $t\bar{t}$ background, we have different Monte Carlo samples and so it is possible to study and considerer the systematical uncertainty associated to the choice of Monte Carlo generator (evaluated comparing the predictions of MC@NLO, Powheg, and Alpgen) and the uncertainty associated to ISR/FSR (evaluated considering the six AcerMC samples with varying ISR/FSR settings, and taking half of the difference between the minimum and maximum value as systematics). A similar study performed by myself is presented in section 4.9.2 for the flavour subtraction analysis. As we can see in table 4.15, just the uncertainties due to the generator choice are those most important and with the main clout.

The Monte Carlo predictions for the $t\bar{t}$ background in the three signal regions of flavour subtraction analysis are shown in Tables 4.16; for the third signal region I report also the data-driven estimation obtained in [59]. The Monte Carlo offers a good possibility validation. The agreement is very satisfactory.

Signal region Control region	FS-SR3 CR
Statistical (CR, observed)	3.8%
Statistical (CR, expected)	3.8%
Statistical ($t\bar{t}$ MC)	6.0%
Statistical (non-$t\bar{t}$ MC)	0.4%
JES ($t\bar{t}$ MC)	10.6%
JES (non-$t\bar{t}$ MC)	3.4%
JER ($t\bar{t}$ MC)	0.6%
JER (non-$t\bar{t}$ MC)	0.9%
luminosity (non-$t\bar{t}$ MC)	0.7%
cross sections (non-$t\bar{t}$ MC)	1.6%
CR fake uncertainty	0.7%
generator	15.6%
ISR/FSR	20.0%
total (expected)	26.7%
total (observed)	26.7%

Table 4.15: Uncertainties on the estimate of the $t\bar{t}$ background in the third signal region of the flavour subtraction analysis, the only one data-driven estimated [59].

Signal region	ee
FS-SR1 MC	199.47 ± 10.55 (syst.) ± 8.37 (stat.)
FS-SR2 MC	215.61 ± 12.78 (syst.) ± 8.53 (stat.)
FS-SR3 MC	1.98 ± 1.22 (syst.) ± 0.93 (stat.)
FS-SR3 DD	1.84 ± 0.49 (syst.) ± 0.07 (stat.)
	$\mu\mu$
FS-SR1 MC	410.72 ± 21.09 (syst.) ± 11.20 (stat.)
FS-SR2 MC	438.30 ± 27.60 (syst.) ± 11.71 (stat.)
FS-SR3 MC	3.20 ± 1.54 (syst.) ± 1.16 (stat.)
FS-SR3 DD	3.34 ± 0.88 (syst.) ± 0.13 (stat.)
	eμ
FS-SR1 MC	580.50 ± 24.35 (syst.) ± 14.10 (stat.)
FS-SR2 MC	629.00 ± 32.45 (syst.) ± 14.70 (stat.)
FS-SR3 MC	5.23 ± 1.89 (syst.) ± 1.35 (stat.)
FS-SR3 DD	5.09 ± 1.35 (syst.) ± 0.19 (stat.)

Table 4.16: Monte Carlo predictions for the $t\bar{t}$ background in the three opposite sign signal regions of the flavour subtraction analysis. For the third signal region FS-SR3 the data-driven estimations are reported.

4.7.6 Results

I summarize the results illustrated in the previous sections in Table 4.17, where the total predicted numbers of background events (Standard Model only) in each opposite-sign channel, in the three flavour-subtraction signal regions, are given. In the total error the systematic and statistical errors have been added in quadrature. For a clearer and more immediate comparison I report both the only Monte Carlo estimates and the partially data-driven ones. The single top and the diboson backgrounds are estimated only with the Monte Carlo, while the $t\bar{t}$ contribution is evaluated by data-driven technique only for FS-SR3. Also the Z contributions in the $e^{\pm}\mu^{\mp}$ channel are obtained from the Monte Carlo. The cosmics are negligible as seen in section 4.7.2. So, the main differences from Monte Carlo and data driven predictions derive from the Z and for FS-SR3 also from $t\bar{t}$: the agreement is very good.

	$e^{\pm}e^{\mp}$	$e^{\pm}\mu^{\mp}$	$\mu^{\pm}\mu^{\mp}$
Exp.MC SR1	306.85±15.78(sys.)±10.63(stat.)	727.23±26.65(sys.)±16.23(stat.)	538.19±27.37(sys.)±13.57(stat.)
Pred. SR1	312.98±15.14(sys.)±12.57(stat.)	727.23±26.65(sys.)±16.23(stat.)	541.16±28.72(sys.)±14.53(stat.)
Data SR1	344	750	551
Exp.MC SR2	285.81±24.59(sys.)±9.99(stat.)	733.23±37.00(sys.)±16.50(stat.)	543.93±34.04(sys.)±13.78(stat.)
Pred. SR2	285.62±18.83(sys.)±11.08(stat.)	733.23±37.00(sys.)±16.50(stat.)	537.34±32.40(sys.)±14.54(stat.)
Data SR2	336	741	567
Exp.MC SR3	2.67±1.27(sys.)±0.97(stat.)	7.90±2.21(sys.)±1.80(stat.)	5.25±1.58(sys.)±1.32(stat.)
Pred. SR3	2.53±0.90(sys.)±0.29(stat.)	7.76±1.77(sys.)±1.38(stat.)	5.45±1.15(sys.)±0.37(stat.)
Data SR3	2	8	3

Table 4.17: Expected, predicted and observed numbers of events in each flavour-subtraction signal region. In SR1 and SR2 the predicted background estimates in each channel include the Monte Carlo predictions for $t\bar{t}$, dibosons and single top, but the data-driven predictions for the fake background and Z+jets background. In SR3 all but the diboson and single top contributions are data-driven.

4.8 Estimate of the identical flavour dilepton excess

In the previous section, I introduced the estimation (partially data-driven) of the contribution of Standard Model processes to the dilepton opposite sign events in the three channels ($e^{\pm}e^{\mp}$, $e^{\pm}\mu^{\mp}$ and $\mu^{\pm}\mu^{\mp}$) in the signal regions defined for the flavour subtraction. These estimates are necessary in order to interpret the observation of dilepton events from the data. Now, we are ready to use these numbers of events in the flavour subtraction analysis.

The excess in data of identical flavour events over those of same flavour can be quantified using the variable $\mathcal{S}$, already introduced in Ref. [70] for the 2010 analysis. This quantity, given in Equation 4.15, computes the excess of identical flavour events by taking into account the different reconstruction (ϵ_e and ϵ_μ) and trigger efficiencies (τ_e and τ_μ) for electrons and muons.

$$\mathcal{S} = \frac{N(e^{\pm}e^{\mp})}{\beta(1-(1-\tau_e)^2)} - \frac{N(e^{\pm}\mu^{\mp})}{1-(1-\tau_e)(1-\tau_\mu)} + \frac{\beta N(\mu^{\pm}\mu^{\mp})}{(1-(1-\tau_\mu)^2)} \tag{4.15}$$

β is defined as the ratio between the electron and muon reconstruction efficiencies ϵ_e/ϵ_μ but takes into account and includes also the difference in the detector acceptance. The trigger and reconstruction efficiencies have to be determined for data and Monte Carlo samples separately. In the next sections, I will present their determination.

4.9 Electron and muon efficiencies

4.9.1 Trigger efficiencies τ_e and τ_μ

As already seen, we have two separate data streams for electrons (Egamma stream) and muons (Muon stream): in the Egamma stream the trigger request involves the electron trigger whilst in the Muon stream the muon trigger. In consequence we can use the Egamma stream as unbiased muon sample to determine the muon trigger efficiency in data and the muon stream for electron trigger efficiency. The trigger efficiencies are determined as the ratio of events selected by the tight event selection and appropriate trigger fired over all events after tight event selection. The trigger efficiencies in Monte Carlo samples are defined as the number of events with selected lepton and appropriate trigger divided by all events containing a selected lepton. The trigger efficiencies obtained with this procedure are reported in Table 4.18.

	τ_e	τ_μ
Data	0.964 ± 0.001	0.819 ± 0.006 B: 0.731 ± 0.009 EC: 0.875 ± 0.008
Monte Carlo	0.987 ± 0.000(1)	0.800 ± 0.000(2) B: 0.709 ± 0.001 EC: 0.866 ± 0.000

Table 4.18: Trigger efficiencies in data and Monte Carlo. For the muon trigger efficiencies, the barrel (B) and endcap (EC) values are reported.

4.9.2 Estimation of β

To calculate the identical flavour excess, we must take into account the different detector acceptance and reconstruction efficiency between electrons and muons in order to give the appropriate weight at the numbers of dilepton events present in $\mathcal{S}$ (Eq. 4.15) and so correct the flavour subtraction. These efficiencies appear only in the ratio β in $\mathcal{S}$. So, there are two methods to obtain β: the first exploits the truth information present in the Monte Carlo samples to derive the electron and the muon efficiencies separately, while the second gives only the ratio β with a data driven technique. Making use of the Monte Carlo, it is possible study some sources of systematic uncertainty.

Monte Carlo estimation

In a Monte Carlo sample, we can considerer the truth information that allows the knowledge and description of the entire chain of decay and of the kinematic properties (four-vectors) of the particles produced directly by the Monte Carlo generator (before the simulation of the detector and the reconstruction). Often, these original particles are labeled as "true". Exploiting these information, we can obtain the reconstruction efficiency as the ratio of reconstructed and identified leptons matched to a true lepton over the sum of all true leptons. As true leptons only those in the detector acceptance are taken into account: so the considered true leptons are the true electrons with $p_T > 20$ GeV and $|\eta| < 2.47$ and the true muons with $p_T > 10$ GeV and $|\eta| < 2.4$. The electron efficiencies only differ within few percents among the various Standard Model backgrounds, whilst the muon efficiencies show larger differences, as we can see in Fig. 4.11. These variations for the muons (and not for the electrons) can be explained by the overlap removal requested among leptons and jets in order to guarantee the lepton isolation: in case of electron jet overlap removal in a first step jets in a cone of $\Delta R < 0.2$ around an electron are removed and in a second step electrons in a cone around jets $\Delta R < 0.4$ are rejected, while in the muon jet overlap removal only the second cut is applied. Therefore, more muon candidates than electron candidates are rejected by the overlap removal in busy events. So, we observe the decrease of the muon efficiency in events with more activity in the detector like $t\bar{t}$, whilst the electron one remain

almost constant.

These variations in the muon efficiencies yield obviously deviations in β. The differences among the β values obtained in various Standard Model processes are taken into account as source of systematic uncertainty when applying the flavour subtraction. In Table 4.19 the values of the lepton reconstruction efficiencies and beta for several SM processes are shown. From this method, we obtain an average value for β of 0.764 ± 0.008.

process	ϵ_e	ϵ_μ	β
W+Jets	0.640 ± 0.000	0.897 ± 0.000	0.714 ± 0.001
diBoson	0.675 ± 0.006	0.872 ± 0.003	0.774 ± 0.007
$t\bar{t}$	0.683 ± 0.002	0.818 ± 0.002	0.835 ± 0.003
Z+Jets	0.650 ± 0.000	0.889 ± 0.000	0.731 ± 0.000

Table 4.19: Reconstruction and identification efficiencies and ratio β for several SM processes.

I exploit the Monte Carlo also for performing a study on the systematic uncertainties on the estimation of β. I'd like to determinate the clout and the importance of three different sources of systematic errors:

- the physics process;
- the Monte Carlo generator;
- the event radiation.

The value of β depends on the Standard Model process we use to calculate it. We must take into account this difference. In table 4.19 the results for several processes are reported. As already noticed, the $t\bar{t}$ has the highest value since it presents the lowest muon reconstruction efficiency due to the lepton-jet overlap removal. The other Monte Carlo backgrounds show similar behaviour and values. Furthermore, including the $t\bar{t}$ process, the uncertainty increases: we can introduce a systematic error due to the physics process of 0.061.

The second source is associated to the choice of Monte Carlo generator. For evaluating this uncertainty, I consider the $t\bar{t}$ sample and compare the results obtained with three different generators: MC@NLO, PowHeg and Alpgen. In table 4.20 the electron and muon reconstruction efficiencies and their ratio are reported. It's interesting to notice that MC@NLO, Poweg and Alpgen are all supported by Jimmy for the parton shower generation; this is a reason that explains why they present similar results in the lepton reconstruction efficiencies and in consequence in the β ratio. In particular, their β values are compatible. In figure 4.12 the efficiency and β distributions are reported. As expected after the reading of the numerical results, the distributions show similar behaviours and are compatible. However, while the MC@NLO and the PowHeg show a similar distribution, the Alpgen sample is characterized by broader fluctuations for high p_T leptons. Using as default the MC@NLO

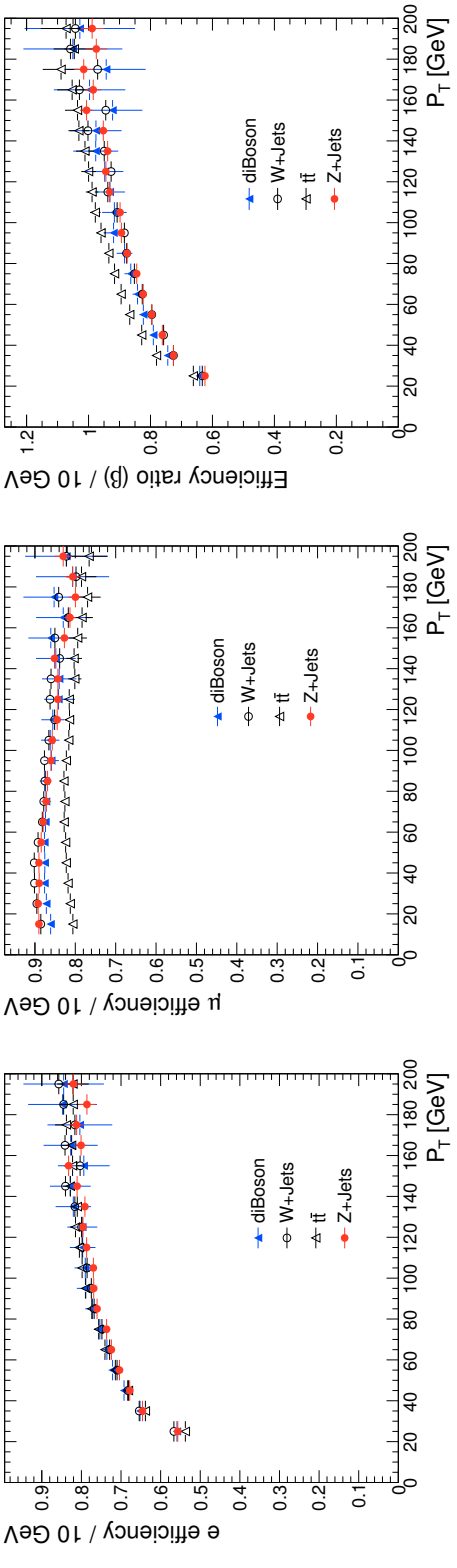

(a) (b) (c)

Figure 4.11: Reconstruction and identification efficiencies for electrons(a) and muons(b) and the ratio β(c) for several MC processes.

sample, the systematic uncertainty associated to the choice of generators can be estimated in 0.007.

$t\bar{t}$ MC	ϵ_e	ϵ_μ	β
MC@NLO	0.683 ± 0.002	0.818 ± 0.002	0.835 ± 0.003
PowHeg	0.680 ± 0.002	0.807 ± 0.001	0.842 ± 0.002
Alpgen	0.693 ± 0.000	0.825 ± 0.003	0.840 ± 0.003

Table 4.20: Reconstruction and identification efficiencies and ratio β for the $t\bar{t}$ process, simulated with different Monte Carlo (MC) generators.

The third component of the systematic uncertainty I consider is associated to the initial state radiation (ISR) and the final state radiation (FSR). Six $t\bar{t}$ Monte Carlo samples are generated with AcerMC varying up and down the parameters controlling the amount of ISR and FSR both separately and simultaneously in order to study their systematic effect (in the Appendix you can find the datasets). The lepton reconstruction efficiencies and β calculated for these samples are reported in table 4.21. All the β values obtained for the AcerMC samples are higher than that retrieved for the MC@NLO sample, considered in my estimation as nominal value and reference sample. So the systematics is computed as

$$\Delta\beta_{syst,IFSR} = 0.5 * \frac{\beta_{max} - \beta_{min}}{\beta_{nominal}}$$

where β_{max} and β_{min} are respectively the maximum and minimum β value among those obtained for the six AcerMC samples and $\beta_{nominal}$ is the MC@NLO one. In this way, I can estimate the systematic uncertainty due to the ISR and FSR as 0.014.

$t\bar{t}$ MC	ϵ_e	ϵ_μ	β
MC@NLO	0.683 ± 0.002	0.818 ± 0.002	0.835 ± 0.003
ISR down	0.588 ± 0.001	0.688 ± 0.001	0.855 ± 0.001
ISR up	0.583 ± 0.001	0.671 ± 0.001	0.870 ± 0.002
FSR down	0.611 ± 0.001	0.712 ± 0.001	0.857 ± 0.002
FSR up	0.554 ± 0.001	0.630 ± 0.001	0.879 ± 0.001
ISR down FSR down	0.619 ± 0.001	0.721 ± 0.001	0.858 ± 0.002
ISR up FSR up	0.548 ± 0.001	0.624 ± 0.001	0.878 ± 0.002

Table 4.21: Reconstruction and identification efficiencies and ratio β for the $t\bar{t}$ process, generated by AcerMC varying the parameters controlling the amount of ISR and FSR.

Adding in quadrature the different systematic contributions, I can evaluate the total systematic uncertainty: $\Delta\beta_{syst} = 0.063$.

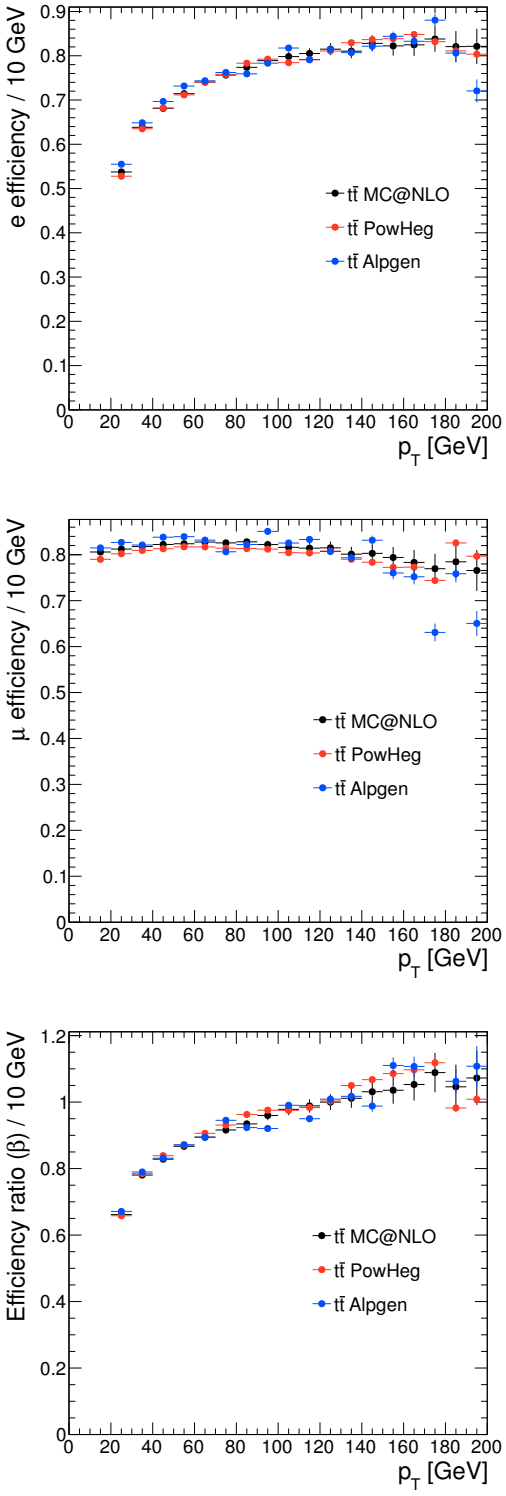

Figure 4.12: Reconstruction and identification efficiencies for electrons (top) and muons (center) and their ratio β (bottom) for $t\bar{t}$ events simulated with different MC generators.

Data driven estimation

The second method allows to obtain a data driven estimation of β. In this case, we can't retrieve the separate values of the electron and the muon reconstruction efficiencies. (However, as already noticed, in the expression of $\mathcal{S}$ (equation 4.15), they appear only in the ratio β.) We exploit the process $Z \to \ell^-\ell^+$; according to the Standard Model, the boson Z decays with equal branching ratio in e^+e^- and in $\mu^+\mu^-$. This means that we should count the same number of e^+e^- events and $\mu^+\mu^-$ events produced by the Z decay. The eventual difference is caused by different trigger and reconstruction efficiencies between electrons and muons.

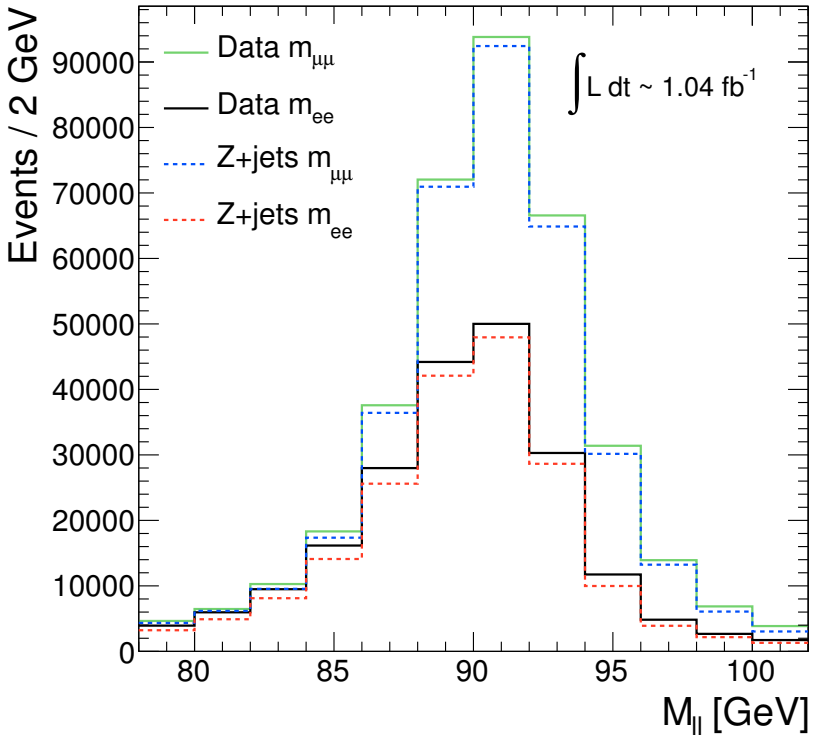

Figure 4.13: Invariant mass distributions for opposite sign dilepton for events (e^+e^- and $\mu^+\mu^-$) with $E_T^{miss} < 40$ GeV. The window under the Z mass peak is shown. With continue lines I report the observed data distributions, whilst with dashed lines the similar ones obtained from the analysis of the Z+jets Monte Carlo datasets.

So, the first step is to define an appropriate Z control region with enhanced Z decays. On top of the dilepton event selection we request:

- $E_T^{miss} < 40$ GeV
- 85 GeV $< m_{\ell\ell} <$ 95 GeV (window around the Z peak)

In figure 4.13 the invariant mass distributions $m_{\ell\ell}$ for e^+e^- and $\mu^+\mu^-$ pairs are shown for events with $E_T^{miss} < 40$ GeV. The comparison between the data observations (continue lines) and the similar distributions obtained from the Z Monte Carlo (dashed lines) highlights the purity of the selected Z control region. Furthermore, it's possible to see the effect of the different trigger and reconstruction efficiencies between electrons and muons that lead to a higher $m_{\mu^+\mu^-}$ peak than the $m_{e^+e^-}$ one. It's an interesting and partially surprising result: in fact, as seen in section 4.9.1, the electron trigger efficiency τ_e is higher than the muon one τ_μ and so we could expect an opposite result with respect to that shown in figure 4.13. In consequence, the observed result can be only explained and caused by a greater muon reconstruction efficiency than the electron one. This supposition was already been confirmed in the previous section with the Monte Carlo study of the separate lepton reconstruction efficiencies. With this data-driven study, this difference can be appreciated through the value of β that therefore will be less than 1. So, β can be estimated by dividing the number of e^+e^- by the number of $\mu^+\mu^-$ events and correcting this ratio for the different trigger efficiencies (τ_e and τ_μ) which have been determined before (equation 4.16).

$$\beta = \sqrt{\frac{N_{ee}}{N_{\mu\mu}} \cdot \frac{1-(1-\tau_\mu)^2}{1-(1-\tau_e)^2}} \tag{4.16}$$

CR: 85 GeV $< m_{\ell\ell} <$ 95 GeV && $E_T^{miss} < 40$ GeV			
Sample	N_{ee}	$N_{\mu\mu}$	β
Data 2011	168977	299513	0.739 ± 0.002
MC Z + jets	161678.22 ± 402.09	286540.22 ± 535.29	
MC diBoson	174.59 ± 13.21	290.36 ± 17.04	
MC Total	161865.58 ± 402.33	286851.02 ± 535.58	0.736 ± 0.002

Table 4.22: Number of e^+e^-, $\mu^+\mu^-$ events in the Z control region and β value (ratio between the identification and reconstruction efficiencies for electrons and muons ϵ_e/ϵ_μ) in data and Monte Carlo obtained with a data driven technique. For the Monte Carlo samples, the two backgrounds (Z+jets and diboson) with more events in the Z control region are reported in detail with statistic error.

In table 4.22 the value of β obtained applying this method on the 2011 data and at the Monte Carlo samples are reported. The Monte Carlo can be used as validation tool for checking the data-driven result: the values are in good and satisfactory agreement, as already verified graphically in figure 4.13. As expected, the β value is less than 1: the muon signature is purer and cleaner than the electron one and so the muon reconstruction efficiency is greater.

It's interesting evaluate the robustness of this estimation and its dependence on the Z control region. So, I try to modify separately both the defini-

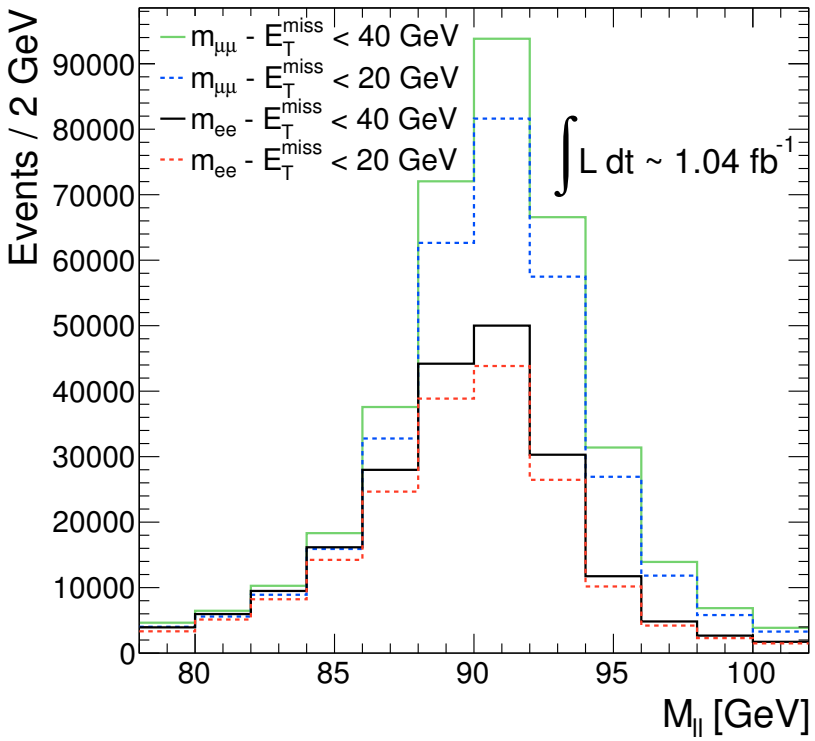

Figure 4.14: Invariant mass distributions for opposite sign dilepton for events (e^+e^- and $\mu^+\mu^-$) with $E_T^{miss} < 40$ GeV (continue lines) and with $E_T^{miss} < 20$ GeV (dashed lines). The window under the Z mass peak is shown.

tion cuts for studying the systematic effects; I take in consideration a second control region (CR2) with an tighter E_T^{miss} cut and the same invariant mass cut:

- $E_T^{miss} < 20$ GeV
- 85 GeV $< m_{\ell\ell} <$ 95 GeV

and a third control region (CR3) with a broader mass window under the Z peak, defined as:

- $E_T^{miss} < 20$ GeV
- 80 GeV $< m_{\ell\ell} <$ 100 GeV

In figure 4.14 I show the dilepton invariant mass distributions for e^+e^- and $\mu^+\mu^-$ in the different control regions; in particular with dashed lines I represent the events with $E_T^{miss} < 20$ GeV (CR2 and CR3), while with continue lines the events with $E_T^{miss} < 40$ GeV (CR1). Using the data-driven technique expressed by the equation 4.16, from the observed number of dilepton opposite sign identical flavour data events in the control regions I can retrieve the β

value. The results for these new control regions are reported in table 4.23 for the data and for the Monte Carlo: the β value from the Monte Carlo is compatible with the observed one in all the control regions. Moreover, also the comparison of β value among the three different control regions is positive and the variation very small. In particular the variation of the invariant mass window width produces minimal effect, whilst a little greater fluctuations are caused by the variation of the E_T^{miss} cut. So we can evaluate the systematic uncertainty due to the definition cut of the Z control region in 0.003.

CR2: 85 GeV $< m_{\ell\ell} <$ 95 GeV && $E_T^{miss} <$ 20 GeV			
Sample	N_{ee}	$N_{\mu\mu}$	β
Data 2011	148258	260005	0.743 ± 0.002
MC Total	137810.64 ± 371.23	242093.24 ± 492.03	0.739 ± 0.002
CR3: 80 GeV $< m_{\ell\ell} <$ 100 GeV && $E_T^{miss} <$ 20 GeV			
Data 2011	176607	308879	0.744 ± 0.002
MC Total	162600.50 ± 403.24	285803.44 ± 534.61	0.739 ± 0.002

Table 4.23: Number of e^+e^-, $\mu^+\mu^-$ events in the second (CR2) and third (CR3) Z control region and β value (ratio between the identification and reconstruction efficiencies for electrons and muons ϵ_e/ϵ_μ) in data and Monte Carlo obtained with a data driven technique.

The difference in β for the two methods (Monte Carlo and data-driven) can be taken as systematic uncertainty. This uncertainty is $\Delta\beta = 0.02$.

4.10 Results

In the Tables 4.24, 4.25 and 4.26 the observations in each of the three dilepton channels ($e^\pm e^\mp$, $e^\pm\mu^\mp$ and $\mu^\pm\mu^\mp$) in the data and the Monte Carlo predictions (with appropriate systematic and statistic uncertainties) are reported for the three signal regions of the flavour subtraction analysis. I will now exploit these numbers and the just derived τ_e, τ_μ and β to calculate the observed $\mathcal{S}$ in data, $\mathcal{S}_{obs}$; the Monte Carlo predictions and the data-driven estimations (see Table 4.17) are used separately to determine the expected mean value of $\mathcal{S}$ from Standard Model events alone ($\bar{\mathcal{S}}_b$).

4.10.1 Observation of $\mathcal{S}$ in data

In data we observe 344, 750 and 551 events in the $e^\pm e^\mp$, $e^\pm\mu^\mp$ and $\mu^\pm\mu^\mp$ channels in FS-SR1. In FS-SR2 we observe 336, 741 and 567 events respectively. As expected, the tight E_T^{miss} cut ($E_T^{miss} > 250$ GeV) that defines the FS-SR3 suppresses almost all the events and so we observe only 2, 8 and 3 events respectively. At this point, we use the definition 4.15 to calculate the excess of

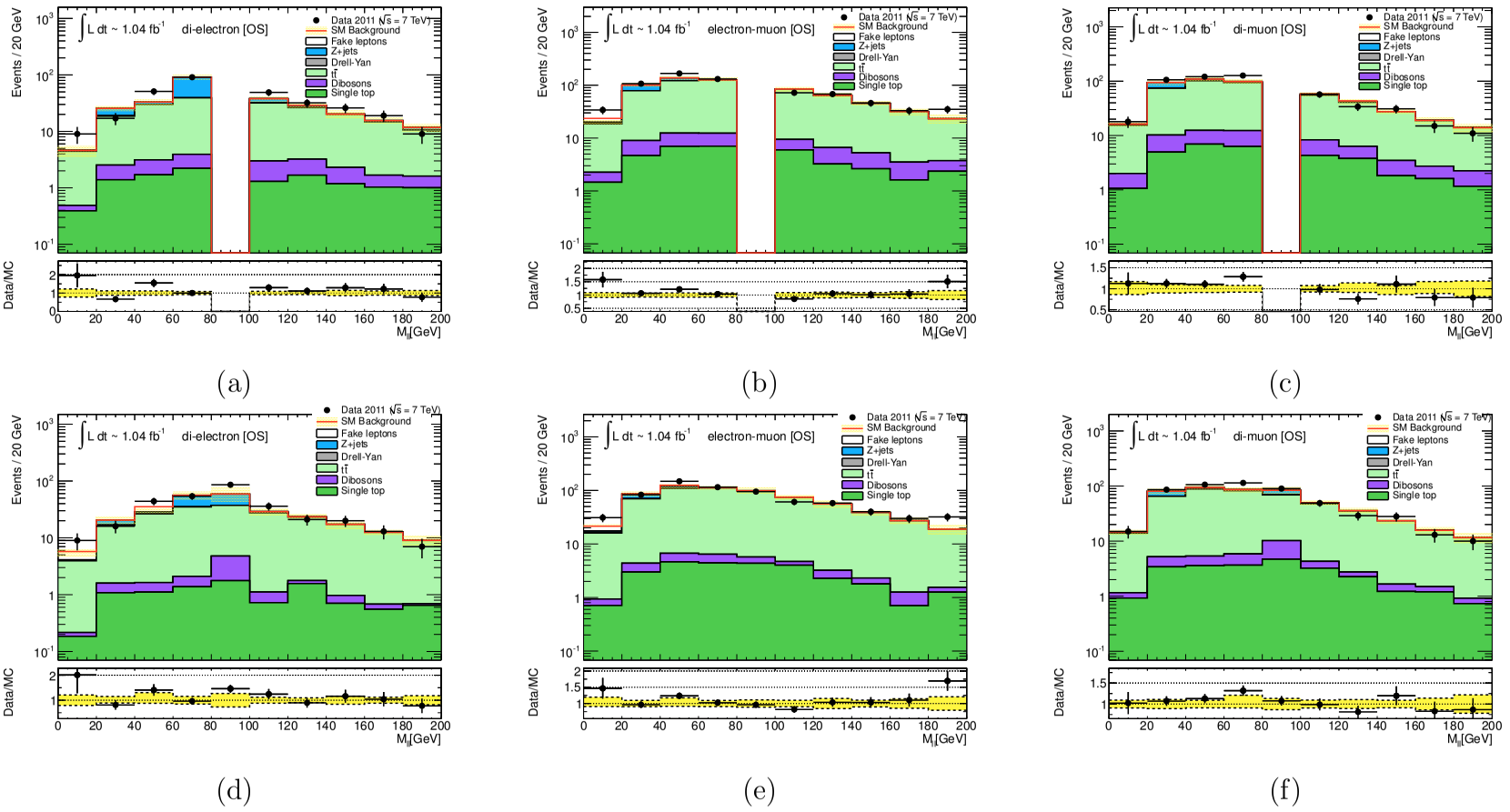

Figure 4.15: Data and Monte Carlo $m_{\ell\ell}$ distributions for the three dilepton channels ($e^{\pm}e^{\mp}$, $e^{\pm}\mu^{\mp}$ and $\mu^{\pm}\mu^{\mp}$) respectively in FS-SR1 (a-c) and FS-SR2 (d-f).

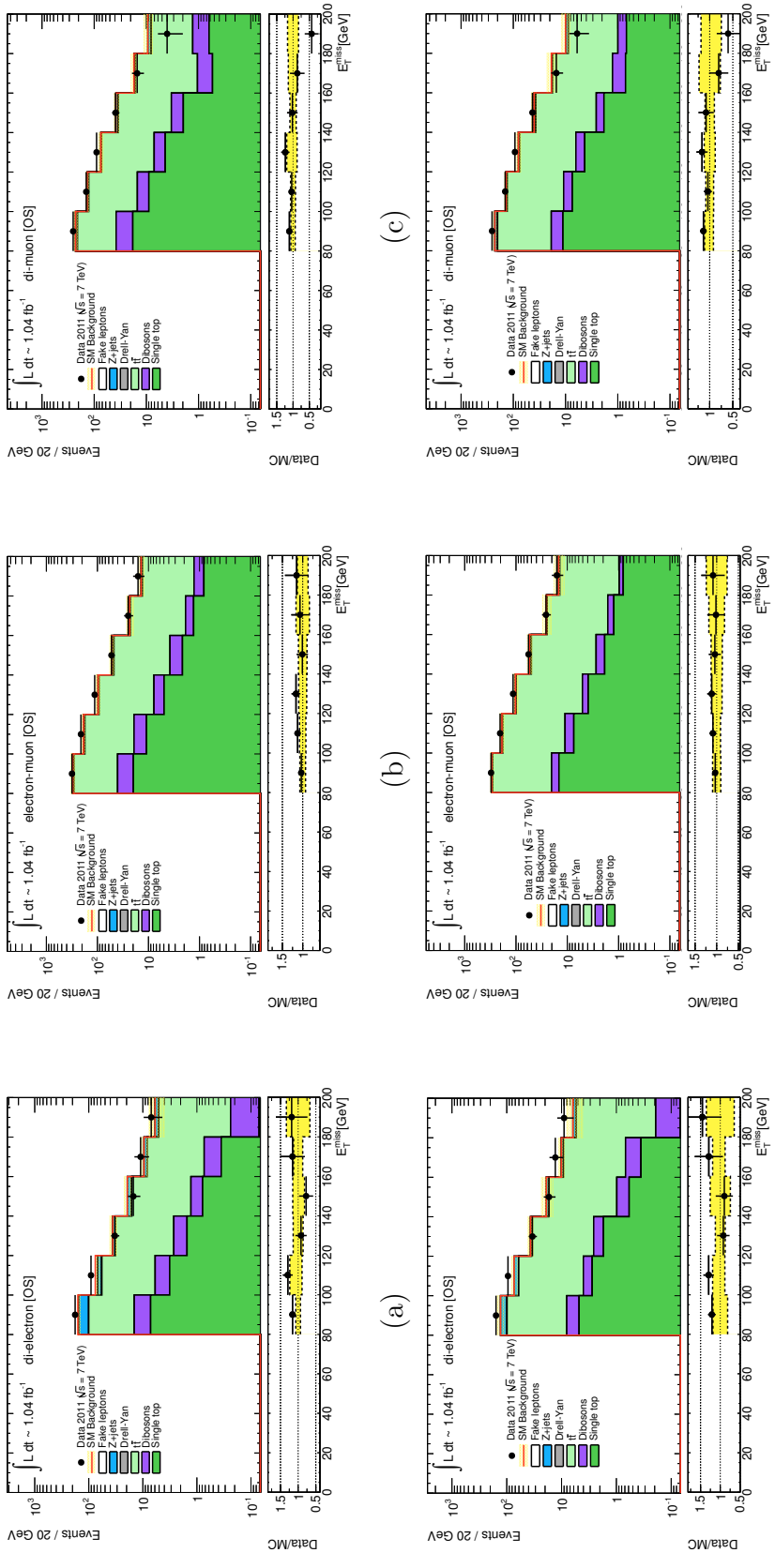

Figure 4.16: Data and Monte Carlo E_T^{miss} distributions for the three dilepton channels ($e^{\pm}e^{\mp}$, $e^{\pm}\mu^{\mp}$ and $\mu^{\pm}\mu^{\mp}$) respectively in FS-SR1 (a-c) and FS-SR2 (d-f).

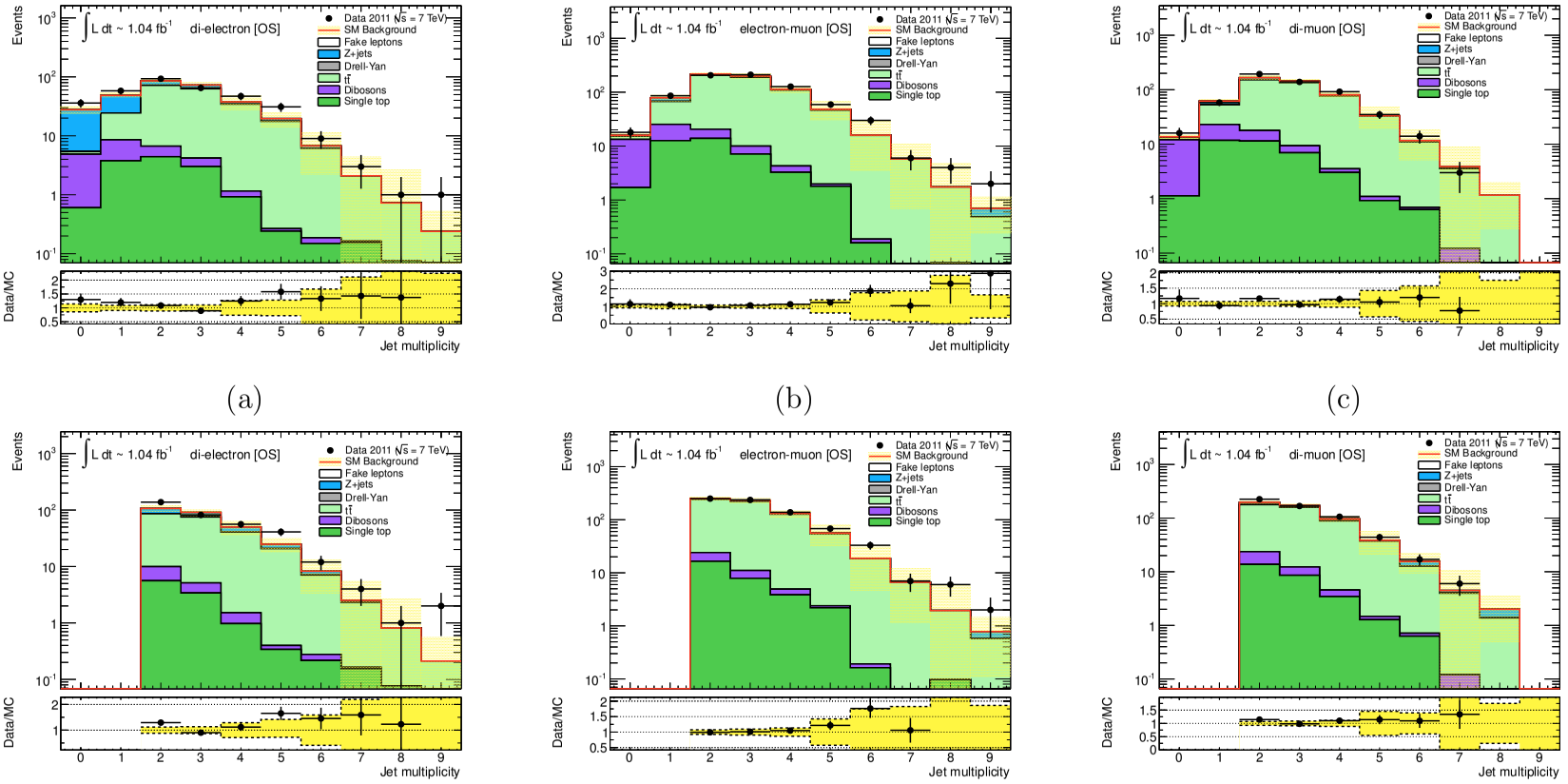

Figure 4.17: Data and Monte Carlo jet multiplicity distributions for the three dilepton channels ($e^{\pm}e^{\mp}$, $e^{\pm}\mu^{\mp}$ and $\mu^{\pm}\mu^{\mp}$) respectively in FS-SR1 (a-c) and FS-SR2 (d-f).

Sample	$e^{\pm}e^{\mp}$	$e^{\pm}\mu^{\mp}$	$\mu^{\pm}\mu^{\mp}$
$t\bar{t}$	199.47±10.55±8.37	580.50±24.35±14.10	410.72±21.09±11.20
Z+jets	75.40±6.34±6.04	40.87±4.12±4.10	37.42±5.82±3.64
diBoson	12.77±1.02±1.60	35.08±1.83±2.83	31.78±2.02±2.44
single top	13.34±0.71±0.95	40.54±1.67±1.64	35.84±1.87±1.49
Drell Yan	0.57±0.09±0.37	0.04±0.00±0.03	0.63±0.66±0.28
Fakes	5.3±9.8±1.7	30.2±9.7±6.1	21.8±16.2±6.1
SM all	306.85±15.78±10.63	727.23±26.65±16.23	538.19±27.37±13.57
data 2011	344.00	750.00	551.00

Table 4.24: Number of dilepton events ($e^{\pm}e^{\mp}$, $e^{\pm}\mu^{\mp}$ and $\mu^{\pm}\mu^{\mp}$) in FS SR1 ($E_T^{miss} > 80$ GeV and Z veto). The contributions are reported with (sys.) and (stat.) uncertainties.

Sample	$e^{\pm}e^{\mp}$	$e^{\pm}\mu^{\mp}$	$\mu^{\pm}\mu^{\mp}$
$t\bar{t}$	215.61±12.78±8.53	629.00±32.45±14.70	438.30±27.60±11.71
Z+jets	50.64±19.73±4.78	29.17±5.97±3.44	42.77±11.48±4.04
diBoson	6.75±2.28±0.99	12.16±3.43±1.66	15.17±4.32±1.44
single top	10.74±1.34±0.88	30.56±3.01±1.41	27.66±3.44±1.32
Drell Yan	0.57±0.11±0.37	0.04±0.00±0.03	0.63±0.66±0.28
Fakes	1.5±6.7±1.5	32.3±16.1±6.3	19.4±15.3 ±5.7
SM all	285.81±24.59±9.99	733.23±37.00±16.50	543.93±34.04±13.78
data 2011	336.00	741.00	567.00

Table 4.25: Number of dilepton events ($e^{\pm}e^{\mp}$, $e^{\pm}\mu^{\mp}$ and $\mu^{\pm}\mu^{\mp}$) in FS SR2 ($E_T^{miss} > 80$ GeV and at least 2 jets). The contributions are quoted with (sys.) and (stat.) uncertainties.

identical flavour events $\mathcal{S}$, weighting the numbers of observed dilepton events with the appropriate trigger efficiencies and β already retrieved. The results for the three signal regions of the flavour subtraction analysis are:

FSSR1: $\mathcal{S}_{obs} = 132.11 \pm 1.70(\beta) \pm 0.98(\tau)$

FSSR2: $\mathcal{S}_{obs} = 142.55 \pm 1.70(\beta) \pm 1.01(\tau)$

FSSR3: $\mathcal{S}_{obs} = -3.05 \pm 0.01(\beta) \pm 0.00(\tau)$

4.10.2 Monte Carlo estimation of $\mathcal{S}$

From a similar analysis on Monte Carlo Standard Model samples we can obtain the results for the $e^{\pm}e^{\mp}$, $e^{\pm}\mu^{\mp}$ and $\mu^{\pm}\mu^{\mp}$ channels reported in tables 4.24, 4.25 and 4.26.

Reading the numbers of these tables, two features appear worth of remark: the first aspect is the good agreement between the observations in data and the Monte Carlo predictions of the Standard Model processes: the data can be well

Sample	$e^{\pm}e^{\mp}$	$e^{\pm}\mu^{\mp}$	$\mu^{\pm}\mu^{\mp}$
$t\bar{t}$	1.98 ± 1.22 ± 0.93	5.23 ± 1.89 ± 1.35	3.20 ± 1.54 ± 1.16
Z+jets	0.01 ± 0.05 ± 0.01	1.03 ± 0.04 ± 0.62	0.74 ± 0.16 ± 0.53
diBoson	0.47 ± 0.03 ± 0.25	0.39 ± 0.03 ± 0.29	0.74 ± 0.27 ± 0.28
single top	0.04 ± 0.05 ± 0.05	0.33 ± 0.08 ± 0.11	0.49 ± 0.10 ± 0.17
Drell Yan	0.00 ± 0.00 ± 0.00	0.00 ± 0.00 ± 0.00	0.00 ± 0.00 ± 0.00
Fakes	0.17 ± 0.36 ± 0.19	0.92 ± 1.15 ± 0.96	0.08 ± 0.03 ± 0.03
SM all	2.67 ± 1.27 ± 0.97	7.90 ± 2.21 ± 1.80	5.25 ± 1.58 ± 1.32
data 2011	2.00	8.00	3.00

Table 4.26: Number of dilepton events ($e^{\pm}e^{\mp}$, $e^{\pm}\mu^{\mp}$ and $\mu^{\pm}\mu^{\mp}$) in FS SR3 ($E_T^{miss} > 250$ GeV). The contributions are reported with (sys.) and (stat.) uncertainties.

described in terms of Standard Model Physics. This numerical compatibility is well evident also in the distributions of the main variables of the dilepton events of the signal regions: in figure 4.15 the invariant mass distributions of the lepton pairs for the three opposite sign dilepton channels for the FS-SR1 and FS-SR2 are reported; in figure 4.16 I report the E_T^{miss} distributions, where is overt the cut $E_T^{miss} > 80$ GeV present in the definition of the two first signal regions, while figure 4.17 shows the jet multiplicity of dilepton events (with the request of at least two jets in the FS-SR2). In the figures, the data observed distributions and those predicted by the Monte Carlo generators are superimposed in order to facilitate the comparison: the agreement data-Monte Carlo is very good and satisfactory in all the distributions for both the signal regions. The distributions for the third signal region FS-SR3 are not shown since the statistic in this region is very poor and so the comparison meaningless.

The second aspect that emerges looking at the numbers written in the tables 4.24, 4.25 and 4.26 is the importance of the top background: $t\bar{t}$ is the main Standard Model background in all the three signal regions of the flavour subtraction analysis. According to the Monte Carlo predictions, it represents the 75.73% of the total Standard Model background in the SR1 and the 82.08% in the SR2. Its importance lightly decreases in the SR3 (65.8%), although in this region the statistics is extremely poor. This is not a surprise, but an expected result. Now, we can evaluate the power of the flavour subtraction analysis in the rejection and cancelation of the $t\bar{t}$ background calculating the identical flavour excess $\bar{\mathcal{S}}_b$ (where b means background) in the three signal regions. In the table 4.27 the values of $\bar{\mathcal{S}}_b$ in the three signal regions of the flavour subtraction analysis are reported for the various Standard Model processes: taking into account the systematic and the statistical uncertainties, the $\bar{\mathcal{S}}_b$ for $t\bar{t}$ is compatible with zero and so the sought flavour cancelation is realized. As already noticed, the reason of this cancelation is that the top (anti-top) quark decay chain presents at the end an electron or a muon with the same probability (branching ratio) and so $t\bar{t}$ decay in identical flavour and

different flavour lepton pair events in a symmetric way. As expected, the main irreducible background for the flavour subtraction is the Z+jets process.

In the tables from 4.28 to 4.33, I show the detailed break down for the overall systematic uncertainty (see section 4.7.1): for the computation of the total systematic we considerer only the biggest contribution of each of the (up/down) systematical variations in JES, μ and Energy systematic effects. When applying the flavour subtraction, I must take into account also additional systematics like the variation of $\mathcal{S}$ due to the error of β, τ_e and τ_{mu}. But, as already underlined, other systematics in the different channels will suppress each other due to the subtraction. The luminosity, parton distribution function, jet energy scale and resolution, electron scale and resolution, ID and MS muon momentum and trigger and β uncertainties are all uncertainties which are perfectly correlated between the backgrounds. These are each summed linearly to give the uncertainty from each of these systematics on the total Standard Model estimate. Only the cross-section uncertainties are not correlated between the backgrounds and are therefore added in quadrature. Finally, the estimates for each source of uncertainty on $\bar{\mathcal{S}}_b$ are added in quadrature to give the total systematic uncertainty on the Monte Carlo $\mathcal{S}$ estimation. The statistical uncertainties of the various Standard Model processes are added in quadrature to obtain the total one.

So, the results for the three signal regions of the flavour subtraction analysis are:

FSSR1: $\bar{\mathcal{S}}_b = 100.53 \pm 19.88$ (sys) ± 24.12 (stat)

FSSR2: $\bar{\mathcal{S}}_b = 70.32 \pm 32.29$ (sys) ± 23.86 (stat)

FSSR3: $\bar{\mathcal{S}}_b =$ -0.27 ± 3.75 (sys) ± 2.45 (stat)

Sample	$\bar{\mathcal{S}}_b$ (FSSR1)	$\bar{\mathcal{S}}_b$ (FSSR2)	$\bar{\mathcal{S}}_b$ (FSSR3)
$t\bar{t}$	3.977 ± 13.872 ± 20.073	-1.570 ± 8.963 ± 20.788	-0.097 ± 3.712 ± 2.054
Z+jets	90.176 ± 13.140 ± 9.594	72.365 ± 30.394 ± 7.980	-0.444 ± 0.042 ± 0.743
diBoson	6.553 ± 1.200 ± 4.034	8.615 ± 3.224 ± 2.408	0.810 ± 0.087 ± 0.496
single top	4.968 ± 1.813 ± 2.382	5.160 ± 1.647 ± 2.110	0.093 ± 0.075 ± 0.184
Drell Yan	1.227 ± 0.610 ± 0.573	1.227 ± 0.610 ± 0.548	0.000 ± 0.000 ± 0.000

Table 4.27: $\bar{\mathcal{S}}_b$ for the Standard Model processes obtained from a Monte Carlo study. The contributions are quoted with (sys.) and (stat.) uncertainties.

process	$\bar{\mathcal{S}}_b$	$\text{JES}_\uparrow$	$\text{JES}_\downarrow$	JER	$\text{E}_{e,\uparrow}$	$\text{E}_{e,\downarrow}$	$\mu_{MS,\uparrow}$	$\mu_{MS,\downarrow}$	$\mu_{ID,\uparrow}$	$\mu_{ID,\downarrow}$	$\text{scale}_{sys.}$
$t\bar{t}$	3.977	8.871	13.013	3.756	0.371	0.494	1.788	1.300	0.425	2.025	13.820
Z+jets	90.176	1.894	4.854	9.468	2.621	0.055	0.745	0.774	0.319	0.086	10.990
diBoson	6.553	0.381	0.841	0.400	0.109	0.123	0.093	0.421	0.316	0.284	1.077
single top	4.968	0.650	1.303	1.088	0.012	0.123	0.342	0.259	0.210	0.332	1.767
Drell Yan	1.227	0.066	0.105	0.593	0.000	0.000	0.000	0.000	0.000	0.000	0.602

Table 4.28: FS-SR1: $\bar{\mathcal{S}}_b$ and systematics due to scale uncertainties after flavour subtraction.

process	$\bar{\mathcal{S}}_b$	$\mathcal{L}_{sys.}$	pdf_{sys}	σ_{sys}	β_{sys}	$\tau_{e,sys}$	$\tau_{\mu,sys}$	scale_{sys}	tot. sys.	stats.
$t\bar{t}$	3.977	0.147	0.199	0.278	1.129	0.117	0.131	13.820	13.872	20.073
Z+jets	90.176	3.337	4.509	4.509	0.289	0.009	0.012	10.990	13.140	9.594
diBoson	6.553	0.242	0.328	0.328	0.081	0.007	0.010	1.077	1.200	4.034
single top	4.968	0.184	0.248	0.248	0.089	0.008	0.011	1.767	1.813	2.382
Drell Yan	1.227	0.045	0.061	0.061	0.002	0.000	0.000	0.602	0.610	0.573

Table 4.29: FS-SR1: $\bar{\mathcal{S}}_b$ with systematic and statistical uncertainties.

process	$\bar{\mathcal{S}}_b$	JES$_\uparrow$	JES$_\downarrow$	JER	E$_{e,\uparrow}$	E$_{e,\downarrow}$	$\mu_{MS,\uparrow}$	$\mu_{MS,\downarrow}$	$\mu_{ID,\uparrow}$	$\mu_{ID,\downarrow}$	scale$_{sys.}$
$t\bar{t}$	-1.570	7.856	3.235	3.908	1.195	1.129	0.302	0.238	0.530	0.550	8.878
Z+jets	72.365	13.689	3.179	26.446	0.800	1.397	0.538	1.291	0.154	0.170	29.840
diBoson	8.615	2.495	1.155	1.863	0.112	0.341	0.297	0.090	0.113	0.028	3.149
single top	5.160	1.384	1.056	0.540	0.009	0.222	0.402	0.303	0.165	0.345	1.593
Drell Yan	1.227	0.066	0.105	0.593	0.000	0.000	0.000	0.000	0.000	0.000	0.602

Table 4.30: FS-SR2: $\bar{\mathcal{S}}_b$ and systematics due to scale uncertainties after flavour subtraction.

process	$\bar{\mathcal{S}}_b$	$\mathcal{L}_{sys.}$	pdf$_{sys}$	σ_{sys}	β_{sys}	$\tau_{e,sys}$	$\tau_{\mu,sys}$	scale$_{sys}$	tot. sys.	stats.
$t\bar{t}$	-1.570	-0.058	-0.079	-0.110	1.211	0.127	0.140	8.878	8.963	20.788
Z+jets	72.365	2.678	3.618	3.618	0.207	0.006	0.014	29.840	30.394	7.980
diBoson	8.615	0.319	0.431	0.431	0.040	0.002	0.005	3.149	3.224	2.408
single top	5.160	0.191	0.258	0.258	0.070	0.006	0.009	1.593	1.647	2.110
Drell Yan	1.227	0.045	0.061	0.061	0.002	0.000	0.000	0.602	0.610	0.548

Table 4.31: FS-SR2: $\bar{\mathcal{S}}_b$ with systematic and statistical uncertainties.

process	$\bar{\mathcal{S}}_b$	$\text{JES}_\uparrow$	$\text{JES}_\downarrow$	JER	$\text{E}_{e,\uparrow}$	$\text{E}_{e,\downarrow}$	$\mu_{MS,\uparrow}$	$\mu_{MS,\downarrow}$	$\mu_{ID,\uparrow}$	$\mu_{ID,\downarrow}$	$\text{scale}_{sys.}$
$t\bar{t}$	-0.097	2.760	2.708	2.328	0.000	0.772	0.265	0.268	0.268	0.237	3.712
Z+jets	-0.444	0.017	0.000	0.017	0.000	0.000	0.000	0.000	0.000	0.000	0.024
diBoson	0.810	0.052	0.010	0.019	0.000	0.011	0.005	0.001	0.001	0.005	0.057
single top	0.093	0.002	0.043	0.035	0.000	0.000	0.000	0.036	0.036	0.000	0.075
Drell Yan	0.000	0.000	0.000	0.000	0.000	0.000	0.000	0.000	0.000	0.000	0.000

Table 4.32: FS-SR3: $\bar{\mathcal{S}}_b$ and systematics due to scale uncertainties after flavour subtraction.

process	$\bar{\mathcal{S}}_b$	$\mathcal{L}_{sys.}$	pdf_{sys}	σ_{sys}	β_{sys}	$\tau_{e,sys}$	$\tau_{\mu,sys}$	scale_{sys}	tot. sys.	stats.
$t\bar{t}$	-0.097	-0.004	-0.005	-0.007	0.010	0.001	0.001	3.712	3.712	2.054
Z+jets	-0.444	-0.016	-0.022	-0.022	0.002	0.000	0.000	0.024	0.042	0.743
diBoson	0.810	0.030	0.041	0.041	0.002	0.000	0.000	0.057	0.087	0.496
single top	0.093	0.003	0.005	0.005	0.001	0.000	0.000	0.075	0.075	0.184
Drell Yan	0.000	0.000	0.000	0.000	0.000	0.000	0.000	0.000	0.000	0.000

Table 4.33: FS-SR3: $\bar{\mathcal{S}}_b$ with systematic and statistical uncertainties.

4.10.3 Partially data-driven estimation of $\mathcal{S}$

Another way to determinate the excess $\mathcal{S}$ of identical flavour lepton pair in the three signal regions of the flavour subtraction analysis is to exploit the partially data-driven estimation of the Standard Model backgrounds. These estimates are reported in table 4.17 for the three dilepton channels $e^{\pm}e^{\mp}$, $e^{\pm}\mu^{\mp}$ and $\mu^{\pm}\mu^{\mp}$.

Using these numbers and the correct trigger efficiencies and β value, I obtain:

FSSR1: $\bar{\mathcal{S}}_b$ = 111.13 ± 19.93 (sys) ± 26.09 (stat)

FSSR2: $\bar{\mathcal{S}}_b$ = 65.01 ± 26.75 (sys) ± 24.99 (stat)

FSSR3: $\bar{\mathcal{S}}_b$ = -0.16 ± 2.71 (sys) ± 1.47 (stat)

4.10.4 Monte Carlo estimation of $\mathcal{S}$ with lepton weights

I have estimated the excess of identical flavour dilepton events weighting the number of dilepton events in the three opposite sign channels ($e^{\pm}e^{\mp}$, $e^{\pm}\mu^{\mp}$ and $\mu^{\pm}\mu^{\mp}$) with appropriate scale factors taking into account the different reconstruction (ϵ_e and ϵ_μ) and trigger efficiencies (τ_e and τ_μ) for electrons and muons (see the master equation 4.15 defining $\mathcal{S}$). Until now I determined $\bar{\mathcal{S}}_b$ using the same efficiencies for all the lepton pair events regardless of the direction of the lepton tracks and so, for each opposite sign channel, I considered always the same scale factor. Now I want to refine this estimation using different weights depending on the η of each lepton of the dilepton events in the signal regions and so taking into account if the lepton is detected in the barrel (B: $|\eta| < 1.05$) or in the end-cap region (EC: $|\eta| > 1.05$). In this way, for each lepton pair $\ell_1\ell_2$, I have four possible combinations and scale factors: ℓ_1(B) ℓ_2(B), ℓ_1(B) ℓ_2(EC), ℓ_1(EC) ℓ_2(B) and ℓ_1(EC) ℓ_2(EC) (only three if I have identical flavour leptons). So, for example, the term for $e^{\pm}e^{\mp}$ events in equation 4.15 becomes:

$$\frac{N(e^{\pm}e^{\mp})}{\beta(1-(1-\tau_e)^2)}$$

$$\downarrow$$

$$\frac{N(e^{\pm}(B)e^{\mp}(B))}{\beta_B(1-(1-\tau_{eB})^2)} + \frac{N(e^{\pm}(B)e^{\mp}(EC))}{\beta(1-(1-\tau_{eB})*(1-\tau_{eEC}))} + \frac{N(e^{\pm}(EC)e^{\mp}(EC))}{\beta_{EC}(1-(1-\tau_{eEC})^2)}$$

For the lepton pairs with one lepton in the barrel region and one in the end-cap I use a common β value.

I perform this study on the Standard Model backgrounds irreducible for the flavour subtraction analysis: Z+jets and diboson events. All the results are determined using the Monte Carlo datasets. For retrieving the four (three) scale factors I must obtain the electron and muon efficiencies separately for the

	Z+jets	diBoson
τ_{eB}	0.995 ± 0.001	0.995 ± 0.003
τ_{eEC}	0.974 ± 0.001	0.977 ± 0.005
$\tau_{\mu B}$	0.761 ± 0.005	0.682 ± 0.015
$\tau_{\mu EC}$	0.874 ± 0.003	0.851 ± 0.012
β_B	0.831 ± 0.001	0.868 ± 0.007
β_{EC}	0.641 ± 0.001	0.681 ± 0.008

Table 4.34: Trigger and reconstruction efficiencies for electrons and muons for the barrel (B) and end-cap (EC) regions for the two more challenging (for my flavour subtraction analysis) Standard Model backgrounds: Z+jets and diboson processes. The errors are statistical.

barrel and end-cap regions. I apply the Monte Carlo techniques described in the previous sections (4.9.1 and 4.9.2). The results are reported in table 4.34.

Using the efficiencies just obtained, I can calculate the correct scale factors for the various combinations of lepton pairs and so compute the new identical flavour excess $\bar{\mathcal{S}}_b$ in the three signal regions FS-SR1, FS-SR2 and FS-SR3. In table 4.35 and 4.36 I report the number of dilepton ($N_{\ell_1\ell_2}$) events (separated according to the η of each lepton: $N_{\ell_{1B}\ell_{2B}}$, $N_{\ell_{1B}\ell_{2EC}}$, $N_{\ell_{1EC}\ell_{2B}}$ and $N_{\ell_{1EC}\ell_{2EC}}$) expected in the three signal regions for the Z+jets and diboson backgrounds respectively and the estimated $\bar{\mathcal{S}}_b$. The comparison between this "weighted" $\bar{\mathcal{S}}_b$ and the $\bar{\mathcal{S}}_b$ calculated with a common scale factor shows a good agreement: the weighted values are a bit higher especially in the first two signal regions but the difference is widely inside the statistical error. This result highlights that the (easer) use of a common efficiency and scale factor regardless the η direction of the lepton is a very good and acceptable approximation.

4.11 Limits and interpretation

The presence of Supersymmetric signal could be revealed by an excess $\mathcal{S}_{obs}$ of identical flavour lepton pairs higher than that predict by the Standard Model ($\bar{\mathcal{S}}_b$): in fact, as already noticed, if the Supersymmetry exists in nature, it presents new sources of identical flavour lepton pairs in addition to the Standard Model ones. If we compare the results shown in the previous section 4.10, we can notice that the observed value $\mathcal{S}_{obs}$ in data is really higher than $\bar{\mathcal{S}}_b$ predicted only taking into account the Standard Model processes (at least in the first two signal regions, FSSR1 and FSSR2. Different is the result in FSSR3, but the statistic is very poor and so it is very difficult to draw conclusions in this region ($E_T^{miss} > 250$ GeV)). However, if we considerer the statistical and systematic uncertainties the values become compatible. We can verify this compatibility also graphically: in figure 4.18 I show the invariant mass distributions for Standard Model (Monte Carlo, red line) and data observations (black

	FS-SR1	FS-SR2	FS-SR3
N_{ee}	75.40	50.64	0.01
N_{eBeB}	40.27	28.00	0.01
N_{eBeEC}	13.47	12.43	0.00
N_{eECeEC}	21.66	10.21	0.00
$N_{e\mu}$	40.87	29.17	1.03
$N_{eB\mu B}$	29.03	21.95	0.64
$N_{eB\mu EC}$	4.66	3.37	0.00
$N_{eEC\mu B}$	2.18	0.91	0.00
$N_{eEC\mu EC}$	5.00	2.94	0.39
$N_{\mu\mu}$	37.42	42.77	0.74
$N_{\mu B\mu B}$	21.38	23.50	0.74
$N_{\mu B\mu EC}$	8.10	10.04	0.00
$N_{\mu EC\mu EC}$	7.94	9.23	0.00
$\bar{\mathcal{S}}_b$ weighted	92.560 ± 9.581	74.883 ± 7.918	-0.467 ± 0.751
$\mathcal{S}_b$	90.176 ± 9.594	72.365 ± 7.980	-0.444 ± 0.743

Table 4.35: Number of dilepton events in the three opposite sign channels ($e^{\pm}e^{\mp}$, $e^{\pm}\mu^{\mp}$ and $\mu^{\pm}\mu^{\mp}$) for the three signal regions for the Z background. The lepton pair $\ell_1\ell_2$ events are distinguished in three (four) categories for taking into account the η of each lepton: ℓ_1(B) ℓ_2(B), ℓ_1(B) ℓ_2(EC), (ℓ_1(EC) ℓ_2(B) for different flavour $e^{\pm}\mu^{\mp}$ pairs) and ℓ_1(EC) ℓ_2(EC). The excess $\bar{\mathcal{S}}_b$ obtained with separate weights and with common only weights are reported with statistical error.

points) obtained after the flavour subtraction for the first two signal regions, FS-SR1 and FS-SR2: I weighted the three dilepton invariant mass distribution for $e^{\pm}e^{\mp}$, $e^{\pm}\mu^{\mp}$ and $\mu^{\pm}\mu^{\mp}$ channels for the appropriate efficiency factor according equation 4.15 and then I subtracted the different flavour distribution from the identical flavour one. So, the figure shows a comparison between $\mathcal{S}_{obs}$ and $\bar{\mathcal{S}}_b$. In general, the agreement is good and the excess observed in the data is compatible in the errors with that predicted for the Standard Model. Only around an invariant mass $m_{\ell\ell}$ of 100 GeV (in both the signal regions) we notice a more marked identical flavour lepton excess in the data with respect to the Standard Model. However, I damp the enthusiasm since $\mathcal{S}_{obs}$ and $\bar{\mathcal{S}}_b$ are compatible in two standard deviations. So, we can not announce a discovery. However, we can put limits on SUSY production.

To check and refine the previous observations, we want to ascertain better whether the observation of $\mathcal{S}$ from the data ($\mathcal{S}_{obs}$) is consistent with expectation from Standard Model processes ($\bar{\mathcal{S}}_b$) evaluating the shape of the predicted $\mathcal{S}$ distribution (following the Poisson fluctuations in the potential numbers of events in each channel) in the presence of only the Standard Model and understanding what range of observed $\mathcal{S}_{obs}$ would have been consistent with

	FS-SR1	FS-SR2	FS-SR3
N_{ee}	12.77	6.75	0.47
N_{eBeB}	8.86	4.78	0.41
N_{eBeEC}	3.01	1.51	0.04
N_{eECeEC}	0.90	0.46	0.02
$N_{e\mu}$	35.08	12.16	0.39
$N_{eB\mu B}$	22.22	7.84	0.21
$N_{eB\mu EC}$	5.18	1.87	0.00
$N_{eEC\mu B}$	4.53	1.55	0.09
$N_{eEC\mu EC}$	3.15	0.99	0.09
$N_{\mu\mu}$	31.78	15.17	0.74
$N_{\mu B\mu B}$	19.17	9.20	0.49
$N_{\mu B\mu EC}$	9.61	4.42	0.23
$N_{\mu EC\mu EC}$	3.00	1.55	0.02
$\bar{\mathcal{S}}_b$ weighted	8.366 ± 4.084	9.538 ± 2.432	0.863 ± 0.492
$\bar{\mathcal{S}}_b$	6.553 ± 4.034	8.615 ± 2.408	0.810 ± 0.496

Table 4.36: Number of dilepton events in the three opposite sign channels ($e^{\pm}e^{\mp}$, $e^{\pm}\mu^{\mp}$ and $\mu^{\pm}\mu^{\mp}$) for the three signal regions for the diboson background. The lepton pair $\ell_1\ell_2$ events are distinguished in three (four) categories for taking into account the η of each lepton: ℓ_1(B) ℓ_2(B), ℓ_1(B) ℓ_2(EC), (ℓ_1(EC) ℓ_2(B) for different flavour $e^{\pm}\mu^{\mp}$ pairs) and ℓ_1(EC) ℓ_2(EC). The excess $\bar{\mathcal{S}}_b$ obtained with separate weights and with common only weights are reported with statistical error.

the only Standard Model hypothesis. This consistency can be tested using pseudo-experiments. Similar pseudo-experiments can be used to set a limit on the contribution to $\mathcal{S}$ from new physics, $\bar{\mathcal{S}}_s$.

Each pseudo-experiment is simulated retrieving the numbers of final dilepton events in the signal regions from the Monte Carlo predicted original numbers with the add of all the uncertainties (both statistical and systematic) extracted from gaussian distributions. In more detail, for each pseudo-experiment the number of observed Standard Model events in the $e^{\pm}e^{\mp}$, $e^{\pm}\mu^{\mp}$ and $\mu^{\pm}\mu^{\mp}$ channels are taken as three random numbers drawn from three Poisson distributions. I label the means of these three Poisson distributions as: $\lambda_{b,e^{\pm}e^{\mp}}$, $\lambda_{b,e^{\pm}\mu^{\mp}}$ and $\lambda_{b,\mu^{\pm}\mu^{\mp}}$. These λ_b are not trivially set to equal the respective N_b ($N_b(e^{\pm}e^{\mp})$, $N_b(e^{\pm}e^{\mp})$ and $N_b(\mu^{\pm}\mu^{\mp})$, the predicted number of background events in each channel); at first they are decomposed into the various background contributions, $\lambda_{b,j}$ and $N_{b,j}$ for background j. Then, the $\lambda_{b,j}$ for each background are obtained by adding to each $N_{b,j}$ a series of random numbers drawn from various Gaussian distributions: for each systematic and statistical uncertainty, one random number is drawn. In the case of correlated systematics between

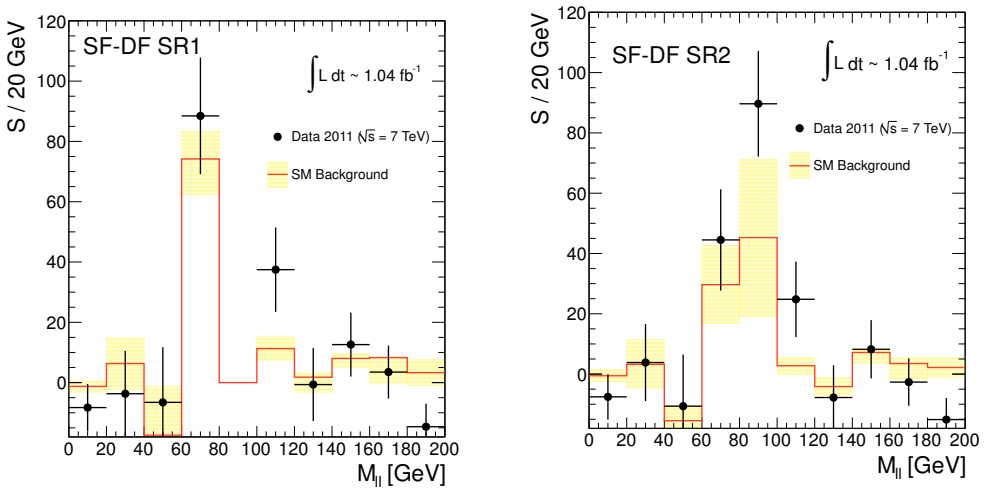

Figure 4.18: Flavour subtracted invariant mass distributions for events in data and Monte Carlo in FS-SR1 (left) and FS-SR2 (right). Errors on data points are statistical Poisson limits, while the error band on the MC represents the statistical, cross section, luminosity uncertainties and JES, JER.

backgrounds or channels, a single random number is drawn which is then appropriately scaled before application to each individual channel or background estimate. Instead, for uncorrelated errors (like as the statistical uncertainty), a different random number is drawn for each background process. The $\lambda_{b,j}$ are them summed to provide λ_b in each channel. In this way, the λ_b for each channel are "sampled". The β, τ_e and τ_μ measured by each pseudo experiment must also be sampled in the same way, using a random number drawn from a Gaussian distribution. Finally, the drawn random numbers of observed events in each channel and the sampled efficiencies are combined to measure the $\mathcal{S}$ of the pseudo-experiment in question.

The distributions of expected $\mathcal{S}$ from one-million signal free pseudo experiments for each signal region are given in Figure 4.19. The number of pseudo experiments with $\mathcal{S} > \mathcal{S}_{obs}$ are respectively 30.8%, 16.4% and 83.9% for FS-SR1, FS-SR2 and FS-SR3. This suggests that the observed identical flavour excess in data is consistent with the Standard Model.

Exclusion limits can thus be set on $\bar{\mathcal{S}}_s$, the hypothetical signal contribution from new physics. For doing this, the pseudo experiments must be modified to include new physics processes: in addition to the λ_b, λ_s can be introduced to give the mean contributions to each flavour channel from new physics. Then, combining λ_b and λ_s, we can obtain pseudo experiments observing $\mathcal{S}$ that simulate the results expected by real experiments in presence of a signal. To set a model independent limit on $\bar{\mathcal{S}}_s$, the λ_s can be put by hand in order to only 5% of the pseudo experiments predict $\mathcal{S} < \mathcal{S}_{obs}$. The λ_s are then combined to give a corresponding $\bar{\mathcal{S}}_s$. For setting a correct and reliable limit, we must

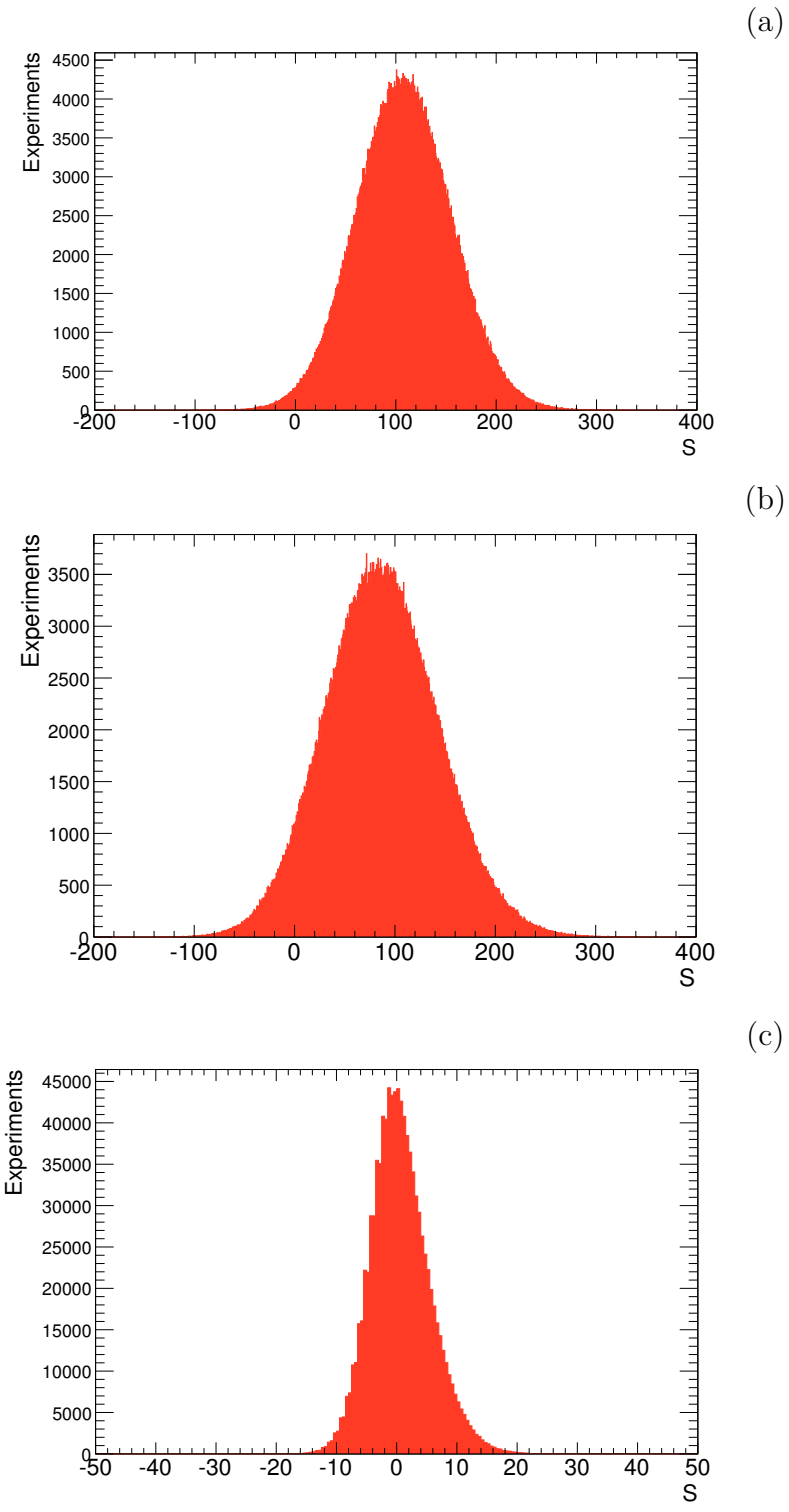

Figure 4.19: Distribution of observed $\mathcal{S}$ values from a million hypothetical signal-free pseudo-experiments. The shape is driven by statistical Poisson fluctuations in the expected rates of identical-flavour and different-flavour events. They represent the expected Standard Model distributions for $\mathcal{S}$ to compared to the observations, respectively in FS-SR1 (a), FS-SR2 (b) and FS-SR3 (c)

make an assumption regarding the relative branching ratio of signal SUSY events into identical flavour and different flavour dilepton channels; in fact, if we add flavour uncorrelated supersymmetry contributions both to the identical flavour and different flavour channels, the width of the $\mathcal{S}$ distribution increases and, in consequence, also the limit on $\mathcal{S}_s$ rises. So, in table 4.37, I report the limits on $\bar{\mathcal{S}}_s$ on the assumption that the branching fractions for $e^{\pm}e^{\mp}$ and $\mu^{\pm}\mu^{\mp}$ final states in supersymmetric events are identical and instead that for $e^{\pm}\mu^{\mp}$ final states is zero: values greater than those are excluded at 95% confidence. The more interesting result is the limit observed in the third signal region (FS-SR3 with the request of $E_T^{miss} > 250$ GeV): it is the more constricting limit and exclude a contribution ($\mathcal{S}_s$) to the identical flavour excess from a signal of new physics greater than 3.5 (or 3.3 considering the data-driven Standard Model estimations). The assumption of a contamination of different flavour SUSY events gives higher limits.

Signal Region	data-driven	MC
FS-SR1	89.5	100.1
FS-SR2	150.9	145.6
FS-SR3	3.3	3.5

Table 4.37: Observed limit on $\mathcal{S}_s$ obtained for each of the signal regions, using the data-driven estimates of the contributions in each channel from the SM background and the purely Monte Carlo estimates of the contributions in each channel from SM background.

Chapter 5

Conclusions

In this thesis, I presented the results of a flavour subtraction technique applied to the data collected by the ATLAS detector until the summer 2011 at $\sqrt{s} = 7$ TeV (corresponding to an integrated luminosity of ~ 1 fb^{-1}). The purpose of my analysis was the search for an excess of events containing opposite sign identical flavour lepton-pairs and significant missing transverse energy beyond the Standard Model expectations. In order to interpret correctly the excess of identical flavour events and understand the eventual supersymmetry contribution I presented a partially data-driven estimation of the Standard Model contribution. The comparison between data observations and Standard Model predictions shows that the collected data can be well described in terms of Standard Model processes and so no significant excess has been observed. Though I did not discover any clue of new physics, I could put model-independent exclusion limits; introducing the quantity $\mathcal{S}$ (the number of excess identical flavour events multiplied by detector acceptances and efficiencies), I obtained the more constricting and robust limit on the supersymmetry contribution ($\mathcal{S}_s$) analyzing events with missing transverse energy greater than 250 GeV: I exclude at 95% confidence excesses $\mathcal{S}_s > 3.3$. This limit is achieved on the assumption of equal branching ratios for SUSY decays to $e^{\pm}e^{\mp}$ and $\mu^{\pm}\mu^{\mp}$ and no $e^{\pm}\mu^{\mp}$ SUSY events in final states.
So, the research of new physics and in particular of supersymmetry events can continue and become more and more exciting and challenging with the analysis of new data at greater centre-of-mass energy.

Appendix

In the following tables I present the Monte Carlo datasets used in my analysis. All the samples were produced by the ATLAS central production teams.

Sample ID	Name	Generator	σxBR [pb]
105200	T1	MC@NLO Jimmy	$8.9{\cdot}10^{1}$
105860	TTbar	PowHeg Jimmy	$7.9{\cdot}10^{1}$
105861	TTbar	PowHeg Pythia	$7.9{\cdot}10^{1}$
105890	ttbarlnlnNp0	Alpgen Jimmy	5.8
105891	ttbarlnlnNp1	Alpgen Jimmy	5.7
105892	ttbarlnlnNp2	Alpgen Jimmy	3.5
105893	ttbarlnlnNp3	Alpgen Jimmy	1.6
117255	ttbar_isr_down	AcerMC Pythia	$8.9{\cdot}10^{1}$
117256	ttbar_isr_up	AcerMC Pythia	$8.9{\cdot}10^{1}$
117257	ttbar_fsr_down	AcerMC Pythia	$8.9{\cdot}10^{1}$
117258	ttbar_fsr_up	AcerMC Pythia	$8.9{\cdot}10^{1}$
117259	ttbar_isr_down_fsr_down	AcerMC Pythia	$8.9{\cdot}10^{1}$
117260	ttbar_isr_up_fsr_up	AcerMC Pythia	$8.9{\cdot}10^{1}$
108340	st_tchan_enu	MC@NLO Jimmy	7.0
108341	st_tchan_munu	MC@NLO Jimmy	7.0
108342	st_tchan_taunu	MC@NLO Jimmy	7.0
108343	st_schan_enu	MC@NLO Jimmy	$4.7{\cdot}10^{-1}$
108344	st_schan_munu	MC@NLO Jimmy	$4.7{\cdot}10^{-1}$
108345	st_schan_taunu	MC@NLO Jimmy	$4.7{\cdot}10^{-1}$
108346	st_Wt	MC@NLO Jimmy	$1.3{\cdot}10^{1}$

Table 5.1: top and diboson Monte Carlo samples with sample ID, generator, cross section numbers.

Sample ID	Name	Generator	σxBR [pb]	k–factor
107680	WenuNp0_pt20	AlpgenJimmy	$6.9{\cdot}10^3$	1.20
107681	WenuNp1_pt20	AlpgenJimmy	$1.3{\cdot}10^3$	1.20
107682	WenuNp2_pt20	AlpgenJimmy	$3.8{\cdot}10^2$	1.20
107683	WenuNp3_pt20	AlpgenJimmy	$1.0{\cdot}10^2$	1.20
107684	WenuNp4_pt20	AlpgenJimmy	$2.5{\cdot}10^1$	1.20
107685	WenuNp5_pt20	AlpgenJimmy	6.9	1.20
107690	WmunuNp0_pt20	AlpgenJimmy	$6.9{\cdot}10^3$	1.20
107691	WmunuNp1_pt20	AlpgenJimmy	$1.3{\cdot}10^3$	1.20
107692	WmunuNp2_pt20	AlpgenJimmy	$3.8{\cdot}10^2$	1.20
107693	WmunuNp3_pt20	AlpgenJimmy	$1.0{\cdot}10^2$	1.20
107694	WmunuNp4_pt20	AlpgenJimmy	$2.5{\cdot}10^1$	1.20
107695	WmunuNp5_pt20	AlpgenJimmy	6.9	1.20
107700	WtaunuNp0_pt20	AlpgenJimmy	$6.9{\cdot}10^3$	1.20
107701	WtaunuNp1_pt20	AlpgenJimmy	$1.3{\cdot}10^3$	1.20
107702	WtaunuNp2_pt20	AlpgenJimmy	$3.8{\cdot}10^2$	1.20
107703	WtaunuNp3_pt20	AlpgenJimmy	$1.0{\cdot}10^2$	1.20
107704	WtaunuNp4_pt20	AlpgenJimmy	$2.5{\cdot}10^1$	1.20
107705	WtaunuNp5_pt20	AlpgenJimmy	6.9	1.20
106280	WbbNp0_pt20	AlpgenJimmy	3.2	1.20
106281	WbbNp1_pt20	AlpgenJimmy	2.6	1.20
106282	WbbNp2_pt20	AlpgenJimmy	1.4	1.20
106283	WbbNp3_pt20	AlpgenJimmy	0.6	1.20
107280	WbbFullNp0_pt20	AlpgenJimmy	$4.6{\cdot}10^1$	-
107281	WbbFullNp1_pt20	AlpgenJimmy	$3.4{\cdot}10^1$	-
107282	WbbFullNp2_pt20	AlpgenJimmy	$1.7{\cdot}10^1$	-
107283	WbbFullNp3_pt20	AlpgenJimmy	6.3	-

Table 5.2: W-Monte Carlo samples with sample ID, generator, cross section, k-factor numbers. For some samples k-factors are included in the total cross section and not given explicitly in the table.

Sample ID	Name	Generator	σxBR [pb]	k–factor
107650	ZeeNp0_pt20	AlpgenJimmy	$6.6{\cdot}10^{2}$	1.25
107651	ZeeNp1_pt20	AlpgenJimmy	$1.3{\cdot}10^{2}$	1.25
107652	ZeeNp2_pt20	AlpgenJimmy	$4.0{\cdot}10^{1}$	1.25
107653	ZeeNp3_pt20	AlpgenJimmy	$1.1{\cdot}10^{1}$	1.25
107654	ZeeNp4_pt20	AlpgenJimmy	2.9	1.25
107655	ZeeNp5_pt20	AlpgenJimmy	$7.5{\cdot}10^{-1}$	1.25
107660	ZmumuNp0_pt20	AlpgenJimmy	$6.6{\cdot}10^{2}$	1.25
107661	ZmumuNp1_pt20	AlpgenJimmy	$1.3{\cdot}10^{2}$	1.25
107662	ZmumuNp2_pt20	AlpgenJimmy	$4.0{\cdot}10^{1}$	1.25
107663	ZmumuNp3_pt20	AlpgenJimmy	$1.1{\cdot}10^{1}$	1.25
107664	ZmumuNp4_pt20	AlpgenJimmy	2.9	1.25
107665	ZmumuNp5_pt20	AlpgenJimmy	$7.5{\cdot}10^{-1}$	1.25
107670	ZtautauNp0_pt20	AlpgenJimmy	$6.6{\cdot}10^{2}$	1.25
107671	ZtautauNp1_pt20	AlpgenJimmy	$1.3{\cdot}10^{2}$	1.25
107672	ZtautauNp2_pt20	AlpgenJimmy	$4.0{\cdot}10^{1}$	1.25
107673	ZtautauNp3_pt20	AlpgenJimmy	$1.1{\cdot}10^{1}$	1.25
107674	ZtautauNp4_pt20	AlpgenJimmy	2.9	1.25
107675	ZtautauNp5_pt20	AlpgenJimmy	$7.5{\cdot}10^{-1}$	1.25
116250	ZeeNp0_Mll10to40	AlpgenJimmy	$3.0{\cdot}10^{3}$	-
116251	ZeeNp1_Mll10to40	AlpgenJimmy	84.91	-
116252	ZeeNp2_Mll10to40	AlpgenJimmy	41.19	-
116253	ZeeNp3_Mll10to40	AlpgenJimmy	8.35	-
116254	ZeeNp4_Mll10to40	AlpgenJimmy	1.85	-
116255	ZeeNp5_Mll10to40	AlpgenJimmy	0.46	-
116260	Z$\mu\mu$Np0_Mll10to40	AlpgenJimmy	$3.0{\cdot}10^{3}$	-
116261	Z$\mu\mu$Np1_Mll10to40	AlpgenJimmy	84.78	-
116262	Z$\mu\mu$Np2_Mll10to40	AlpgenJimmy	41.13	-
116263	Z$\mu\mu$Np3_Mll10to40	AlpgenJimmy	8.34	-
116264	Z$\mu\mu$Np4_Mll10to40	AlpgenJimmy	1.87	-
116265	Z$\mu\mu$Np5_Mll10to40	AlpgenJimmy	0.46	-
116270	Z$\tau\tau$Np0_Mll10to40	AlpgenJimmy	$3.0{\cdot}10^{3}$	-
116271	Z$\tau\tau$Np1_Mll10to40	AlpgenJimmy	84.88	-
116272	Z$\tau\tau$Np2_Mll10to40	AlpgenJimmy	41.28	-
116273	Z$\tau\tau$Np3_Mll10to40	AlpgenJimmy	8.35	-
116274	Z$\tau\tau$Np4_Mll10to40	AlpgenJimmy	1.83	-
116275	Z$\tau\tau$Np5_Mll10to40	AlpgenJimmy	0.46	-

Table 5.3: Z and Drell Yan Monte Carlo samples with sample ID, generator, cross section, k–factor numbers. For some samples k–factors are included in the total cross section and not given explicitly in the table.

105985	WW	Herwig	$1.7{\cdot}10^{1}$
105986	ZZ	Herwig	$1.3{\cdot}10^{1}$
105987	WZ	Herwig	$5.5{\cdot}10^{1}$
107100	WWlnulnuNp0	Alpgen	2.6
107101	WWlnulnuNp1	Alpgen	1.3
107102	WWlnulnuNp2	Alpgen	$5.7{\cdot}10^{-1}$
107103	WWlnulnuNp3	Alpgen	$2.2{\cdot}10^{-1}$
107104	WZincllNp0	Alpgen	$8.6{\cdot}10^{-1}$
107105	WZincllNp1	Alpgen	$5.3{\cdot}10^{-1}$
107106	WZincllNp2	Alpgen	$2.9{\cdot}10^{-1}$
107107	WZincllNp3	Alpgen	$1.2{\cdot}10^{-1}$
107108	ZZincllNp0	Alpgen	$6.6{\cdot}10^{-1}$
107109	ZZincllNp1	Alpgen	$3.0{\cdot}10^{-1}$
107110	ZZincllNp2	Alpgen	$1.1{\cdot}10^{-1}$
107111	ZZincllNp3	Alpgen	$4.1{\cdot}10^{-2}$
119357	W^+W^+_jj	MadGraph	$2.2{\cdot}10^{-1}$
105921	W^+W^-_eνeν	MC@NLO Jimmy	$5.7\cdot10^{-1}$
105922	W^+W^-_e$\nu\mu\nu$	MC@NLO Jimmy	$5.7\cdot10^{-1}$
105923	W^+W^-_e$\nu\tau\nu$	MC@NLO Jimmy	$5.7\cdot10^{-1}$
105924	W^+W^-_$\mu\nu\mu\nu$	MC@NLO Jimmy	$5.7\cdot10^{-1}$
105925	W^+W^-_$\mu\nu$eν	MC@NLO Jimmy	$5.7\cdot10^{-1}$
105926	W^+W^-_$\mu\nu\tau\nu$	MC@NLO Jimmy	$5.7\cdot10^{-1}$
105927	W^+W^-_$\tau\nu\tau\nu$	MC@NLO Jimmy	$5.7\cdot10^{-1}$
105928	W^+W^-_$\tau\nu$eν	MC@NLO Jimmy	$5.7\cdot10^{-1}$
105929	W^+W^-_$\tau\nu\mu\nu$	MC@NLO Jimmy	$5.7\cdot10^{-1}$
105930	ZZ_llqq	MC@NLO Jimmy	$5.3\cdot10^{-1}$
105931	ZZ_llll	MC@NLO Jimmy	$2.5\cdot10^{-2}$
105932	ZZ_ll$\nu\nu$	MC@NLO Jimmy	$1.5\cdot10^{-1}$
105940	W^+Z_lνqq	MC@NLO Jimmy	1.7
105941	W^+Z_lνll	MC@NLO Jimmy	$1.6\cdot10^{-1}$
105942	W^+Z_qqlli	MC@NLO Jimmy	$5.0\cdot10^{-1}$
105970	W^-Z_lνqq	MC@NLO Jimmy	$9.8\cdot10^{-1}$
105971	W^-Z_lνll	MC@NLO Jimmy	$8.0\cdot10^{-2}$
105972	W^-Z_qqlli	MC@NLO Jimmy	$2.7\cdot10^{-1}$
108323	Z_ee_γ	MadGraph	$1.0{\cdot}10^{1}$
108324	Z_$\mu\mu$_γ	MadGraph	$1.0{\cdot}10^{1}$
108325	Z_$\tau\tau$_γ	MadGraph	1.6
108388	W^-_$e\nu$_γ	MadGraph	$1.9{\cdot}10^{1}$
106001	W^-_$\mu\nu$_γ	MadGraph	$1.9{\cdot}10^{1}$
108388	W^-_$e\nu$_γ	MadGraph	2.9
106001	W^+_$e\nu$_γ	MadGraph	$2.8{\cdot}10^{1}$
106002	W^+_$\mu\nu$_γ	MadGraph	$2.8{\cdot}10^{1}$
106003	W^+_$\tau\nu$_γ	MadGraph	4.0

Table 5.4: Diboson Monte Carlo samples with sample ID, generator, cross section numbers.

Bibliography

[1] S. Weinberg, Phys. Rev. Lett. **19**, 1264 (1967);
A. Salam, p. 367 of Elementary Particle Theory, ed. N. Svartholm (Almquist and Wiksells, Stockholm, 1969);
S.L. Glashow, J. Iliopoulos, and L. Maiani, Phys. Rev. **D2**, 1285 (1970).

[2] M. Kobayashi, T. Maskawa, Prog. Theor. Phys. **49**, 652 (1973).

[3] K. Nakamura et al. (Particle Data Group), J. Phys. **G37** 075021 (2010) and 2011 partial update for the 2012 edition.

[4] F. Mandl, G. Shaw, *Quantum Field Theory (Revised Edition)*, John Wiley & Sons;
M. E. Peskin, D. V. Schroeder, *An Introduction to Quantum Field Theory*, Westview Press.

[5] Luis Alvarez-Gaume and John Ellis, *Eyes on a prize particle*, Nature Physics **7**, $2-3$ (2011).

[6] G. Bertone, D. Hooper, and J. Silk, Phys. Rept. **405**, 279 (2005).

[7] D. I. Kazakov, *Lectures given at the European School on High Energy Physics*, August-September 2000, Caramulo, Portugal, [hep-ph/0012288v2].

[8] S. Dimopoulos and H. Georgi, Nucl. Phys. **B193**, 150 (1981);
N. Sakai, Z. Phys. **C11**, 153 (1981);
R.K. Kaul, Phys. Lett. **109B**, 19 (1982).

[9] Yu.A. Golfand and E.P. Likhtman, JETP Lett. **13** (1971) 323;
A. Neveu and J.H. Schwartz, Nucl. Phys. **B31** (1971) 86;
A. Neveu and J.H. Schwartz, Phys. Rev. **D4** (1971) 1109;
P. Ramond, Phys. Rev. **D3** (1971) 2415;
D.V. Volkov and V.P. Akulov, Phys. Lett. **B46** (1973) 109;
J. Wess and B. Zumino, Phys. Lett. **B49** (1974) 52;
J. Wess and B. Zumino, Nucl. Phys. **B70** (1974) 39;

P. Fayet, Phys. Lett. **B69** (1977) 489;
G.R. Farrar and P. Fayet, Phys. Lett. **B76** (1978) 575;
S. P. Martin, *A Supersymmetry Primer*, arXiv:hep-ph/9709356.

[10] M. Drees, R. Godbole and P. Roy, *Theory and Phenomenology of Sparticles*, (World Scientific, Singapore, 2005);
H. Baer and X. Tata, *Weak Scale Supersymmetry: from Superfields to Scattering Events*, (Cambridge University Press, Cambridge, UK, 2006);
I.J.R. Aitchison, *Supersymmetry in Particle Physics: an elementary introduction*, (Cambridge University Press, Cambridge, UK, 2007).

[11] S. R. Coleman, J. Mandula, Phys. Rev. **159**, 1251 (1967).

[12] R. Haag, I. Lopuszanski, M. Sohnius, Nucl. Phys. **B88**, 257 (1975).

[13] P. Fayet, Nucl. Phys. **B78**, 14 (1974);
ibid., **B90**, 104 (1975);
R. Flores and M. Sher, Ann. Phys. (NY) **148**, 95 (1983).

[14] L. Susskind, Phys. Reports **104**, 181 (1984).

[15] Ilia Gogoladze, Bin He and Qaisar Shafi, *New fermions at the LHC and mass of the Higgs boson*, Phys. Lett. **B690**, 495 (2010).

[16] P. Fayet, Phys. Lett. **69B**, 489 (1977);
G. Farrar and P. Fayet, Phys. Lett. **76B**, 575 (1978).

[17] G. Jungman, M. Kamionkowski, and K. Griest, Phys. Reports **267**, 195 (1996);
K. Griest and M. Kamionkowski, Phys. Reports **333**, 167 (2000).

[18] L. Girardello and M. Grisaru, Nucl. Phys. **B194**, 65 (1982);
L.J. Hall and L. Randall, Phys. Rev. Lett. **65**, 2939 (1990);
I. Jack and D.R.T. Jones, Phys. Lett. **B457**, 101 (1999).

[19] P. van Nieuwenhuizen, Phys. Reports **68**, 189 (1981);
S. Deser and B. Zumino, Phys. Rev. Lett. **38**, 1433 (1977);
E. Cremmer et al., Phys. Lett. **79B**, 231 (1978);
L. Ibanez, Nucl. Phys. B218, **514** (1982);
L. Alvarez-Gaume, J. Polchinski, and M.B. Wise, Nucl. Phys. **B221**, 495 (1983).

[20] M. Dine, W. Fischler, and M. Srednicki, Nucl. Phys. **B189**, 575 (1981);
S. Dimopoulos and S. Raby, Nucl. Phys. **B192**, 353 (1982); **B219**, 479 (1983);
G.F. Giudice and R. Rattazzi, Phys. Reports **322**, 419 (1999).

[21] LEPSUSYWG, ALEPH, DELPHI, L3, and OPAL experiments, note LEPSUSYWG/04-01.1, `http://lepsusy.web.cern.ch/lepsusy/Welcome.html`.

[22] ALEPH Collaboration, Eur. Phys. J. **C25**, 339 (2002);
OPAL Collaboration, Eur. Phys. J. **C46**, 307 (2006);
LEPSUSYWG, *ibid.*, note LEPSUSYWG/02-09.2.

[23] The ALEPH, DELPHI, L3, OPAL, SLD Collaborations, the LEP Electroweak Working Group, the SLD Electroweak and Heavy Flavours Groups, Phys. Reports **427**, 257 (2006).

[24] LEPSUSYWG, *ibid.*, note LEPSUSYWG/01-03.1;
LEPSUSYWG, *ibid.*, note LEPSUSYWG/01-03.1;
LEPSUSYWG, *ibid.*, note LEPSUSYWG/02-04.1;
LEPSUSYWG, *ibid.*, note LEPSUSYWG/04-07.1;
LEPSUSYWG, *ibid.*, note LEPSUSYWG/02-06.1;
LEPSUSYWG, *ibid.*, note LEPSUSYWG/04-02.1.

[25] L. Zivkovic, *New Phenomena Searches at the Tevatron*, talk given at the Rencontres de Moriond QCD and High Energy Interactions, March 10-17, 2012, La Thuile, Italy.

[26] L. Zivkovic, *SUSY Searches at the Tevatron*, FERMILAB-CONF-11-317-E (2011).

[27] Michel Jaffre, *SUSY searches at the Tevatron*, arXiv:1202.0712 [hep-ex] (2012).

[28] Steven Lowette, *Supersymmetry Searches with ATLAS and CMS*, talk given at the Rencontres de Moriond QCD and High Energy Interactions, March 10-17, 2012, La Thuile, Italy.

[29] T. Lari, *Recent results from New Physics searches using the ATLAS detector at LHC*, ATL-PHYS-PROC-2011-150 (2011).

[30] M. Fehling-Kaschek, *Supersymmetry Searches at ATLAS*, ATL-PHYS-PROC-2012-039 (2012).

[31] The ATLAS Collaboration, *Search for squarks and gluinos using final states with jets and missing transverse momentum with the ATLAS detector in $\sqrt{s}$ = 7 TeV proton-proton collisions*, CERN-PH-EP-2011-145, arXiv: 1109.6572, 2011.

[32] The ATLAS Collaboration, *Search for new phenomena in final states with large jet multiplicities and missing transverse momentum using $\sqrt{s}$ = 7 TeV pp collisions with the ATLAS detector*, 10.1007/JHEP11(2011)099.

[33] The ATLAS Collaboration, *Search for supersymmetry in final states with jets, missing transverse momentum and one isolated lepton in $\sqrt{s}$ = 7 TeV pp collisions using 1 fb^{-1} of ATLAS data*, arXiv: 1109.6606, 2011.

[34] The ATLAS Collaboration, *Searches for supersymmetry with the ATLAS detector using final states with two leptons and missing transverse momentum in $\sqrt{s}$ = 7 TeV proton-proton collisions*, arXiv: 1110.6189, 2010.

[35] The ATLAS Collaboration, *Search for supersymmetry in pp collisions at $\sqrt{s}$ = 7 TeV in final states with missing transverse momentum, b-jets and no leptons with the ATLAS detector*, ATLAS-CONF-2011-098, 2011; The ATLAS Collaboration, *Search for supersymmetry in pp collisions at $\sqrt{s}$ = 7 TeV in final states with missing transverse momentum, b-jets and one lepton with the ATLAS detector*, ATLAS-CONF-2011-130, 2011.

[36] J. Campbell et al., *Hard interactions of quarks and gluons: a primer for LHC physics*, Reports on Progress in Physics, arXiv:hep-ph/0611148, 2007.

[37] R. Barate et al. [LEP Working Group for Higgs boson searches and ALEPH Collaboration], *Search for the standard model Higgs boson at LEP*, Phys. Lett. **B565**, 61 (2003) [arXiv:hep-ex/0306033].

[38] The ATLAS Collaboration, *The ATLAS Experiment at the CERN Large Hadron Collider*, JINST **3** S08003 (2008).

[39] The ATLAS Collaboration, *Expected Performance of the ATLAS Experiment - Detector, Trigger and Physics*, arXiv:0901.0512 [hep-ex].

[40] A. Negri et al., *ATLAS TDAQ System Integration and Commissioning*, Preprint submitted to TIPP09 Proceedings in Nucl. Instr. and Meth.

[41] The ATLAS Collaboration, *ATLAS Computing - Technical Design Report*, CERN-LHCC-2005-022, cds:837738.

[42] S. Frixione, B.R. Webber, JHEP **0206**, 029 (2002), [hep-ph/0204244]; S. Frixione, P. Nason, B.R. Webber, JHEP **0308**, 007 (2003), [hep-ph/0305252].

[43] G. Corcella et al., *HERWIG 6.5: an event generator for Hadron Emission Reactions With Interfering Gluons (including supersymmetric processes)*, JHEP 01 (2001) 010, arXiv:hep-ph/0011363.

[44] T. Sjostrand, S. Mrenna, and P. Skands, *PYTHIA 6.4 Physics and Manual*, JHEP 05 (2006) 026, arXiv:hep-ph/0603175.

[45] The GEANT4 Collaboration, *GEANT4: A simulation toolkit*, Nucl. Instrum. Meth. **A506**.

[46] E. Richter-Was, D. Froidevaux and L. Poggioli, *ATLFAST 2.0 a fast simulation package for ATLAS*, ATL-PHYS-98-131.

[47] E. Richter-Was, *AcerDET: A particle level fast simulation and reconstruction package for phenomenological studies on high p_T physics at LHC*, arXiv:hep-ph/0207355.

[48] The ATLAS Collaboration, *Expected electron performance in the ATLAS experiment*, ATL-PHYS-PUB-2011-006.

[49] D.Banfi et al., *The determination of the energy of electrons and photons in the ATLAS electromagnetic calorimeters*, ATL-PHYS-INT-2010-038.

[50] W. Lampl et al., *Calorimeter Clustering Algorithms : Description and Performance*, ATL-LARG-PUB-2008-002.

[51] S. Hassani, L. Chevalier, E. Lancon, J. F. Laporte, R. Nicolaidou and A. Ouraou, *A muon identification and combined reconstruction procedure for the ATLAS detector at the LHC using the (MUONBOY, STACO, MuTag) reconstruction packages*, Nucl. Instrum. Meth. **A572** (2007) 77.

[52] T. Lagouri et al., *A muon identification and combined reconstruction procedure for the ATLAS detector at the LHC at CERN*, IEEE Trans. Nucl. Sci. 51 (2004) 3030.

[53] G.C. Blazey et al., *Run II jet physics*, hep-ex/0005012.

[54] S. Catani, Y. L. Dokshitzer, M. H. Seymour and B. R. Webber, *Longitudinally invariant $K(t)$ clustering algorithms for hadron hadron collisions*, Nucl. Phys. **B406** (1993) 187;
S.D. Ellis and D.E. Soper, *Successive combination jet algorithm for hadron collisions*, Phys. Rev. **D48** (1993) 3160 [hep-ph/9305266].

[55] P. M. Nadolsky et al., *Implications of CTEQ global analysis for collider observables*, Phys. Rev. **D78** (2008) 013004, arXiv:0802.0007 [hep-ph].

[56] M. L. Mangano, M. Moretti, F. Piccinini, R. Pittau and A. D. Polosa, *ALPGEN, a generator for hard multiparton processes in hadronic collisions*, JHEP 07 (2003) 001, arXiv:hep-ph/0206293.

[57] D. Stump et al., *Inclusive jet production, parton distributions and the search for new physics*, JHEP 10 (2003) 046, arXiv:hep-ph/0303013.

[58] J. M. Butterworth, J. R. Forshaw, and M. H. Seymour, *Multiparton interactions in photoproduction at HERA*, Z. Phys. **C72** (1996) 637-646, arXiv:hep-ph/9601371.

[59] The ATLAS Collaboration, *Search for Supersymmetry with two leptons and missing transverse momentum at $\sqrt{s} = 7$ TeV*, ATL-COM-PHYS-2011-649, 2011.

[60] The ATLAS Collaboration, *Luminosity Determination in pp Collisions at $\sqrt{(s)} = 7$ TeV using the ATLAS Detector in 2011*, Eur. Phys. J. **C71** (2011) 1630 and ATLAS-CONF-2011-011-116.

[61] S. Moch and P. Uwer, *Theoretical status and prospects for top-quark pair production at hadron colliders*, Phys. Rev. **D78** (2008) 034003, arXiv:0804.1476 [hep-ph].

[62] U. Langenfeld, S. Moch, and P. Uwer, *New results for $t\bar{t}$ production at hadron colliders*, arXiv:0907.2527 [hep-ph].

[63] T. A. collaboration, *Jet energy resolution and selection efficiency relative to track jets from in-situ techniques with the ATLAS Detector Using Proton-Proton Collisions at a Center of Mass Energy $\sqrt{s} = 7$ TeV*, Tech. Rep. ATLAS-CONF-2010-054, CERN, Geneva, Jul 2010.

[64] F. Cerutti, C. Gatti, P. Kluit, O. Kortner, W. Liebig, J. Liu, G. Salamanna, A. Salvucci, E. Van der Poel, and J. Zhu, *Muon Momentum Resolution in First Pass Reconstruction of pp Collision Data Recorded by ATLAS in 2010*, Tech. Rep. ATLAS-COM-CONF-2011-003, CERN, Geneva, Jan 2011.

[65] The ATLAS Collaboration, *SUSY searches with dileptons and high missing transverse momentum*, Tech. Rep. ATL-PHYS-INT-2011-030, CERN, Geneva, 2011.

[66] The ATLAS Collaboration, *Search for high mass dimuon resonances at $\sqrt{s} = 7$ TeV*, Tech. Rep. ATL-COM-PHYS-2011-084, 2011

[67] The ATLAS Collaboration, *SUSY searches with dileptons and high missing transverse momentum*, Tech. Rep. ATL-PHYS-INT-2011-030, CERN, Geneva, 2011.

[68] G. Polesello and D. Tovey, *Supersymmetric particle mass measurement with the boost-corrected contransverse mass*, JHEP 1003 (2010) 030.

[69] The ATLAS Collaboration, *Search for supersymmetric particles in events with lepton pairs and large missing transverse momentum in $\sqrt{s} = 7$ TeV proton-proton collisions with the ATLAS experiment*, arXiv:1103.6214 [hep-ex].

[70] The ATLAS Collaboration, *Search for an excess of events with an identical flavour lepton pair and significant missing transverse momentum in $\sqrt{s} = 7$ TeV proton-proton collisions with the ATLAS detector*, arXiv:1103.6208 [hep-ex].

[71] The ATLAS Collaboration, *Measurement of the WW production cross section in proton-proton collisions at $\sqrt{s} = 7$ TeV with the ATLAS detector*, Tech. Rep. ATLAS-CONF-2011-015, CERN, Geneva, Mar, 2011.

[72] J. Butterworth, E. Dobson, U. Klein, B. M. Garcia, T. Nunnemann, J. Qian, D. Rebuzzi, and R. Tanaka, *Single Boson and Diboson Production Cross Sections in pp Collisions at* $\sqrt{s}$ *= 7 TeV*, Tech. Rep. ATL-COM-PHYS-2010-695, CERN, Geneva, Aug, 2010.

[73] I. Hinchliffe, F. E. Paige, M. D. Shapiro, J. Soderqvist, and W. Yao, *Precision SUSY measurements at CERN LHC*, Phys. Rev. **D55** (1997) 5520–5540, arXiv:hep-ph/9610544.

Acknowledgments

At the end of my PhD and of my thesis, I would like to thank those who have accompanied me in this way.

First, I want to thank my supervisor Giacomo for all the time he has dedicated to me and for the patience, also during the difficult and painful moments I have lived in these years.
Then, I am very grateful to Davide for the willingness, for the precious and prompt help...and obviously for having read and commented this thesis. Probably, without his solicitude I couldn't end my PhD.

Then, I would also like to thank Gabriella and Andrea Negri for the kindness and for the suggestions and help in the difficult moments. A special thanks to Silvia for the fantastic help, availability and friendship.

A big thanks also to Aurora, Fabrizio and Andrea for their warmth and affection, for their friendship; also in the gloomy moments, they gave me a smile. With them I felt at home.

I want to thank also the physicists met during these years at CERN, especially the Italian SUSY group: the friendly atmosphere created with some of them made more pleasant and calm my work. With them I share the passion and enthusiasm for my research and for the new Physics that (maybe) expects to be unveiled and detected.

A warm, sincere thanks to my Friends. They have come along with me in these years, sharing joys and sorrows of the PhD experience and of my life. They have been a fundamental support, a source of cheerfulness and warmth. I have no enough words to express my thanks to them. From my heart, a huge thanks!

Last but not least... The biggest thanks is for my family, the most precious gift of God for my life. Without my family not only the thesis, but my existence would be meaningless. As the dedication of this thesis suggests, nothing can separate us! I'm happy and proud to have two parents and a sister (a family) as mine!